MICROCOPY RESOLUTION TEST CHART
NATIONAL BUREAU OF STANDARDS 1963-A

MEASUREMENTS OF ELECTRICAL TRANSPORT PHENOMENA
IN SEMICONDUCTOR MATERIALS

FINAL REPORT: Grant No. AFOSR-79-0131
November, 1981

School of Electrical Engineering
Cornell University
Ithaca, NY 14853

REPORT DOCUMENTATION PAGE	READ INSTRUCTIONS BEFORE COMPLETING FORM

1. REPORT NUMBER AFOSR-TR- 82 -0015	2. GOVT ACCESSION NO. AD A111 528	3. RECIPIENT'S CATALOG NUMBER

4. TITLE (and Subtitle) MEASUREMENTS OF ELECTRICAL TRANSPORT PHENOMENA IN SEMICONDUCTOR MATERIALS	5. TYPE OF REPORT & PERIOD COVERED Final Report
	6. PERFORMING ORG. REPORT NUMBER

7. AUTHOR(s) Jeffrey Frey	8. CONTRACT OR GRANT NUMBER(s) AFOSR-79-0131

9. PERFORMING ORGANIZATION NAME AND ADDRESS Cornell University Ithaca, NY 14853	10. PROGRAM ELEMENT, PROJECT, TASK AREA & WORK UNIT NUMBERS 61102F 2301/A5

11. CONTROLLING OFFICE NAME AND ADDRESS Air Force Office of Scientific Research Washington, DC /NA	12. REPORT DATE November, 1981
	13. NUMBER OF PAGES 265

14. MONITORING AGENCY NAME & ADDRESS(if different from Controlling Office)	15. SECURITY CLASS. (of this report) unclassified
	15a. DECLASSIFICATION/DOWNGRADING SCHEDULE

16. DISTRIBUTION STATEMENT (of this Report)

Approved for public release; distribution unlimited.

17. DISTRIBUTION STATEMENT (of the abstract entered in Block 20, if different from Report)

18. SUPPLEMENTARY NOTES

19. KEY WORDS (Continue on reverse side if necessary and identify by block number)

Semiconductors, electron transport, high-field transport, experimental techniques, silicon properties, Gallium Arsenide properties

20. ABSTRACT (Continue on reverse side if necessary and identify by block number)

A microwave time-of-flight experiment is used to investigate the high-field transport of electrons and holes in silicon and electrons in GaAs.

In the experiment, a microwave-modulated electron beam bombards a reverse-biased semi-transparent rectifying contact on the surface of a low-doped epitaxial layer, creating secondary carriers which traverse the layer and are collected at the conducting substrate. Analysis of the ensuing periodic

DD FORM 1473 EDITION OF 1 NOV 65 IS OBSOLETE
1 JAN 73

unclassified

microwave current yields the carrier velocity as a function of electric field.

A general theory is presented from which expressions relating the carrier velocity as a function of depth to the amplitude and phase of each component of the test device terminal current are derived. The consequences of electric field nonuniformity in the sample are examined, and a method developed to correct for this effect. Diffusion effects are evaluated with a one-dimensional numerical simulation of carrier motion through a test device, duplicating experimental conditions. All other relevant secondary effects, including beam penetration depth, circuit effects, trapping, sample heating, impact ionization, and space-charge effects, are examined in the context of the present work.

Low field regions of the deduced velocity field curves are consistent with previously reported work, but the experiments described here extend to fields more than twice those achieved with more conventional time-of-flight experiments. Results are as follows:

1) Measured drift velocity of electrons in silicon is reported for fields between 5 and 135 kV/cm. A saturated velocity of $1.10 \pm .08 \times 10^7$ cm/sec is observed at 115 kV/cm.

2) Measured electron velocity in GaAs decreases steadily with increasing electric field, from $0.86 \pm .04 \times 10^7$ cm/sec at 40 kV/cm to $0.60 \pm .03 \times 10^7$ cm/sec at 205 kV/cm.

3) Measured hole velocity in silicon is presented for fields ranging from 9 to 235 kV/cm. Velocity saturation has been observed for the first time: a saturated velocity of $0.96 \pm .05 \times 10^7$ cm/sec is seen at fields above 175 kV/cm.

Two techniques by which the microwave time-of-flight experiment can yield high-field diffusivity are presented. For GaAs, in particular, we have determined that electron diffusivities of 5 ± 5 cm²/sec at 64 kV/cm, and 29 ± 8 cm²/sec at 170 kV/cm consistent with our experimental data.
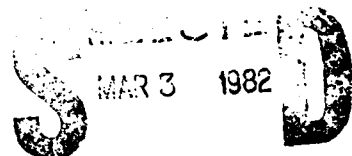
Finally, application of the experiment to the detection of transient effects is discussed. It is suggested that a modified version of the present microwave time-of-flight experiment in which optical carrier excitation is employed may permit detection of the "velocity overshoot" phenomenon predicted by Monte Carlo calculations.

MEASURMENTS OF ELECTRICAL TRANSPORT PHENOMENA

IN SEMICONDUCTOR MATERIALS

FINAL REPORT: Grant No. AFOSR-79-0131

November, 1981

MAR 3 1982

A

School of Electrical Engineering
Cornell University
Ithaca, N.Y. 14853

TABLE OF CONTENTS

LIST OF TABLES

ix

LIST OF FIGURES

x

xi

xiii

LIST OF SYMBOLS

A	Amplitude
a	Sample area
B	Bandwidth
C	Capacitance
C_d	Depletion layer capacitance
C_f	Fringing capacitance
C_p	Package capacitance
C_u	Undepleted zone capacitance
D	Diffusivity
D_p	Pseudodiffusion coefficient
E	Electric field
E_a	Average energy of transmitted primary electrons
F	Electron flux
f	Frequency
$\tilde{H}$	H-parameter matrix
I_o	Electron beam current
J	Current density
K	Terminal current
k	Boltzmann constant
L_D	Debye length
L_w	Bonding wire inductance
ℓ	Sample length - location of depletion layer edge
ℓ_o	Epitaxial layer thickness
M	Multiplication
m	Mass

m^* Carrier effective mass

N_a Acceptor concentration

N_d Donor concentration

N_t Trap density

n Electron concentration

p Hole concentration

q Electronic charge

R Resistance, electron range

R_s Substrate resistance

R_u Undepleted zone resistance

R_w Bonding wire resistance

T Period of oscillation, carrier temperature

t Time

t_f Fall time

t_r Rise time

V Voltage

V_{bi} Built-in voltage

V_{br} Breakdown voltage

V_n Noise voltage

V_x x deflection voltage

V_y y deflection voltage

v Carrier velocity

v_{app} Apparent velocity

v_{ave} Average velocity

v_t Electron beam transverse velocity

x Distance

Z_L Load impedance

α	Electron ionization coefficient
β	Hole ionization coefficient
$\Delta\phi_D$	Phase shift produced by diffusion
$\Delta\phi_E$	Phase shift produced by field taper
ε	Dielectric permittivity
ε_p	Electron-hole pair creation energy
η	Fraction of transmitted primary electrons
θ	Reflection coefficient phase
μ	Mobility
ρ	Resistivity
σ	Beam half-width, trapping cross-section
τ	Transit time
τ_m	Momentum relaxation time
τ_p	Plasma time
ϕ	Phase
ϕ_m	Measured phase
ω	Angular frequency

CHAPTER 1

INTRODUCTION

1.1 Background

When a weak electric field E is applied to a semiconductor, carriers respond according to

$$v = \mu E \qquad (1.1)$$

where v is the velocity and μ, a constant, is defined as the mobility. In 1951 Ryder and Shockley[1] found that for fields greater than about 1 kV/cm the mobility of electrons in n-type germanium became field-dependent. This first observation of nonlinear carrier transport in semiconductors has since been followed by numerous investigations, both theoretical and experimental, of the high field transport properties of semiconductors.

While physicists have always been interested in the behavior of carriers in semiconductors, specific device applications have at times provided added momentum to the work. In 1965 the advent of the Read diode[2], which operates at fields on the order of hundreds of kV/cm, sparked interest in carrier transport at very high fields. More recently, it has become possible to reduce the dimensions of common devices to submicron levels, and corresponding electric fields have increased accordingly. It will be seen that the results reported here are

significant in that they extend previous knowledge into the very high field regime.

With a number of assumptions, the general transport equations derived from kinetic theory reduce to the following forms[3]:

$$\frac{dn}{dt} + \nabla \cdot (nv) = 0 \tag{1.2}$$

$$\vec{v} = \mu(E)\vec{E} - \frac{D(E)}{n} \nabla n \tag{1.3}$$

$$\mu(E) = \frac{q\tau_p(E)}{m^*} \tag{1.4}$$

$$D(E) = \frac{kT(E)\tau_p(E)}{m^*} \tag{1.5}$$

where

n = carrier density

D = diffusivity

q = electronic charge

τ_p = momentum relaxation time

m^* = carrier effective mass

k = Boltzmann constant

T = carrier temperature

The assumptions under which (1.2) - (1.5) are valid are described in detail by Cook[4] and Blotekjaer[3]. Among these is the requirement that spatial and temporal variations in carrier energy, velocity and density are small; note that

in submicron devices this condition may not be satisfied. We do not attempt to strictly justify the use of equations (1.2) - (1.5) here, but they are considered appropriate in light of the present experimental conditions (i.e. relatively long sample lengths and slow time variation).

As seen above, a number of physical parameters including mobility, diffusivity, carrier temperature and momentum relaxation time are functions of the electric field.

Theoretical investigations of the high-field transport problem involve either analytical approximations[5] or numerical techniques. The most commonly used numerical approach is the Monte Carlo method[6-8], which simulates the motion of carriers through a semiconductor in a probabilistic manner. While the most important scattering mechanisms are realistically included, Monte Carlo results are in general strongly dependent upon the initial choice of material parameters[9]. One therefore seeks theoretical models (in this specific case a set of material parameters) which are consistent with experimentally observed behavior.

Experimental work thus provides the physical observations upon which an understanding of transport phenomena is built. A variety of techniques, reviewed in [10], have been used to measure quantities such as the drift velocity (equal to $\mu(E)E$), diffusion coefficient, and energy relaxation time. In the next section, various

techniques used to determine the most important transport quantity, the drift velocity, are presented and compared.

1.2 Drift Velocity Measurements

Experimental techniques by which carrier drift velocity is measured can be divided into four major groups: conductivity, microwave, space charge resistance, and time-of-flight. In this section each technique is described briefly, and advantages and disadvantages are presented.

Conductivity

This technique is the oldest, and is still frequently used[1,11-19]. It consists of measuring the conductivity of a semiconductor sample, i.e., the current as a function of applied voltage. Since the current density J is given by

$$J = qnv \qquad\qquad (1.6)$$

and the electric field by

$$E(V) = \frac{V}{\ell} \qquad\qquad (1.7)$$

where ℓ is the sample length, the velocity-field characteristic is obtained directly from $J(V)$, after both n and ℓ have been independently determined. Two commonly used test structures are shown in Figure 1.1.
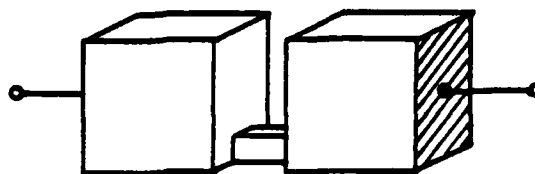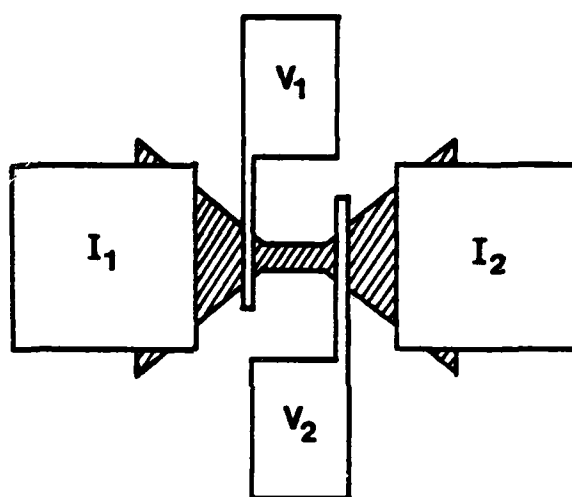
Figure 1.1. Test structures used in conductivity measure-
ments. a) large, single-crystal sample having metal
contacts on opposite ends (after Ryder[11]). b) planar
structure used for epitaxial layers on insulating
substrates (after Cook and Frey[19]); current flows
between contacts I_1 and I_2, voltage is measured across
contacts V_1 and V_2.

Advantages

1. Analysis of data is straightforward.

2. A wide range of doping levels can be used. For example, Nash and Holm-Kennedy[17] performed measurements on n-type silicon for several doping levels between 10^{14} and 2.5×10^{17} cm^{-3}.

3. Measurements can be performed on large, single crystal samples as well as thin epitaxial layers (see Figure 1.1).

Disadvantages

1. The carrier concentration n must be essentially uniform throughout the test region.

2. The technique requires that either n or the low-field mobility μ must be precisely determined. This is in practice difficult to accomplish; n derived from C-V measurements has an associated error of about 10%, and n or μ obtained from Hall-effect measurements is similarly imprecise. Uncertainty in the measured drift velocity is therefore on the order of 10%, relatively high compared to time-of-flight techniques.

3. Appreciable carrier injection from the contacts can occur, affecting the experimental results. This problem is usually circumvented by fabricating samples in which the test region is far from the metal contacts, and the sample cross-sectional area is large in the vicinity of the contacts, insuring that local electric fields are low,

thereby minimizing carrier injection. These design considerations have been incorporated into the test structures shown in Figure 1.1.

4.   Since relatively large currents can flow through the sample, appreciable heating can occur. The bias voltage must therefore be pulsed.

5.   Samples such as that shown in Figure 1.1a are difficult to fabricate.

6.   The conductivity technique can not be used to measure drift velocity in materials which possess N.D.M. (negative differential mobility, i.e. dv/dE $<$ 0) since oscillation will occur. However, a modified form of the technique, in which the current-voltage characteristic of a Gunn diode is measured during the transit time of a domain, has been successfully used to determine electron drift velocity in the N.D.M. region of GaAs.[20]

Microwave

In what is commonly referred to as the "microwave" technique, the average current density $<J>$ is determined from the power reflected from or absorbed by a sample which has been inserted in a rectangular waveguide.[21-25] The carriers are heated by strong electric fields which can be either ac or dc.

Advantages

1. It is not necessary to make dc electrical contact to the sample; hence, carrier injection is not a problem.

2. Normally, measurements are performed at a frequency sufficiently low that the carriers can be assumed to follow the field variation "instantaneously". If frequency is high enough, however, it is possible to evaluate microscopic times such as the energy relaxation time.[26]

Disadvantages

1. The technique requires accurate knowledge of the carrier concentration.

2. The interpretation of experimental data is rather involved, since <j> must be determined from integral equations. As a result, the technique is rarely used today.

Space-Charge Resistance

Drift velocities have been determined from measurements of the differential space-charge resistance $\Delta V/\Delta I$ of planar sandwich structures which contain a fully depleted low-doped layer in which the electric field is nearly uniform.[27-30] Since impact ionization can be included in the analysis,[28] the technique is applicable at fields close to avalanche breakdown, and in IMPATT diodes.[30] In a variation of this method, drift velocity

has been derived from the small-signal impedance of IMPATT devices measured at 8-12 GHz.[31]

Advantages

1. Results can be obtained at very high fields. In n-Si, for example, Duh and Moll[28] measured the saturated velocity at fields as high as 400 kV/cm.

2. It is not necessary to know the carrier concentration n.

Disadvantages

1. The method is indirect, and analysis of the data is based upon several assumptions. First, the velocity is assumed to be saturated, and is therefore taken to be constant throughout the sample. When electron velocity is being studied, one must assume a value for the hole velocity, and vice-versa. Also, ionization coefficients must be known to properly interpret the measured data.

2. The technique is not suitable for testing new materials since fabrication of the sandwich structure requires a fairly advanced material growth technology such as is now available only for Si and GaAs.

3. In general, results are in the form of discrete points and are limited to high fields.

Time of Flight

The time-of-flight technique[32] consists of the
measurement of the time τ taken by a pulse of carriers,
created by some form of ionizing radiation, to travel
across a sample of known width ℓ in response to an applied
electric field. The drift velocity is then

$$v = \frac{\ell}{\tau} \tag{1.8}$$

The experiment is illustrated in Figure 1.2(a).
While the ionizing radiation usually takes the form of
electrons in the 10 to 40 keV range, nuclear particles and
photons have also been used. A number of electron-hole
pairs are created close to the surface; depending on the
direction of the applied field, one carrier type is
immediately swept out the irradiated contact while the
other drifts through the sample, inducing a current in the
external measurement circuit which lasts for a time τ (see
Figure 1.2b).

The current pulse, viewed on a sampling oscilloscope,
is found to have finite rise and fall times t_r and t_f due
to the electron apparatus, where t_r and t_f are defined in
Figure 1.2b. Note that when diffusion is present, the
fall time t_f is greater than the rise time t_r, and carrier
diffusivity can be obtained[34-36].

The time-of-flight technique has been used to
characterize a wide variety of materials, including
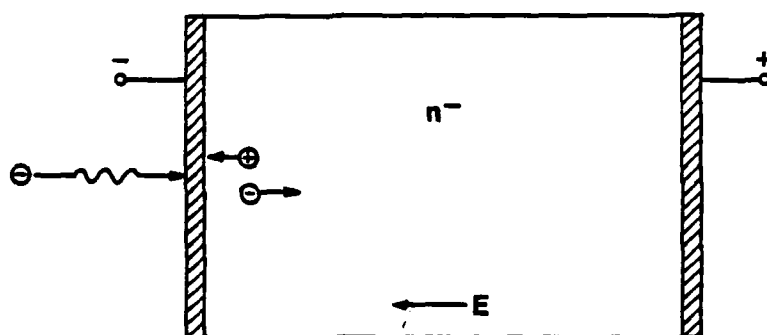
a)
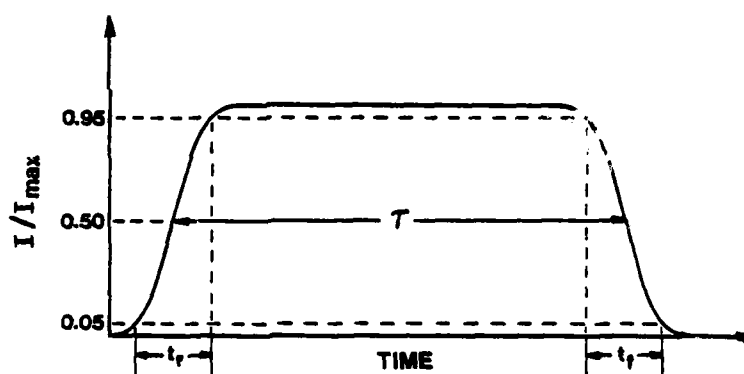
b)

Figure 1.2.   Time-of-flight technique.   a) Sample geo-
metry.   b) Induced current pulse.

$Si,$[33,36-43] $GaAs$[34,44], Ge[45,46], $CdTe$[47], $InSb$[48], $CdSe$[49] and CdS[50].

Advantages

1.   As a result of the simple form of Equation (1.8), the method is both accurate (estimated error is on the order of 5%) and direct.

2.   It is not necessary to know the carrier concentration n.

3.   The same sample can be used for both electron and hole measurements, by applying proper bias and irradiating either the front or back contact.

4.   Diffusivities can be determined.

Disadvantages

1.   Material must be very pure (i.e. low carrier concentration).

2.   For measurable transit times (i.e., nsec range), relatively long samples must be used. It may not be possible to test materials in which it is difficult to obtain thick, high-resistivity samples which are uncompensated. Also, very large voltages must be applied to establish strong electric fields.

3.   The transit time must be short compared to both the dielectric relaxation time and the mean carrier lifetime.

4.   If an electron beam is used, the experiment must be performed in a vacuum chamber.

In its usual form, then, the time-of-flight technique suffers from several disadvantages. However, a modified version of the time-of-flight technique, known as the <u>microwave</u> time-of-flight technique, alleviates most of these problems. This technique, which has been used in the present work, is discussed in the next section.

The Microwave Time-of-Flight Technique

A block diagram of the microwave time-of-flight experiment is shown in Figure 1.3. A 2.5 kV electron beam is deflected at a microwave frequency in a direction transverse to its axis by passage through a resonant microwave cavity. Consequently, short bursts of electrons periodically bombard the sample, creating secondary carriers which move in response to the applied field, thereby producing a microwave current. Carrier velocity is determined from the measured bias voltage dependence of the amplitude and phase of a given Fourier component of the periodic current waveform. Note that the beam may be positioned so as to intercept the sample either once or twice per microwave cycle; consequently the primary spectral component of sample current can occur at the cavity resonant frequency (5.3 GHz in our experiment) or its second harmonic.

Since phase shifts can be measured quite accurately, transit times as short as 10 psec can be measured, and
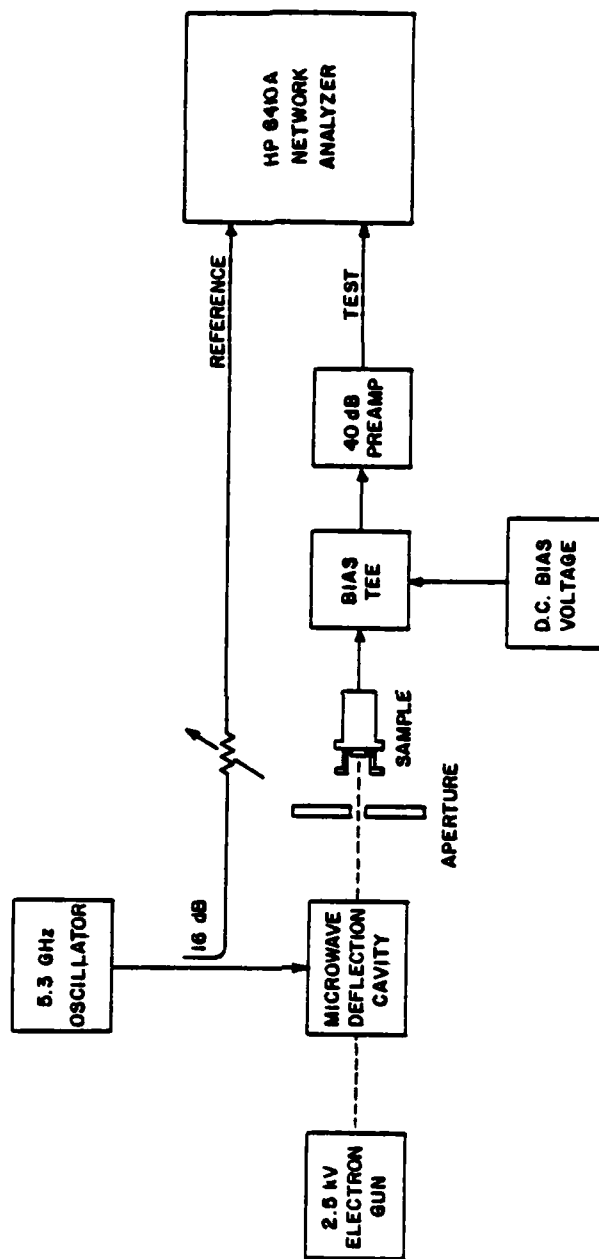
Figure 1.3. Microwave time-of-flight experiment.

thin samples can therefore be used. For mechanical support, test layers are deposited on thick highly conductive substrates. As a result, samples can not be reversed to facilitate measurements of both carrier types. However, the use of thin samples circumvents several problems associated with the classical time-of-flight technique:

1. Carrier concentration can be as high as 10^{15} cm^{-3} before electric field non-uniformity poses a problem.

2. The technique is better suited to materials in which it is difficult to obtain thick, high resistivity samples which are uncompensated.

3. The requirement that the transit time is short relative to the dielectric relaxation time and the carrier lifetime is more easily satisfied.

4. Large electric fields can be established with considerably lower bias voltages.

A comparison of several aspects of the classical and microwave time-of-flight experiments appears in Table 1.1 in order to insure that the beam penetration depth is negligible, a smaller electron beam accelerating potential is used in the microwave technique. In addition to the advantages already mentioned, thinner samples undergo avalanche breakdown at higher fields, so that the microwave time-of-flight experiment has produced results at field strengths more than twice those possible with the classical technique.

Table 1.1

Comparison of classical time-of-flight experiment

with the microwave time-of-flight experiment used

in the present work

	Classical	Microwave
Sample length ℓ	$> 200 \mu m$	$1\text{-}10 \ \mu m$
Carrier concentration	$\leq 10^{12} cm^{-3}$	$\leq 10^{15} cm^{-3}$
E-beam energy	10-40 keV	2.5 keV
Typical transit time	5 nsec	30 psec
Transit time resolution	100 psec	.2 psec
Maximum bias voltage	5 kV	200 V
Maximum electric field: n-GaAs	100 kV/cm	205 kV/cm
n-Si	50 kV/cm	135 kV/cm
p-Si	50 kV/cm	235 kV/cm

The theory of the microwave time-of-flight experiment is presented and developed in the next chapter. Chapter 3 describes the experimental apparatus. A detailed explanation of the data reduction procedure is given in Chapter 4, along with measured velocity field curves for electrons and holes in silicon and electrons in GaAs. Several secondary effects are analyzed in Chapter 5. Chapter 6 deals with application of this technique to the measurement of transient effects in thin samples. The results of this work are summarized in Chapter 7, and suggestions are made for future endeavors.

CHAPTER 2

THEORY OF MICROWAVE TIME-OF-FLIGHT MEASUREMENTS

2.1. General Description

The experimental system has been described in the
last chapter. In this chapter theory is presented which
relates carrier velocity to the quantity measurable in
this experiment: test device terminal current. In
Section 2.2 an analytical theory is developed. The effect
of non-uniform electric field is considered in Section
2.3. Finally, in Section 2.4 the analysis is extended to
include diffusion effects, which necessitate a one-
dimensional numerical simulation duplicating experimental
conditions.

The important time relationships and various
waveforms in the system are shown in Figure 2.1. The
electron beam, deflected by a sinusoidal electric field,
sweeps back and forth, irradiating the sample at one end
of its sweep, i.e. once per cycle. Each incident primary
electron creates many electron-hole pairs near the
surface: depending on the direction of the electric
field, one carrier type will be swept to the surface, the
other will drift through the layer and be collected, on
average, a time τ later. According to Ramo's theorem, the
terminal current at any instant is proportional to the
particle current integrated over the length of the test

18
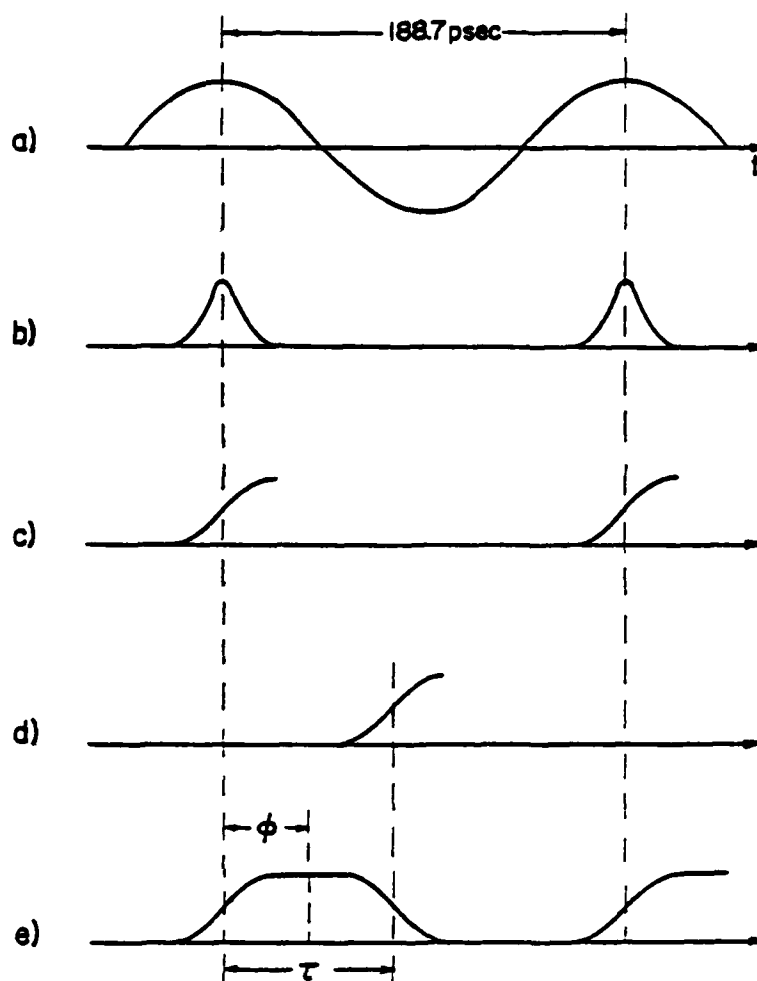
Figure 2.1. Waveforms for 5.3 GHz operation, assuming
constant carrier velocity and neglecting diffusion and
trapping. a) Deflecting electric field. b) Electron
flux incident on sample. c) Number of secondary
electrons (or holes) created in sample. d) Number of
carriers collected. e) Terminal current (c-d).

region. For the case of a constant velocity, the transit time is simply the sample length ℓ divided by the velocity v. From 2.1, it can be seen that the difference in phase between the fundamental frequency components of the incident electron flux and the terminal current is

$$\phi = \frac{\omega\tau}{2} = \frac{\omega\ell}{2v} \cdot \tag{2.1}$$

2.2.1. Analytical Theory

In this section we apply the basic semiconductor equations to our test structure in order to calculate the measurable quantity of this experiment, the device terminal current. This treatment is analytical, and requires that certain assumptions be made. The validity of these assumptions is considered in Chapter 5.

It is assumed that electron-hole pairs are created instantaneously at the surface (x = 0). The carrier of interest drifts through the epitaxial layer whereas its partner, having opposite charge, is immediately swept out the surface contact. For simplicity, this analysis takes the carrier of interest to be an electron, but the treatment of holes is identical. In the present discussion diffusion, trapping, and field induced impact ionization are neglected.

In the absence of generation and recombination, the current continuity equation is written as

$$\frac{\partial n}{\partial t} + \nabla \cdot nv = 0. \qquad (2.2)$$

For a one-dimensional system (x variation only) (2.2) becomes

$$\frac{\partial n}{\partial t} + \frac{1}{q}\frac{\partial J}{\partial x} = 0 \qquad (2.3)$$

where we have also included the fact that

$$J = qnv. \qquad (2.4)$$

Since velocity v is a function of position only, Equation (2.3) becomes

$$\frac{\partial J}{\partial x} + \frac{1}{v}\frac{\partial J}{\partial t} = 0. \qquad (2.5)$$

We now take the quantities n, J and E to be periodic in time, so that they can be written in the form

$$\sum_{i=o}^{\infty} c_i e^{j\omega_i t}.$$

Our analysis continues for one Fourier component of the series, that which occurs at angular frequency ω. Equation (2.5) then becomes

$$\frac{\partial \tilde{J}}{\partial x} + \frac{j\omega}{v}\tilde{J} = 0. \qquad (2.6)$$

where the tilde is used to denote an ac quantity. The

solution of this differential equation is

$$\tilde{J} = J_o \ e^{j\omega t} \ \exp(-j\omega \int_o^x \frac{dx'}{v(x')}) \tag{2.7}$$

where J_o is a constant dependent on such factors as electron beam energy and current, surface metallization, and electron-hole pair creation energy.

Poisson's equation states that

$$\frac{\partial E}{\partial x} = \frac{q}{\epsilon} \ (N_A - N_D + n_o - p_o + n) \tag{2.8}$$

Since n and E are the only time dependent quantities in (2.8), substitution into Equation (2.3) yields

$$\frac{\partial}{\partial x} \ [\tilde{J} + \epsilon \frac{\partial \tilde{E}}{\partial t}] = 0 \tag{2.9}$$

where $\tilde{K}$, the terminal current of the device, is defined by

$$\frac{\tilde{K}}{a} = \tilde{J} + \epsilon \frac{\partial \tilde{E}}{\partial t} \tag{2.10}$$

and is constant with respect to position. Integrating over the length of the sample, we obtain

$$\tilde{K} = \frac{a}{\ell} \int_o^\ell (\tilde{J} + \epsilon \frac{\partial \tilde{E}}{\partial t}) \ dx \tag{2.11}$$

$$= \frac{a}{\ell} \int_0^\ell \tilde{J} \, dx + \frac{\varepsilon a}{\ell} \frac{\partial}{\partial t} \int_0^\ell \tilde{E} \, dx \qquad (2.12)$$

Under constant bias voltage conditions, the second term in (2.12) vanishes, leaving

$$\tilde{K} = \frac{J_o a e^{j\omega t}}{\ell} \int_0^\ell \exp(-j\omega \int_0^x \frac{dx'}{v(x')}) \, dx \qquad (2.13)$$

The terminal current is a complex quantity of the form $A \cdot \exp[j(\omega t - \phi)]$. The amplitude A and phase ϕ are evaluated according to the following equations:

$$A = \frac{J_o a}{\ell} \left[(\int_0^\ell \sin(\omega \int_0^x \frac{dx'}{v(x')}) \, dx)^2 \right.$$
$$\left. + (\int_0^\ell \cos(\omega \int_0^x \frac{dx'}{v(x')}) dx)^2 \right]^{1/2} \qquad (2.14)$$

$$\phi = \tan^{-1} \left[\frac{\int_0^\ell \sin(\omega \int_0^x \frac{dx'}{v(x')}) \, dx}{\int_0^\ell \cos(\omega \int_0^x \frac{dx'}{v(x')}) \, dx} \right] \qquad (2.15)$$

These equations relate $v(x)$, carrier velocity as a function of position, to the two quantities which can be measured, the amplitude and phase of each frequency component of the device terminal current. However, it is difficult to determine $v(x)$ from a set of measurements of amplitude and phase versus average electric field.

Furthermore, while through iteration a v(x) can be found which is consistent with the measurements, it is not known whether this is a unique solution.

2.2.2. Constant Velocity Case

For the time and distance scales involved in this experiment, the carrier velocity can normally be approximated as an instantaneous function of the electric field. If the electric field throughout the sample is constant, and injected currents are small, carrier velocity will also be constant, and (2.14) and (2.15) reduce to

$$A = J_o \frac{\sin \left(\frac{\omega \ell}{2v}\right)}{\frac{\omega \ell}{2v}} \qquad (2.16)$$

$$\phi = \frac{\omega \ell}{2v} \qquad (2.17)$$

These simplified expressions allow velocity to be determined relatively easily from measurements of A and ϕ.

The amplitude takes the functional form sin (x)/x and is therefore negative when x falls within certain intervals (for example, $\pi < x < 2\pi$. Only a positive amp.itude is measured experimentally. Since

$$- A e^{jd} = Ae^{j(\phi - \pi)} \qquad (2.18)$$

we measure a positive amplitude and a phase which is shifted by π when the amplitude given by Equation (2.16) is negative. Furthermore, the cyclic nature of phase constrains the measured phase to the range $0 < \phi < 2\pi$. The forms of measured phase and measured amplitude are plotted in Figure 2.2 as functions of $\phi = \omega\ell/2v$.

The amplitude is equal to zero for

$$\frac{\omega\ell}{2v} = m\pi \tag{2.19}$$

where $m = 1, 2, 3\ldots$. Relative maxima, or "peaks", occur in the amplitude for values of $\omega\ell/2v$ determined by setting

$$\frac{d}{d\left(\frac{\omega\ell}{2v}\right)} \left[\frac{\left|\sin\left(\frac{\omega\ell}{2v}\right)\right|}{\frac{\omega\ell}{2v}}\right] = 0, \tag{2.20}$$

resulting in the transcendental equation

$$\tan\left(\frac{\omega\ell}{2v}\right) = \frac{\omega\ell}{2v}, \tag{2.21}$$

Solutions of this equation are given by Equation (2.19), with $m = 0, 1.430, 2.459, 3.471, 4.477\ldots$. Experimental observation of a peak or zero in the amplitude leads directly to the carrier velocity according to

$$v = \frac{f\ell}{m} \tag{2.22}$$
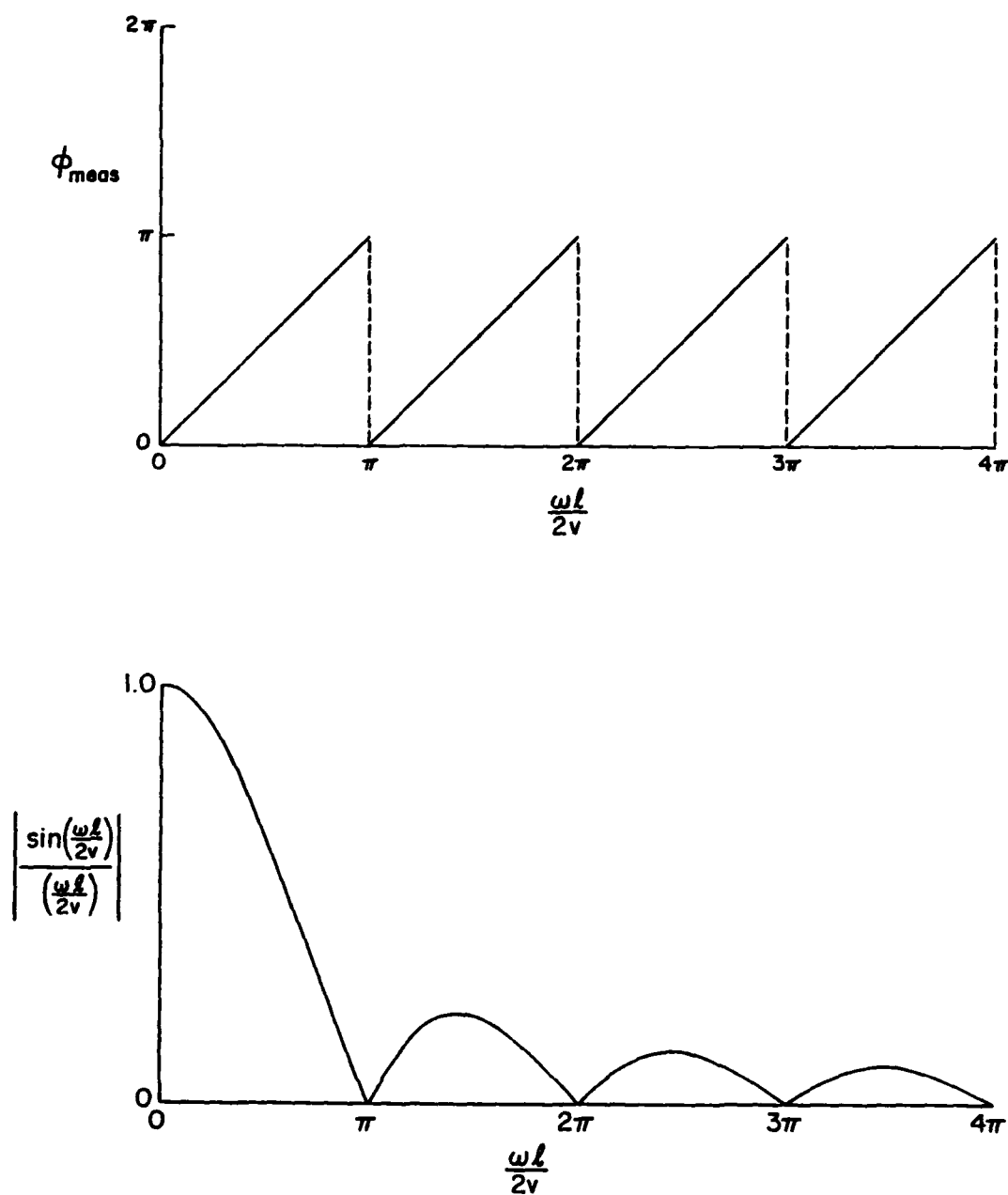
Figure 2.2. Measured phase and amplitude vs. actual phase
ϕ for the constant velocity case.

where f and ℓ are known quantities. Obviously, the maximum occurring at m = 0 is not physically observable.

In order to illustrate the magnitudes of measured quantities to be expected in this experiment, the calculated dependences of terminal current amplitude and phase on carrier velocity given by (2.16) and (2.17) are shown in Figures 2.3 through 2.6 for samples 1 and 10 micrometers in length at the two frequencies of operation of this experiment, 5.3 and 10.6 GHz. 1 and 10 micrometers are approximately the lengths of the thinnest and thickest epitaxial layers, respectively, for which the experiment was performed.

We see that for a length of 10 micrometers, the amplitude possesses several extrema; in general, a greater number can be observed at 10.6 GHz than at 5.3 GHz for a specified range in velocity. Furthermore, although each 5.3 GHz amplitude minimum corresponds to a 10.6 GHz minimum with the same velocity (as required by (2.22)), the amplitude relative maxima are unique in that they occur for a given velocity at only one frequency.

For a 10 micrometer long sample, the phase is seen to vary rapidly with velocity. At 10.6 GHz, for example, the total variation in phase as velocity varies from 0.3 to 2.0×10^7 cm/sec is 540 degrees. It should also be noted that the phase jumps discontinuously by 180 degrees whenever the amplitude passes through a minimum. In addition, the phase is proportional to frequency, and thus
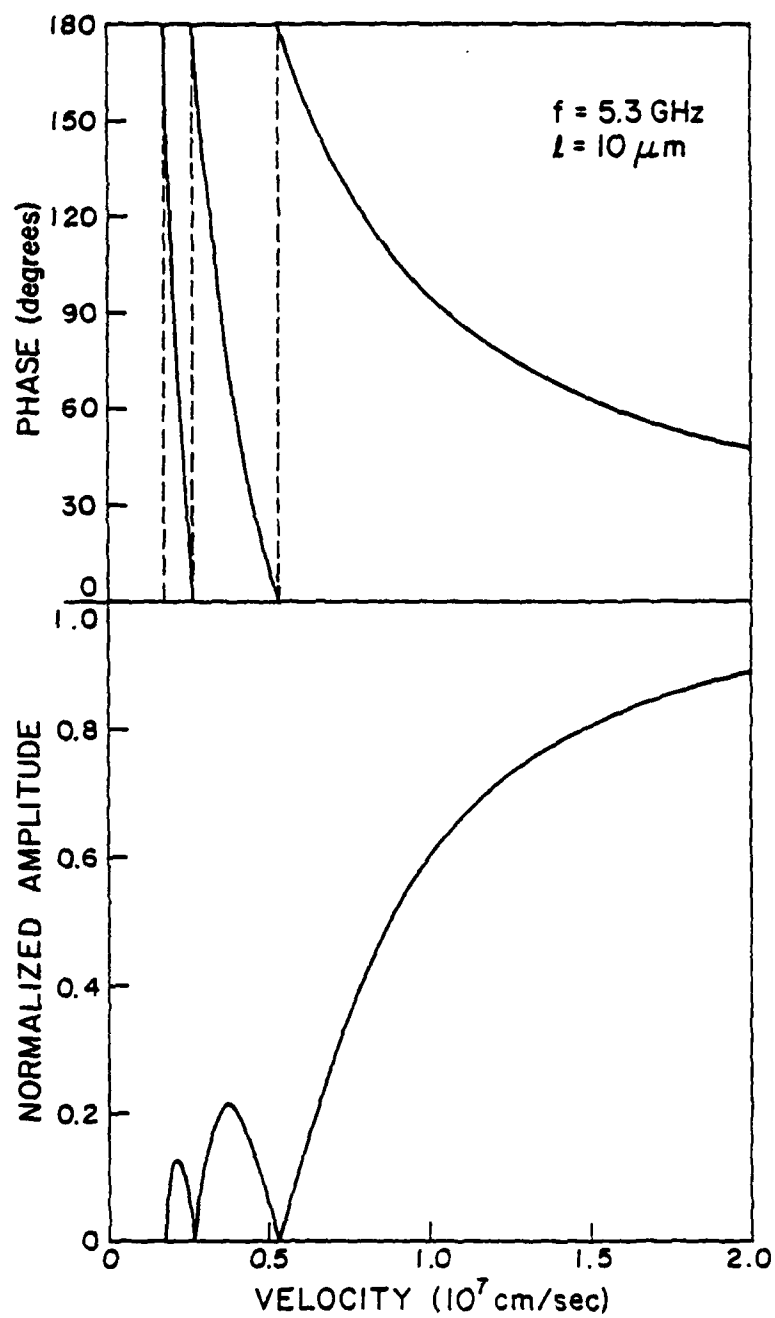
Figure 2.3.   Phase and amplitude vs. carrier velocity for

ℓ = 10 μm, f ≈ 5.3 GHz.
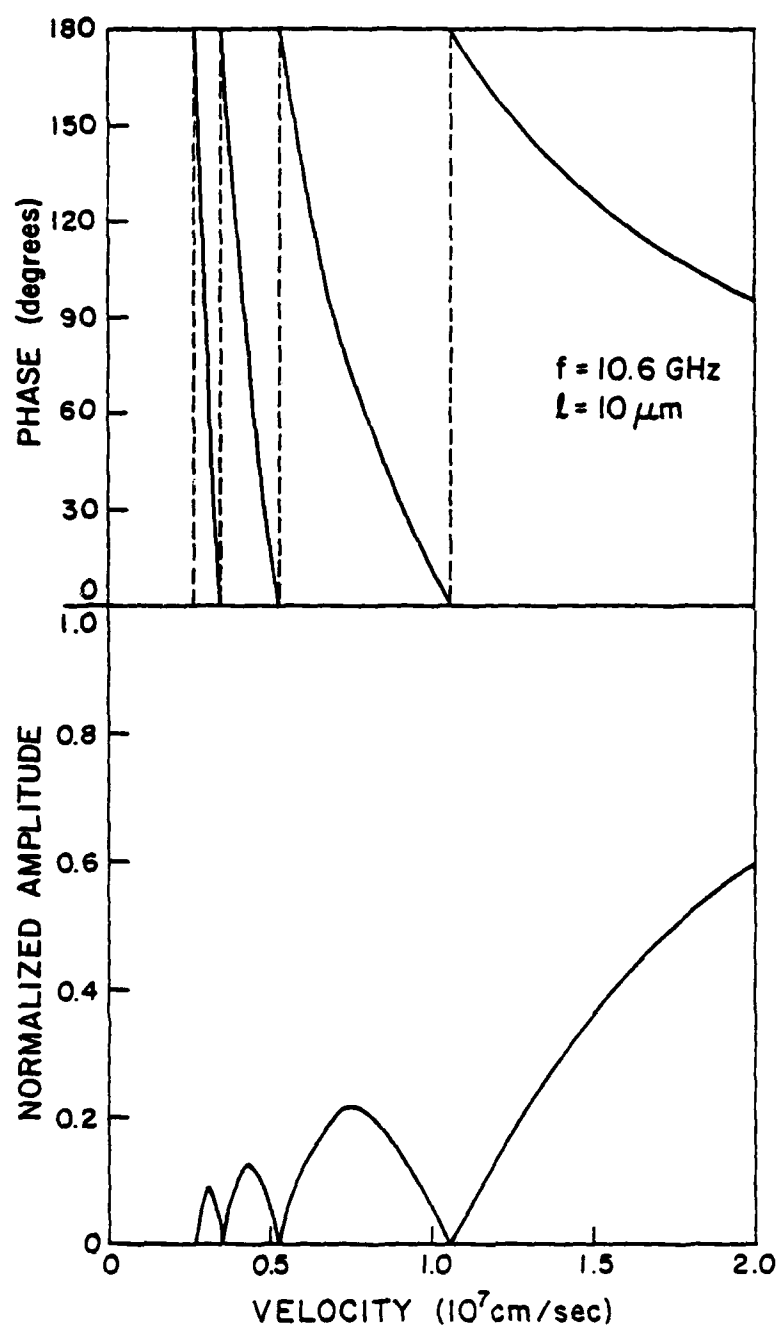
Figure 2.4. Phase and amplitude vs. carrier velocity for

ℓ = 10 μm, f = 10.6 GHz.
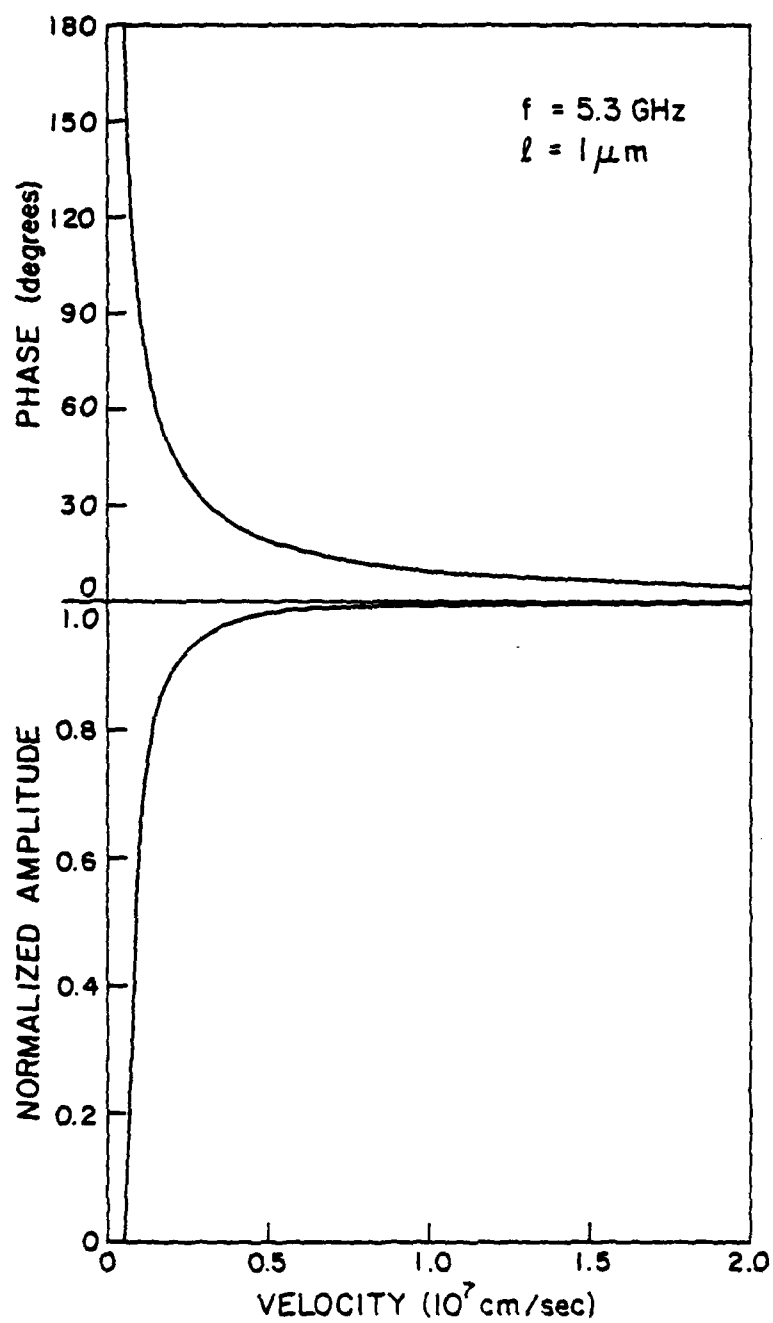
Figure 2.5. Phase and amplitude vs. carrier velocity for

$\ell = 1$ μm, f = 5.3 GHz.
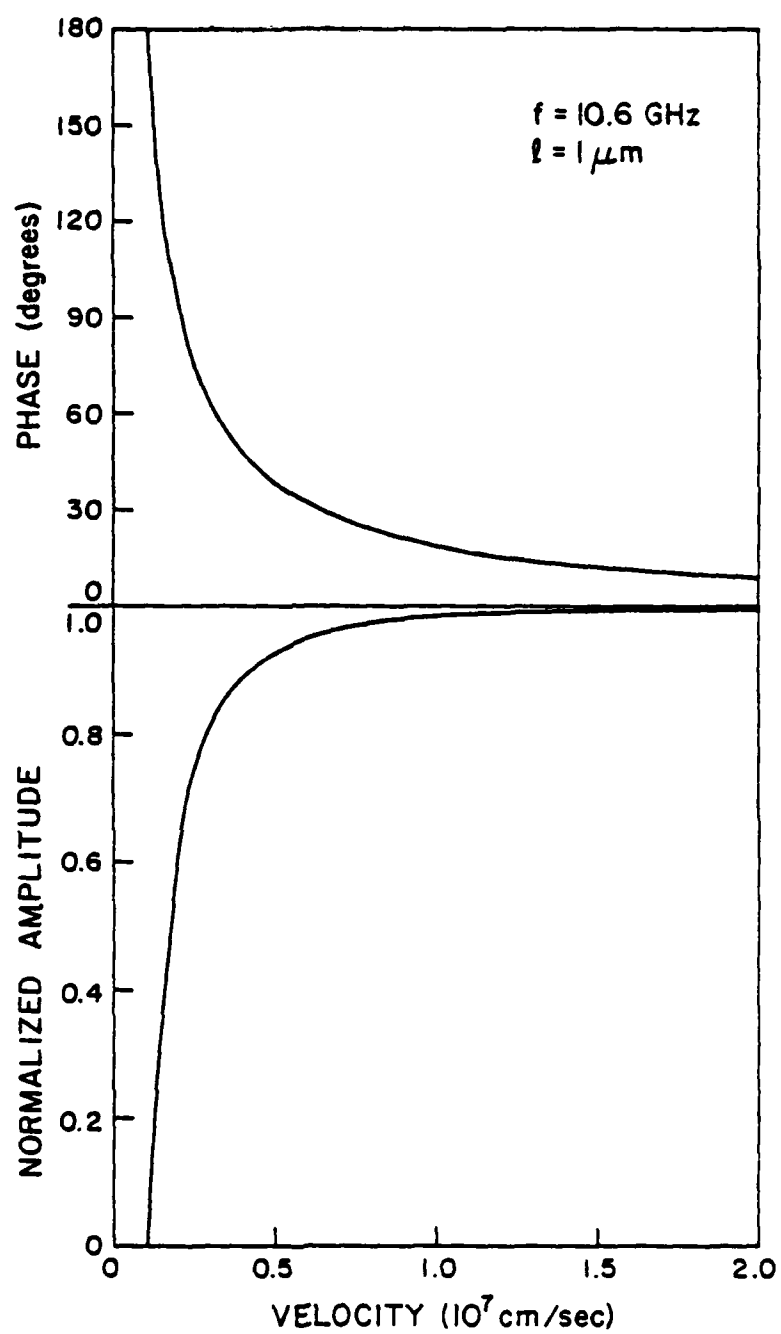
Figure 2.6.   Phase and amplitude vs. carrier velocity for

ℓ = 1 μm, f = 10.6 GHz.

at 10.6 GHz is exactly twice that at 5.3 GHz.

The variation in both phase and amplitude with velocity is much smaller for a 1 micrometer sample length. The first amplitude minimum, corresponding to m = 1 (ϕ = π), occurs at extremely low values of velocity - 0.05 x 10^7 cm/sec at 5.3 GHz and 0.11 x 10^7 cm/sec at 10.6 GHz.

In this experiment the range of electric field strength at which measurements can be made is determined by two factors - electric field non-uniformity determines the lower limit, whereas avalanche breakdown fixes the maximum. The velocity therefore assumes values within certain bounds. For the frequencies of operation of this experiment, 5.3 and 10.6 GHz, and sample lengths on the order of a few micrometers or less, it is possible that

$$0 < \frac{\omega \ell}{2v} < \pi \tag{2.23}$$

i.e., no amplitude extrema may be experimentally observed. In a typical GaAs sample, electric field strength might be confined to the region between 50 and 150 kV/cm. The corresponding velocity ranges from 0.70 to 0.86 x 10^7 cm/sec. Obviously, for thin samples the value of ϕ will be much less than π, and no amplitude minima will be seen. Moreover, for such a narrow range of velocity, the calculated phase of a 1 micrometer sample varies by only 2.5 degrees at 5.3 GHz, from 11.1 to 13.6 degrees. In this case the calculated amplitude changes almost

imperceptibly, by only .3%. Experimentally, phase can be resolved more accurately than amplitude - our phase resolution is estimated to be half a degree, whereas amplitude resolution error may be as high as 3%. For thin samples, therefore, the measured phase is a more useful quantity than the amplitude.

Due to the experimental configuration, i.e., the unknown electrical lengths of the test and reference channels, the electron beam drift distance, etc., our microwave time-of-flight experiment is not capable of measuring absolute phase. What we measure, instead, is

$$\phi_{meas} = \phi_0 + \phi(V) \tag{2.24}$$

where ϕ_0 is an unknown constant of the system at a particular frequency, and $\phi(V)$ is the absolute phase as a function of sample bias voltage V, given in the general case by Equation (2.15) and in the constant velocity case by Equation (2.17). Clearly, it is necessary to evaluate ϕ_0 in some way so that it can be subtracted from the measured phase. The most straightforward approach would be to determine ϕ_0 for the experimental system with some type of calibration procedure. Several such schemes are proposed in Appendix F.

Alternatively, one can remove the effect of ϕ_0 by equating the measured phase at one point with that predicted for an assumed value of carrier velocity. This

reference value of velocity can be derived in one of the
following ways:

1. An observed extremum in the amplitude provides
   an absolute value of velocity, and hence phase,
   to which the entire phase curve might be
   matched. Since the phase is discontinuous at
   amplitude minima, it is impossible to use a
   minimum as a reference point for phase measured
   at the same frequency. However, amplitude
   minima occurring at 10.6 GHz for m odd can be
   used to correct measured phase at 5.3 GHz. In
   addition, the phase is well behaved in the
   vicinity of all amplitude relative maxima;
   consequently these data lead to valid reference
   values of velocity.

2. The carrier velocity at low fields may be
   measured for the same material using a different
   technique, such as Hall mobility or J-V
   measurements. If the low field mobility is to
   be used as a reference, the phase measurements
   must be meaningful at fields sufficiently low
   that the velocity-field characteristic can be
   taken as linear.

3. A velocity measured by other workers, either
   from a single experiment or an average from
   several experiments, might be used as a
   reference. Since the microwave time-of-flight

experiment is capable of measurements at higher
fields than other techniques, a low field $v(E)$
characteristic which is reasonably well known
(by virtue of the fact that it has been
determined from measurements using a variety of
techniques, with good agreement) can be
accurately extended to higher fields. When
using this method, one must choose a velocity
obtained for material of the same impurity
concentration as that used in the microwave
time-of-flight experiment, except when the field
is sufficiently high that ionized impurity
scattering is insignificant, resulting in a
velocity which is independent of doping.

Ideally, measurement of either the amplitude or phase
of any frequency component of the terminal current would
permit evaluation of carrier drift velocity versus
electric field. In our experiment, however, both
amplitude and phase are measured at two distinct
frequencies. In some cases our data is redundant, whereas
in others the data is insufficient due to the experimental
problems mentioned in this section.

For thick samples, we have seen that amplitude
extrema yield absolute values of velocity at discrete
points determined by the frequency and sample length, two
quantities which are not easily varied in our experiment.
A thin sample may have no observable amplitude extrema.

In addition, the amplitude is difficult to measure accurately, particularly for thin samples.

Phase, on the other hand, can be measured continuously over a wide range of velocities with exceptionally good resolution (0.5 degrees). Since this is only a relative measurement, however, data must be corrected by evaluating and subtracting a constant phase shift inherent to the experimental system, either by direct measurement or the use of a velocity reference point.

2.2.3. Discussion of Amplitude Zero

We have seen that the modulated electron beam creates a cloud of carriers which drifts through the epitaxial layer under the influence of an applied electric field, and is collected at the conducting substrate. If the carriers move at a constant velocity and the transit time is equal to one period of excitation, the phase given by Equation (2.17) is π, and the corresponding terminal current rf amplitude should be zero.

This phenomenon is illustrated in Figure 2.7. At time t_1, the incident beam produces a charge packet at the surface, the terminal current rising accordingly. Exactly one period later, at time $t_1 + T$, this packet has traveled through the layer and is collected; the terminal current due to these moving charges now decreases. At the same time, however, more carriers are being created at the
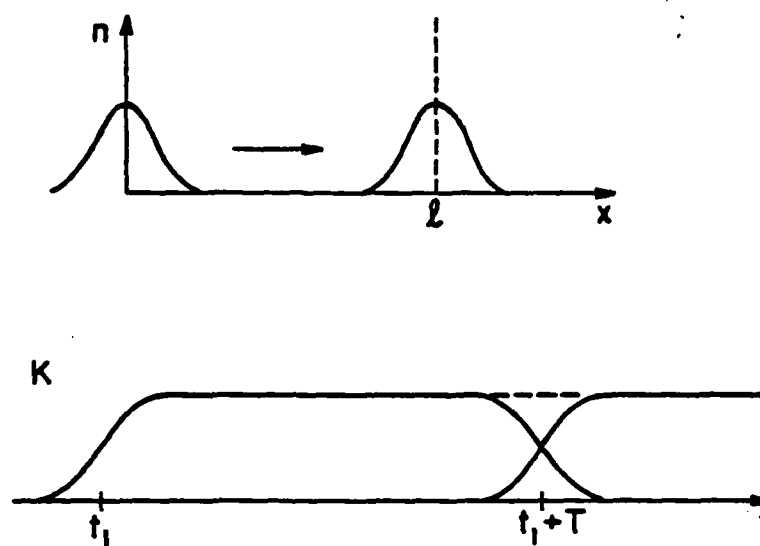
Figure 2.7. Carrier spatial distribution n(x) and result-
ing terminal current K(t) for a transit time equal to
one period of oscillation.

surface. The terminal current for times close to $t_1 + T$ is therefore the sum of two components, one decreasing with time and the other increasing.

If the shape of the packet at both front and back planes of the sample is the same, then the rising and falling curves will add to give a resultant terminal current which is constant in time, i.e., all rf components vanish. Furthermore, it can also be shown that such an amplitude null can arise for charge distributions of arbitrary shape as well. In addition, the physical width of the carrier distribution need not be small compared with the sample length.

The origin of the amplitude zero arising when the transit time is exactly one period has just been explained. Similarly, the amplitude is equal to zero for transit times which are an integral number of periods.

It should be emphasized that the amplitude will be zero only if the carriers travel with a constant velocity and the shape of the carrier distribution remains unchanged as the carriers traverse the test region. If the velocity is not constant, then the terminal current "plateau" shown in Figure 2.7 will not be level. A change in the shape of the carrier distribution implies that the sum of the previously mentioned rising and falling components of the terminal current will not be constant in time. In either case the resulting terminal current will have non-zero rf components.

The carrier velocity may vary with position if transients are present or if the electric field is not constant throughout the test region. The effect of a non-uniform electric field is considered in the next section.

The shape of the carrier distribution can be altered by several effects. Diffusion, discussed later in this chapter, causes spatially localized charge concentrations to spread. Trapping would prevent some carriers from reaching the back contact; in this case the current would decay with time.

2.3. Non-uniform Electric Field

In this section we consider the effects of electric field non-uniformity on test device terminal current. A one-dimensional Poisson equation allows the sample electric field variation to be calculated from the doping profile, which is determined experimentally. $E(x)$ is then combined with an assumed $v(E)$, yielding a $v(x)$ which, when inserted into Equations (2.14) and (2.15), permits evaluation of terminal current amplitude and phase.

Structural details of the test devices are presented in the next chapter. It is necessary here to know only that the sample consists of a rectifying contact on the surface of semiconductor material consisting of a thin high-resistivity epitaxial layer on a highly conductive substrate.

Poisson's equation in one-dimenstional form is
written as

$$\frac{\partial E}{\partial x} = \frac{q}{\epsilon} \, (N_A(x)-N_D(x) + n_O(x)-p_O(x) + n(x)) \qquad (2.25)$$

The electric field is thus

$$E(x) = \int_x^\infty [N_A(x')-N_D(x') + n_O(x')-p_O(x')+n(x')]dx' \qquad (2.26)$$

For the range of operating conditions of this
experiment, the concentration of excess carriers created
by the electron beam $n(x')$ is small compared to the net
ionized impurity concentration $N_A(x') - N_D(x')$, and is
thus neglected in calculations of the dc electric field.
This assumption will be justified in Chapter 5.

With an applied reverse bias voltage, a region of the
semiconductor sample is virtually depleted of mobile
charge. Numerical calculations[53,54] have shown that the
depletion layer edge is not well defined; the spatial
extent of the space charge layer edge is approximately a
few Debye lengths, where the Debye length is defined as[55]

$$L_D = \sqrt{\frac{\epsilon kT}{q^2(N_A-N_D)}} \qquad (2.27)$$

The depletion edge thus becomes more abrupt as the
ionized impurity concentration increases. For the samples
of this experiment with large applied reverse bias, the

impurity concentration at the layer edge will be on the order of 10^{16} cm^{-3}. The corresponding room-temperature Debye length in GaAs is 0.043 micrometers, i.e., small relative to the sample length. When the epitaxial layer is not fully depleted, however, impurity concentration might be as low as 10^{14} cm^{-3}, and Debye length effects become considerable, since L_D = 0.43 micrometers.

If Debye length effects are small, the depletion layer can arguably be assumed to be totally void of mobile carriers, an approximation originally proposed by Schottky[56] and later developed by Shockley[57] for abrupt asymmetrical p-n junctions. (2.25) and (2.26) then become

$$\frac{\partial E}{\partial x} = \frac{q}{\epsilon} (N_A(x) - N_D(x)) \qquad (2.28)$$

$$E(x) = \frac{q}{\epsilon} \int_x^{x_0} [N_A(x') - N_D(x')] dx' \qquad (2.29)$$

and the junction voltage V and the depletion width x_0 are related by

$$V(x_0) = \frac{q}{\epsilon} \int_0^{x_0} \int_{x'}^{x_0} [N_A(x) - N_D(x)] dx dx' \qquad (2.30)$$

where the junction voltage is the sum of the junction built-in potential V_{bi} and the externally applied bias V_{bias}. In Chapter 5 E(x) is computed for the samples of

this experiment using these equations.

In order to illustrate qualitatively the variation of the shape of the electric field profile with bias voltage, we consider the simple case in which the net ionized impurity concentration is constant throughout the epitaxial layer, with a substrate of infinite conductivity. The electric field strength decreases with depth according to

$$E(x) = \frac{q}{e} (N_A - N_D)(x_o - x) \qquad x < \ell \qquad (2.31)$$

where the depletion width X_o is given by

$$x_o = \sqrt{\frac{2\epsilon V}{q(N_A - N_D)}} \qquad (2.32)$$

The depletion width increases with increasing V, until at some point the entire sample length is depleted. Let us denote the voltage corresponding to this "punch-through" condition as V_o. Further increasing V causes the average electric field in the sample (which is equal to V/ℓ) to increase accordingly, while the depletion width remains constant. The electric field distribution is shown in Figure 2.8 for a junction voltage less than, equal to, and greater than V_o.

When the junction voltage is less than V_o, an undepleted region of length $\ell - x_o$ exists within the
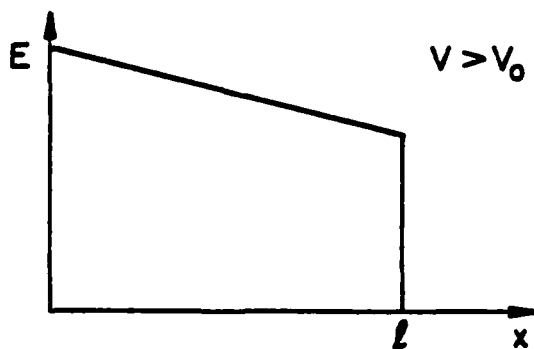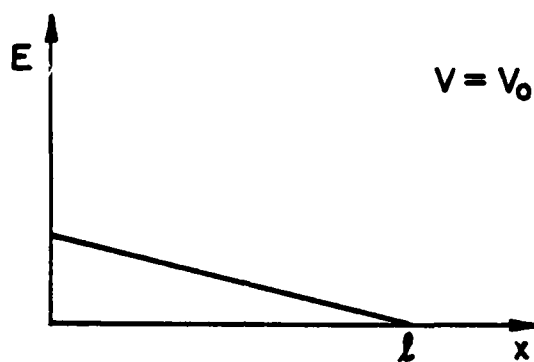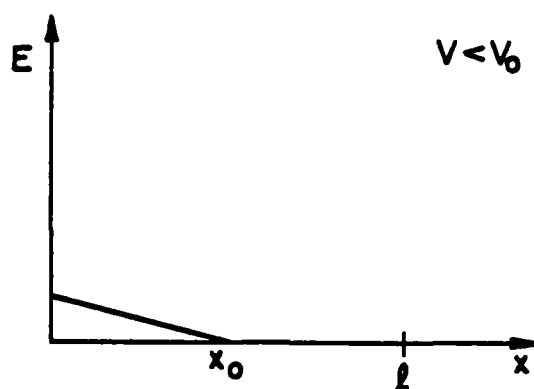
Figure 2.8. Sample electric field distributions for junction voltages less than, equal to, or greater than "punch-through" voltage V_0.

sample, producing an associated series resistance which prohibits accurate measurement of the terminal current. This phenomenon is discussed further in Chapter 5. For the present experimental work, we have attempted to operate within the regime where V is greater than V_o.

Analysis of experimental data is tractable only when electric field non-uniformity is a second order effect. It is therefore advantageous to minimize the variation in electric field across the sample, or field taper, defined by

$$\Delta E = \frac{q}{\epsilon} (N_A - N_D) \ell \qquad (2.33)$$

This is accomplished by using thin samples of high resistivity (corresponding to low ionized impurity concentration). The field taper is a constant; as average electric field increases, the ratio of taper to average field, and hence the effect of field taper, are reduced.

Once the electric field as a function of distance is known for a particular sample, the effect of field non-uniformity on measured terminal current amplitude and phase can be investigated. Since $v(x)$ must be known to apply Equations (2.14) and (2.15), it is obtained by combining $E(x)$, derived from C-V measurements, with an assumed equilibrium $v(E)$, yielding $v(E(x))$. Obviously, this type of analysis assumes that carriers respond instantaneously to the electric field. Transient effects

are thus neglected here, but could be incorporated by running a one-dimensional Monte Carlo simulation with position dependent electric field.[58] Transient effects might be important when the duration of a transient is comparable to the transient time, or when the spatial extent of a transient is of the same order as the sample length. In particular, transient effects would be important in a 1 micrometer GaAs sample with an applied field of approximately 10 kV/cm.

Since we must assume a v(E) dependence, we can determine only the effect of field taper on measured quantities for the assumed v(E) characteristic. An approximate v(E) is generally sufficient to estimate the magnitude of this effect, which is usually insensitive to small variations in assumed v(E) curves.

It is important to realize that the degree to which velocity varies across a given sample is a function of both the electric field distribution and the velocity-field characteristic. In fact, if velocity varies slowly with field (as in GaAs at high fields), then the error in measurement of carrier velocity introduced by field non-uniformity can be small.

Amplitude and phase are calculated according to (2.14) and (2.15). A piecewise linear v(x) is assumed, allowing the inner integral to be evaluated analytically. The outer integration is then performed numerically. Details of the method are presented in Appendix A, along

with the Fortran Program "CALC" used to perform the calculations.

In order to illustrate qualitatively the effect of field (and hence velocity) non-uniformity, program "CALC", was run at 10.6 GHz for a velocity which decreases linearly with position, by a total of 0.2×10^7 cm/sec over a distance of 5.0 micrometers. This v(x) might arise in a sample in which E(x) decreases linearly with distance if the velocity-field characteristic is linear with positive slope over the range of electric fields existing within the device.

Results are plotted in Figure 2.9. Calculated phase and amplitude differ substantially from those predicted by Equations (2.16) and (2.17) for the constant velocity case. The phase does not step discontinuously by 180 degrees at an amplitude minimum. The amplitude at a minimum is non-zero (as predicted in Section 2.2.3) and the velocity at which both minima and maxima occur is shifted upward. Both amplitude and phase deviate most significantly from the constant velocity values in the vicinity of minima.

In Chapter 4 the effect of field non-uniformity is determined for the test devices of this experiment using the computer program "E" listed in Appendix A. Given the reverse bias voltage, a piecewise linear doping profile and a piecewise linear assumed v(E), the program first calculates E(x) using Equations (2.29) and (2.30), then
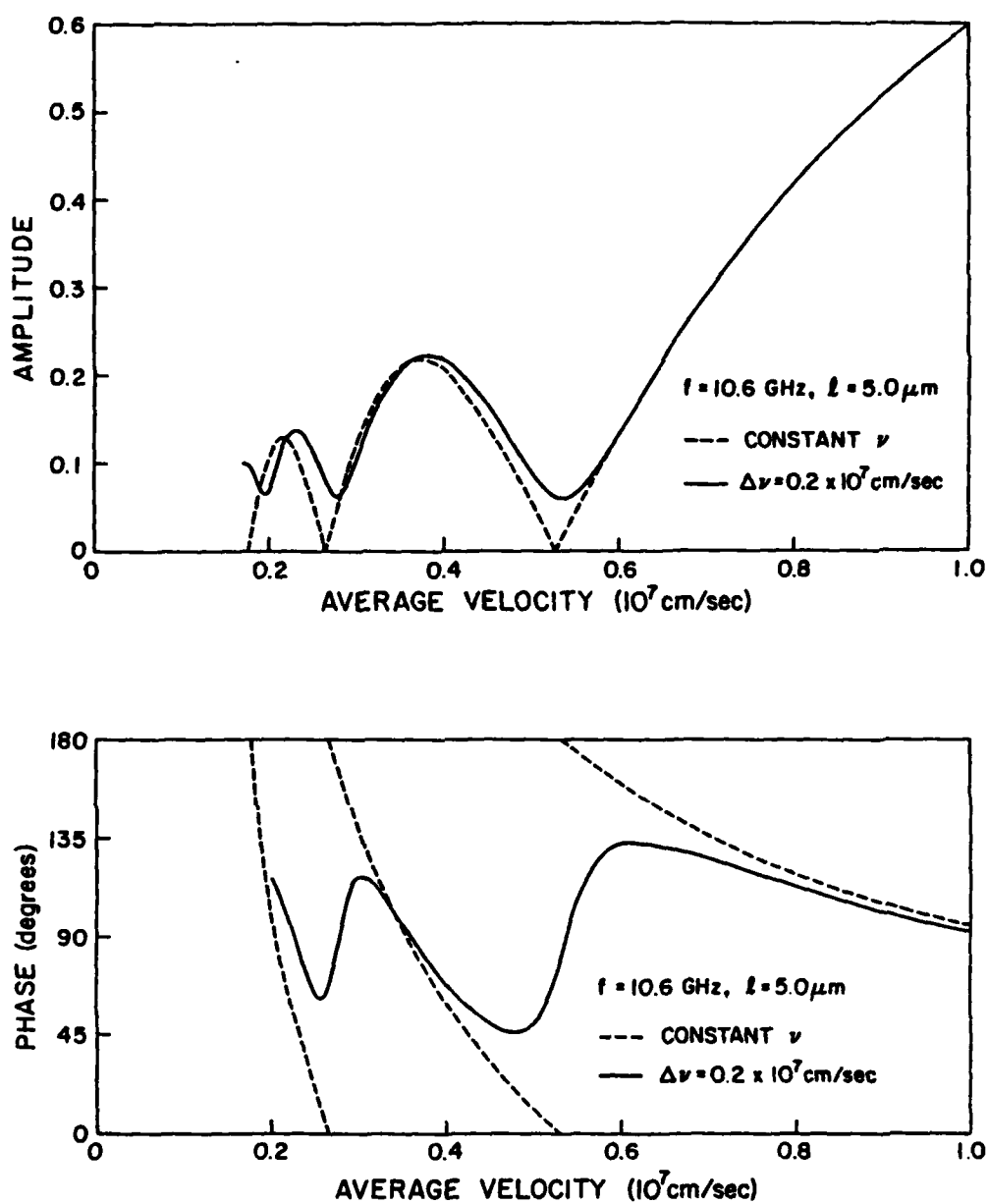
Figure 2.9. Calculated 10.6 GHz amplitude and phase vs.
average carrier velocity for a 5 μm sample with
velocity taper $\Delta v = 0.2 \times 10^7$ cm/sec.

combines E(x) and v(E) and evaluates amplitude and phase
in the same manner as program "CALC".

2.4. Diffusion

When the spatial distribution of carrier density or
temperature in a material is non-uniform, a pressure
gradient exists which acts to move the distribution toward
uniformity. In this experiment, charge packets should
therefore spread as they traverse the sample (Figure
2.10a). In Figure 2.10b, the effect of such packet
dispersion on the terminal current waveform is
illustrated. In the absence of diffusion, the current
rises as carriers are created at the surface, and falls at
the same rate upon collection a time τ later. When
diffusion is present, the current begins to fall sooner,
and does so more gradually, corresponding to the rate at
which the broadened packet is collected. In this example,
it can be shown from Fourier analysis of the terminal
current that the component of current at the fundamental
frequency is displaced earlier in time. If diffusion were
neglected, a measured phase shift would thus lead to a
calculated value of experimental drift velocity higher
than the true value.

As discussed in Chapter 1, the transport equations
derived from kinetic theory reduce to much simpler forms
under certain conditions. In particular, carrier velocity
is given by
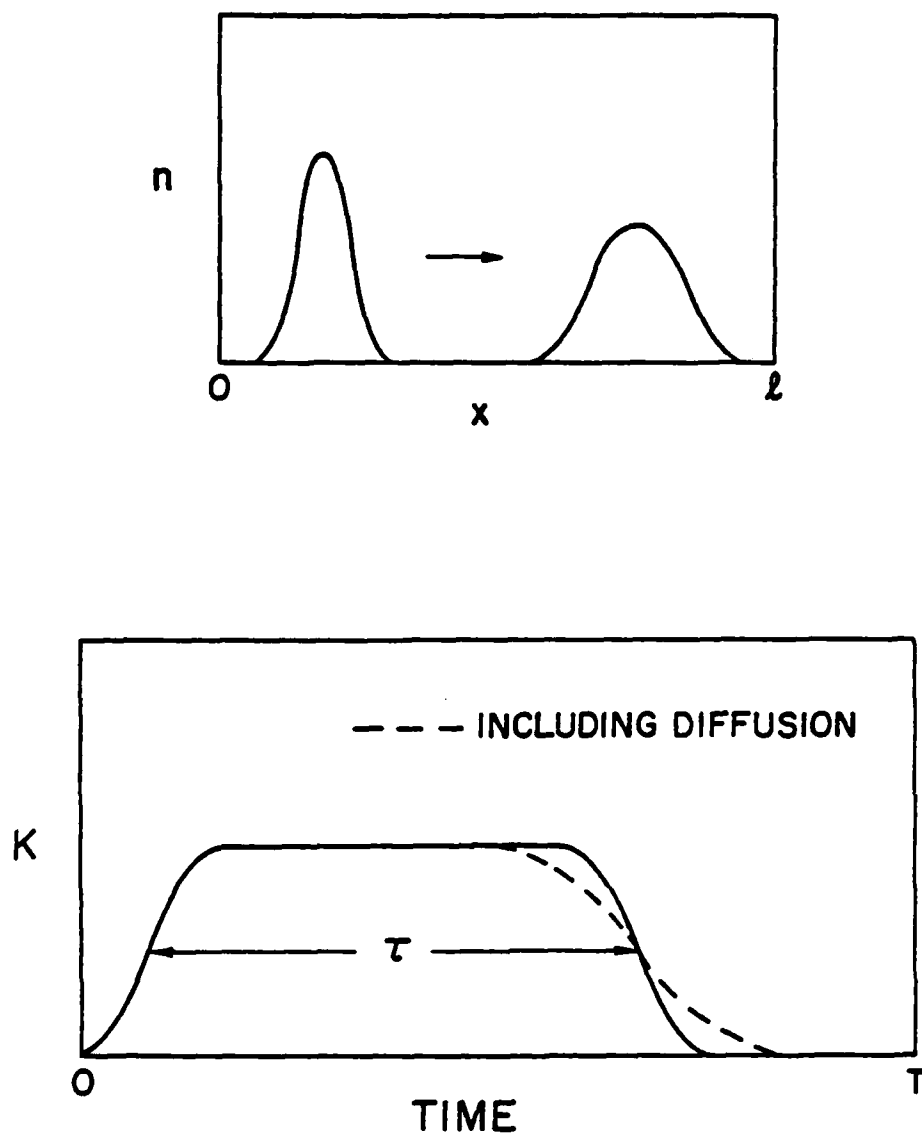
Figure 2.10. Effect of diffusion on a) carrier distri-
bution and b) terminal current waveform.

$$\vec{v} = \mu(E)\vec{E} + \frac{D(E)}{n} \vec{\nabla}n \tag{2.35}$$

where mobility and diffusivity are field-dependent quantities. This equation was assumed to be correct in previous measurements[34] of high-field diffusivity. In fact, the more conventional time-of-flight technique takes the initial carrier distribution to be a delta function, which then evolves into a Gaussian.[34] We assume only that a diffusion current flows which is proportional to the gradient in carrier concentration, i.e.,

$$\vec{J}_{diff} = -qD(E) \vec{\nabla}n \tag{2.36}$$

which is applicable to any carrier distribution. Although Equation (2.35) may not be strictly correct, we are still able to measure values of $\mu(E)$ and $D(E)$ for the conditions of this experiment. We denote diffusivity determined in this fashion as "spreading" diffusivity.

It is obvious that application of (2.35) to any physical system requires that the spatial distribution of carriers be known. Since in our experiment this distribution depends on details of the incident electron beam modulation, a computer simulation is utilized to accurately model the experimental conditions. The incident electron flux as a function of time is computed, as is the motion of carriers within the smaple due to the

applied field and carrier gradients, leading to a
predicted terminal current waveform. Fourier analysis of
this current and the incident electron flux provides the
necessary phase and amplitude information.

If we take carrier gradients in planes parallel to
the sample surface to be small with respect to gradients
in the x-direction, then the problem becomes one-
dimensional. For typical experimental values of σ = 13.9
mils and r = 5 mils, the beam intensity at any instant
varies by a maximum of 23% across the surface of a sample.
For the transit times occurring in this experiment,
carrier concentration varies by a comparable amount across
the thickness of a sample. However, since the sample
diameter is normally at least 25 times the sample length,
transverse concentration gradients can be neglected and
(2.35) becomes ·

$$v = \mu(E) \ E + \frac{D(E)}{n(x)} \frac{dn(x)}{dx} \qquad (2.37)$$

In order to calculate the flux of beam electrons
striking the sample surface as a function of time, the
shape and motion of the beam, and the geometry and
location of the sample must be known.

Since our beam is Gaussian (see Chapter 3), it has a
density of the form

$$\rho(\vec{r}) = \frac{I_o}{2\pi\sigma^2} \, e^{-\frac{|\vec{r}-\vec{r}_o|^2}{2\sigma^2}} \tag{2.38}$$

where I_o is the total beam current and $\vec{r}_o$ is the position of the beam center. Both I_o and σ can be varied in our experiment by changing the voltages applied to various electron gun grids.

Using the coordinate system of Figure 2.11, the position of the beam center r_o in the plane of the sample can be written as

$$\vec{r}_o = A \sin(\omega_o t)\hat{z}. \tag{2.39}$$

A is the deflection amplitude and ω_o is the resonant angular frequency of the microwave deflection cavity. Combining (2.38) and (2.39), we have

$$\rho(y,z,t) = \frac{I_o}{2\pi\sigma^2} \, e^{-\frac{[y^2 + (z - A \sin(\omega_o t))^2]}{2\sigma^2}} \tag{2.40}$$

which describes the beam intensity as a function of both position and time.

At any specified time, Equation (2.40) can be numerically integrated over the area of the sample, yielding total incident beam current. Results of such an integration for parameters typical of this experiment are shown in Figure 2.12. Not that in 2.12a, with the sample positioned at the center of the beam deflection (i.e.
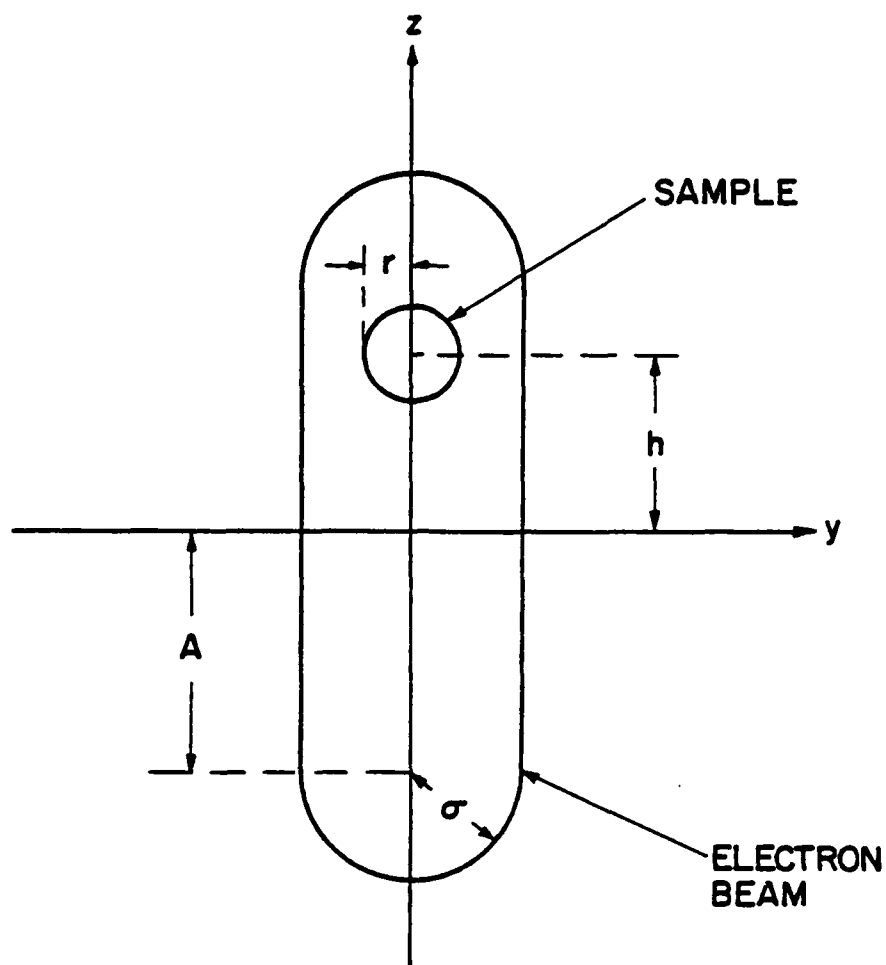
PARAMETERS

σ = HALF WIDTH OF BEAM
A = AMPLITUDE OF BEAM DEFLECTION
r = SAMPLE RADIUS
h = z-COORDINATE OF SAMPLE CENTER

Figure 2.11. Illustration of parameters used in computation of incident electron flux waveform.
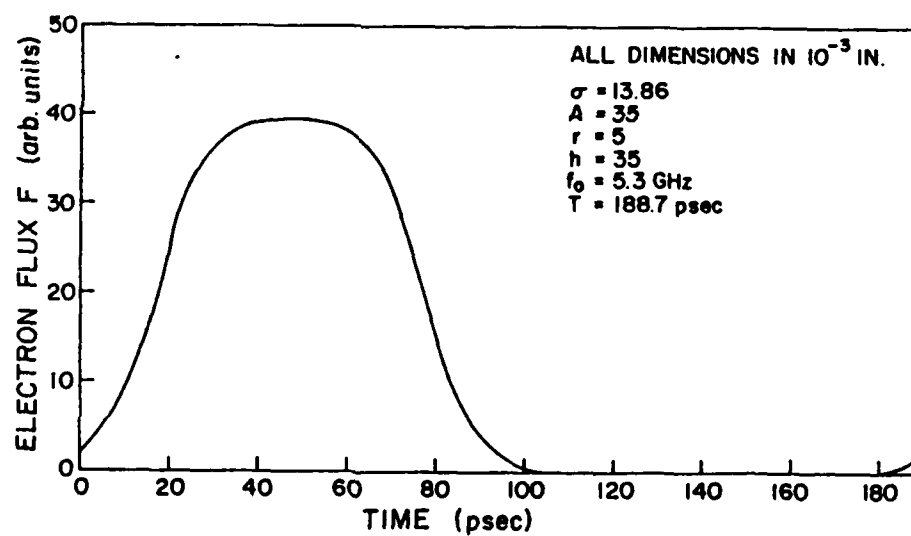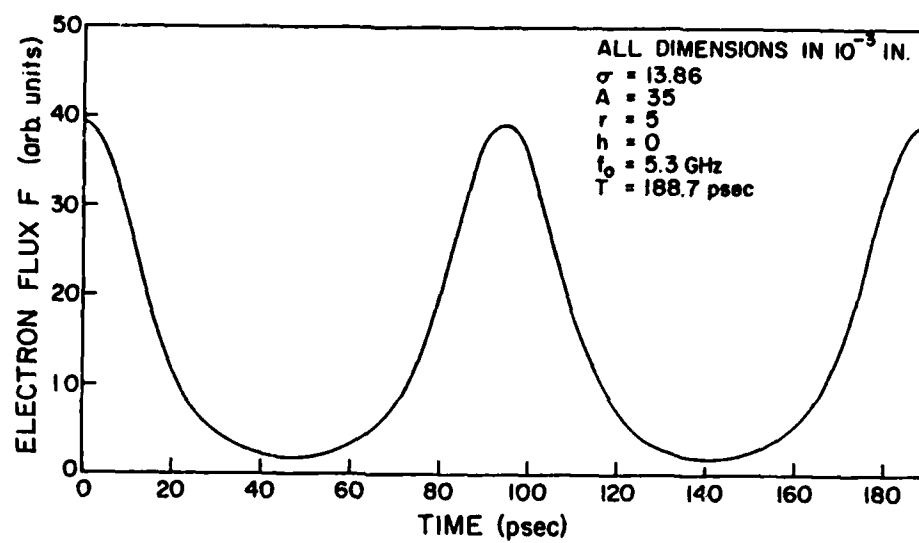
Figure 2.12. Calculated incident electron flux waveforms.

a) h = 0 (10.6 GHz fundamental). b) h = 35 x 10^{-3} in.

(5.3 GHz fundamental).

h = 0), the beam sweeps over the sample twice per microwave deflection cycle. The period of the resultant incident electron flux is thus halved, its fundamental frequency doubled. Certainly, in neither of the two cases shown is the bombarding electron pulse "instantaneous", as required for the more conventional time-of-flight technique.

The spectral composition of both computed incident beam current waveforms is listed in Table 2.1. Since the magnitude of some of the higher harmonics is appreciable, measurements of those components may provide important information, e.g., amplitude minima not occurring at lower frequencies.

If F(t) is the primary electron flux in units of charge/m^2-sec, then the current density jsut below the sample surface is equal to

$$J(x_o, t) = MF(t) \tag{2.41}$$

where M, the multiplication, is given by[60]

$$M = \frac{\eta E_a}{e_p} \tag{2.42}$$

We shall see in Chapter 3 that a number of possible test devices exist. As a consequence, the surface rectifying contact may consist of simply a metallization, a

a) h = 0

FOURIER ANALYSIS OF INCIDENT BEAM CURRENT

FREQ(GHZ)	MAG(UA)	PHASE(DEG)
DC	0.1148E+00	
10.6	0.1390E+00	179.942
21.2	0.4863E-01	-0.070
31.8	0.1179E-01	179.883
42.4	0.2172E-02	0.140
53.0	0.3190E-03	179.363
63.6	0.3646E-04	4.765
74.2	0.5459E-05	73.999
84.8	0.4219E-05	-174.486
95.4	0.7838E-05	48.898
106.0	0.3395E-05	-176.623

b) $h = 35 \times 10^{-3}$ in.

FOURIER ANALYSIS OF INCIDENT BEAM CURRENT

FREQ(GHZ)	MAG(UA)	PHASE(DEG)
DC	0.1036E+00	
5.3	0.1640E+00	179.999
10.6	0.7311E-01	-0.002
15.9	0.3894E-02	-179.977
21.2	0.1703E-01	179.983
26.5	0.1016E-01	-0.027
31.8	0.1374E-02	179.912
37.1	0.1235E-02	179.993
42.4	0.6699E-03	-0.074
47.7	0.4035E-04	178.572
53.0	0.7897E-04	-178.764

Table 2.1. Spectral composition of incident electron flux for a total beam current of 10 μA. a) h = 0. b) $h = 35 \times 10^{-3}$ in.

metallization and an oxide, or a metallization and a thin low-resistivity semiconductor layer. η represents the fraction of primary electrons which penetrate this material, and E_a is defined as the average energy of the transmitted electrons. These quantities have been experimentally determined for thin metal layers[61] and oxide-semiconductor systems.[62] e_p, the energy required to produce an electron-hole pair, is equal to 3.6 eV in silicon and 4.6 eV in gallium arsenide.[60] For the case of a 200 Å chromium Schottky contact on GaAs, $\eta = 0.3$, $E_a = 1.65$ keV and the resulting multiplication is approximately 100.

Equation (2.41) is valid if the secondaries are created within a distance of the surface which is much shorter than the sample length, and this phenomenon occurs quickly relative to the carrier transit time. This approximation is discussed further in Chapter 5.

Carriers move with a velocity given by (2.37). Our numerical simulation of carrier motion uses the equation

$$\frac{dn(x,t)}{dt} = -v(x)\frac{dn(x,t)}{dx} + D(x)\frac{d^2n(x,t)}{dx^2} \qquad (2.43)$$

to reevaluate $n(x,t)$ at each mesh position after a time interval Δt. Certain numerical aspects of the simulation, such as pseudodiffusion and stability, are discussed in Appendix A. The current density is computed acccording to

$$J(x,t) = qn(x,t)v(x) - qD(x) \frac{dn(x,t)}{dx} \qquad (2.44)$$

Finally, the terminal current is calculated from

$$K(t) = \frac{a}{\ell} \int_{0}^{\ell} J(x,t)dx \qquad (2.45)$$

Both terminal current and incident electron flux are subsequently Fourier analyzed, yielding amplitude and phase of each frequency component of terminal current relative to the corresponding harmonic of the incident beam current.

The simulation was initially performed for the case of no diffusion (D = 0) so that results might be compared with predictions of the analytical theory. Terminal current waveforms are shown in Figure 2.13 for three different sample lengths. The current waveform peaks are shifted relative to the incident flux, the time shift being equal to one-half the transit time, or $\ell/2v$. Fourier analysis of these waveforms indicates that the amplitude and phase of the first five harmonics agree with values predicted by equations (2.16) and (2.17) to within computational accuracy, the largest discrepancy being less than 0.1%. We have seen, then, that the duration of the incident electron pulse can be comparable in length to the period of oscillation. In fact, each frequency component of the induced terminal current will satisfy the
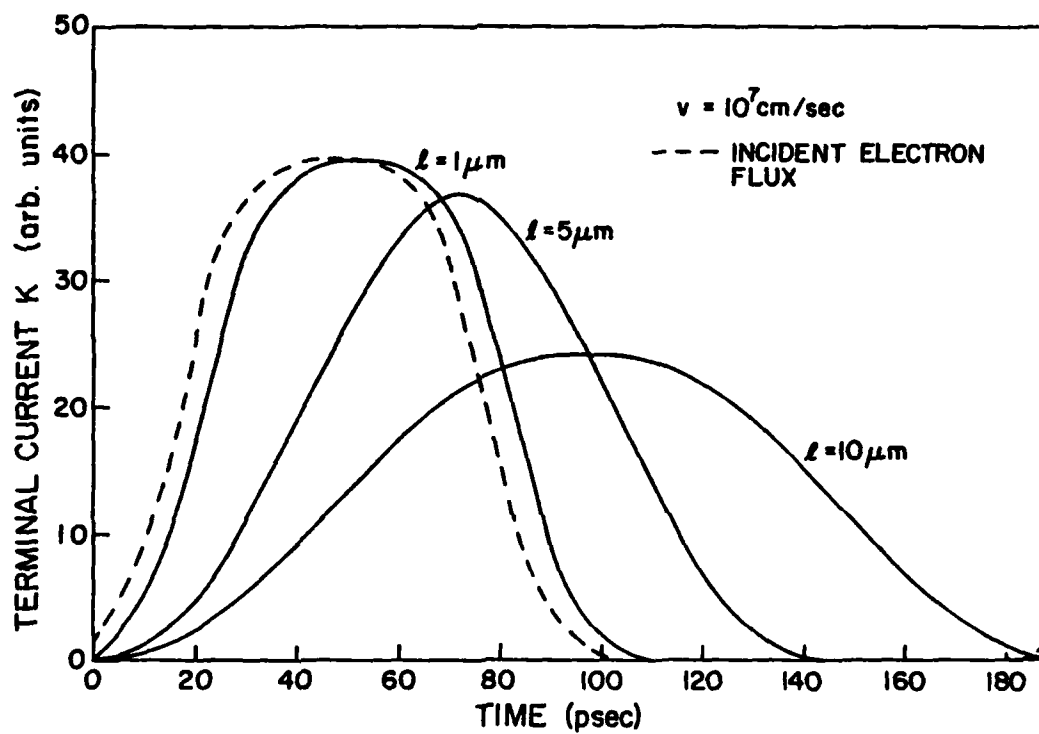
Figure 2.13. Simulated terminal current waveforms for sample lengths of 1, 5 and 10 μm, with f_0 = 5.3 GHz

analytical equations for any choic` of periodic incident beam current.

Finite diffusion was then introduced into the simulation; the effect of spreading diffusion on the terminal current waveform is illustrated in the example of Figure 2.14. The 10.6 GHz amplitude and phase as functions of drift velocity are given in Figure 2.15 for a 5.0 micrometer sample with a diffusivity of 20 cm^2/sec. The amplitude minimum occurring at a velocity of 0.53 x 10^7 cm/sec is non-zero, as in the non-uniform electric field case of seciton 2.3, but in the present results the position of the minimum is not shifted. In addition, amplitude peaks have been lowered by diffusion.

A number of simulations were performed; parameters which were varied include drift velocity, sample length, diffusivity and frequency. This work led to the following conclusions:

1.   The fractional change in phase, and thus the shift in apparent velocity $v = \omega \ell/2\phi_{meas}$ is greater for thin samples since spreading is proportional to $\sqrt{t}$ whereas the distance traveled is proportional to t. Measured "apparent" velocity-field curves will thus be functions of sample length.

2.   The deviation of both amplitude and phase from non-diffusing case (D = 0) increases with increasing diffusivity D.
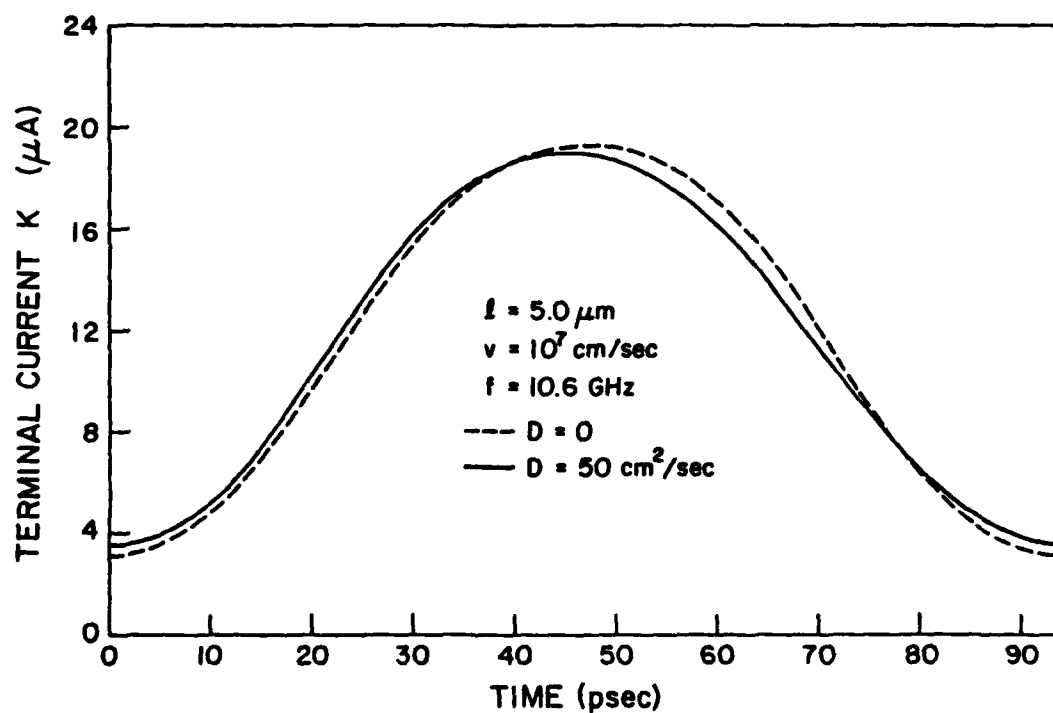
Figure 2.14. Effect of 50 cm^2/sec diffusivity on the terminal current of a 5 μm sample having carrier velocity v = 10^7 cm/sec.
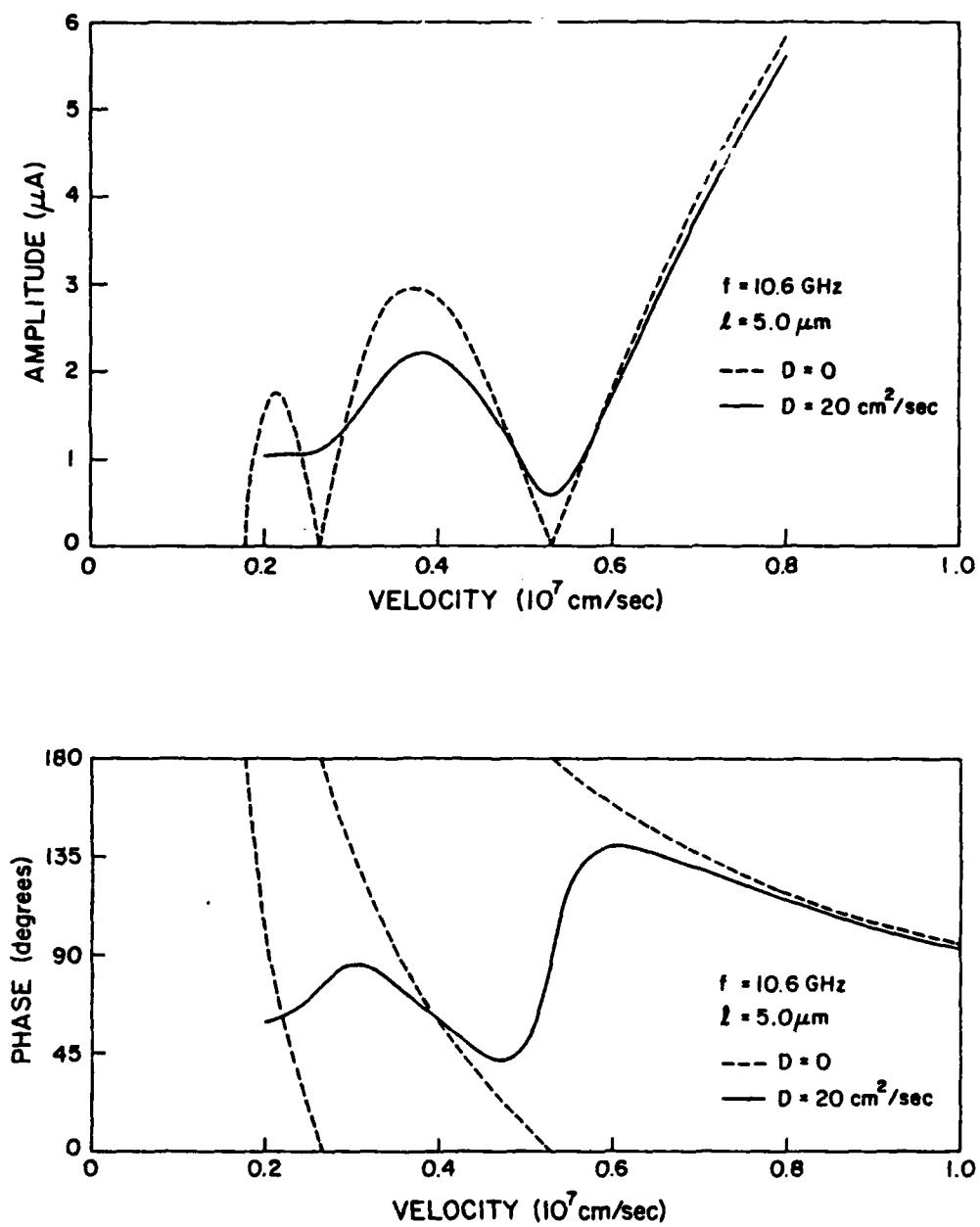
Figure 2.15.   Dependence of 10.6 GHz amplitude and phase on carrier drift velocity for a 5 µm sample with D = 20 cm^2/sec.

3. The effect of diffusion is larger when drift velocity
    is small, since carrier gradients are larger and
    transit time increases.

4. In general, diffusion has a more pronounced effect on
    10.6 GHz results than on 5.3 GHz results for a
    specified length and velocity due to larger carrier
    gradients.

5. Diffusion causes the amplitude at a minimum to be
    non-zero. The degree to which the minimum is
    "smeared" increases with increasing diffusivity. In
    Chapter 4 the simulation will be utilized to
    determine a value for D which matches simulated and
    experimental amplitude responses in the vicinity of
    one such "smeared" minimum.

It should be noted that dE/dx was taken to be zero in
the preceding calculations; hence, both v(x) and D(x) were
assumed to be constant. A second version of program
"EXPT" was then written to include $v(E(x))$ and $D(E(x))$.
The program is essentially a combination of programs "E"
and "EXPT". Given the sample doping profile n(x), v(E)
and D(E), E(x) is first computed, then values of v and D
are assigned to each mesh point and carrier motion is
simulated. The execution time of this program is more
than 20 times that of the simpler "EXPT". For the input
parameters $\ell = 5\,\mu m$, $\Delta x = .02\,\mu m$ and $\Delta t = .05$ psec,
execution time on an LSI 11 microcomputer increased from

25 minutes to 10 hours when v(x) and D(x) were added. Although it is recognized that a single program including both E-field non-uniformity and diffusion is probably the most exact treatment, it is felt that the required computer time is prohibitively long. Consequently, these two secondary effects are examined separately, using programs "E" and "EXPT". This approach is considered valid since it was discovered that adding the phase shifts due to E-field taper and diffusion computed separately yields a total phase shift almost exactly equal to that calculated with the second version of "EXPT", provided the magnitude of the effect is small (i.e. on the order of 10% or less.)

2.5 Summary

In this chapter a comprehensive theory of microwave time-of-flight measurements has been presented. First, general analytical expressions for amplitude and phase of various spectral components of the test device terminal current were derived. When a constant velocity is assumed, these expressions are found to reduce to simpler forms, allowing the dependences of amplitude and phase on velocity for the operating frequencies and typical sample lengths of this experiment to be investigated.

An amplitude of zero is expected when the transit time is equal to an integral number of periods. A quantitative discussion was given which predicts the

amplitude at such a minimum to be non-zero when velocity varies with position or the charge packet shape is modified in any way while in transit.

The effects of non-uniform electric field and diffusion on measured quantities were analyzed. In general, electric field non-uniformity and diffusion were seen to similarly alter the terminal current for the examples given. Methods were developed which allow the magnitude of these effects in experimental samples to be evaluated; results of such analyses appear in Chapter 4.

CHAPTER 3

EXPERIMENTAL APPARATUS

A block diagram of the microwave time-of-flight
experiment has already been presented in Chapter 1;
photographs of the apparatus appear on the following two
pages. In this chapter individual components of the
experimental system are described, the discussion
focusing on certain aspects such as the requirements,
design and operation of the various components.

3.1 Semiconductor Samples

3.1.1. Requirements

Semiconductor samples used in the microwave time-
of-flight experiment must satisfy several requirements.
The selected structure must allow large, preferably
uniform electric fields to be produced within a region
of fixed length with minimal current flow.

To achieve these conditions, non-injecting contacts
are formed on the surface of semiconductor material
consisting of a high-resistivity epitaxial layer on a
highly conductive substrate. Rectifying contacts, when
reverse biased, permit the epitaxial layer to be fully
depleted of mobile charge, and an electric field
configuration such as that shown in Figure 2.9a

66

Figure 3.1. Microwave time-of-flight experimental system.
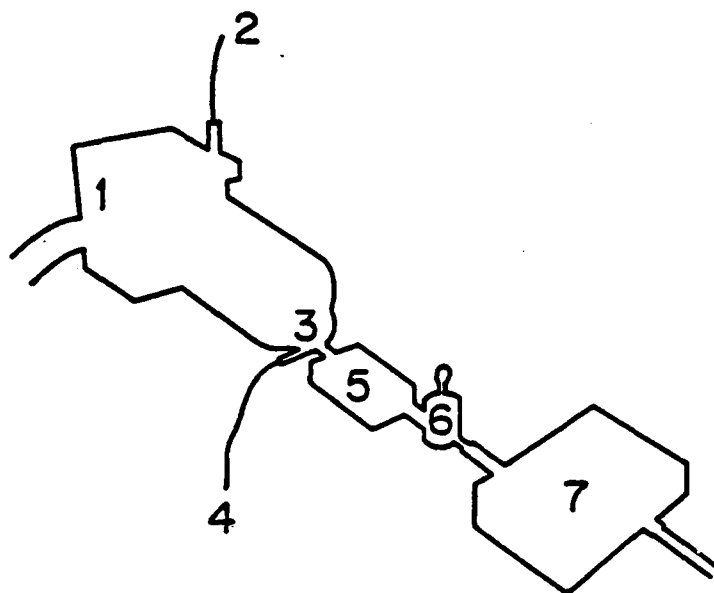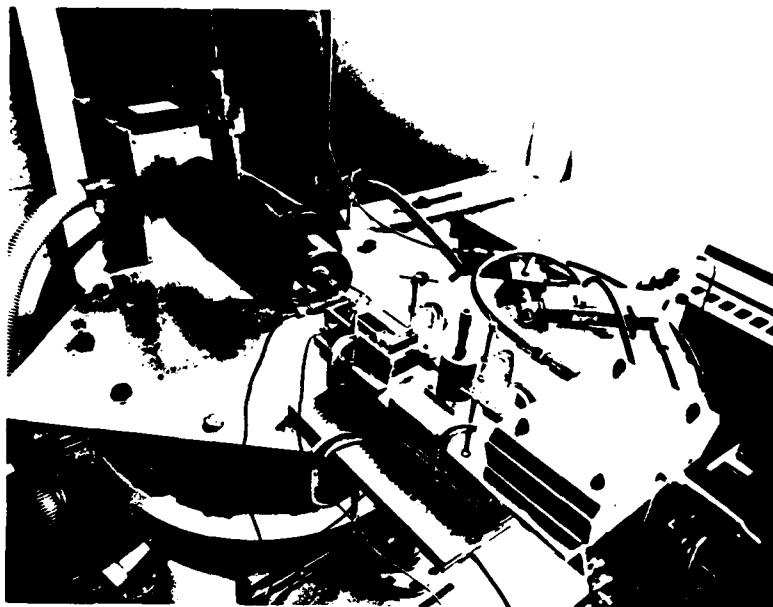
1 Electron gun
2 Input to microwave deflection cavity
3 Sample holder
4 Sample bias
5 GaAs FET amplifier
6 10.6 GHz transmission cavity
7 Harmonic frequency converter

Figure 3.2. Detailed view of experiment section.

established. The surface contact region must have a low
stopping power for incident beam electrons. The
following test configurations may be used:

1. Schottky barrier

2. p-n junction

3. MIS (metal-insulator-semiconductor) structure

The Schottky barrier is by far the simplest
structure to fabricate, since it consists solely of a
surface metallization. In some cases, however, barrier
heights may be too low for use in this experiment (as in
p-type silicon).

An abrupt asymmetric p-n junction can be used,
provided the surface layer is very highly doped so that
it will not be totally depleted, and sufficiently thin
to allow transmission of an appreciable number of beam
electrons. For the beam energy of this experiment (2.5
kV), a thickness of approximately 500 $\overset{o}{A}$ is acceptable,
although in some cases difficult to obtain. To reduce
series resistance, the surface is normally coated with a
very thin layer of metal.

An MIS structure has been successfully used by Ruch
and Kino[34] in a conventional time-of-flight experiment
to measure electron velocity in GaAs. However, since
the insulator capacitance is typically much larger than
that of the sample, the bias voltage must be pulsed so
as not to charge the insulator. In addition, carrier
transit time must be less than the time constant of the

insulating layer. Another disadvantage of this structure is that beam electrons must penetrate both metal and insulator.

A diode is considered suitable for use in the experiment only if it possesses a reverse leakage current which is small (i.e. a barrier height which is large[63]). Since reverse breakdown due to avalanche phenomena limits the maximum field at which microwave time-of-flight measurements are possible, a high breakdown voltage is desired. Edge effects in planar Schottky diodes may cause premature breakdown.[64] This situation can be improved by employing a mesa or inverted mesa structure[65] as well as a guard ring.[66]

3.1.2 Preparation

In this section we describe the design and fabrication of test diodes of n-type silicon and gallium arsenide, and p-type silicon.

A circular sample geometry was selected as the most appropriate for use with a Gaussian electron beam. A top view of the sample is shown in Figure 3.3a. The chip is square, .025" (.633 mm) on edge. The test device is circular with a diameter of .015" (.381 mm). A 2500 Å thick gold ring defines the central target area, since it has a large density-thickness product (i.e. stopping power) and is essentially opaque to incident beam electrons. The circular target area is
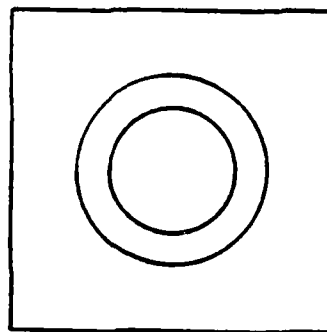
a) Top view
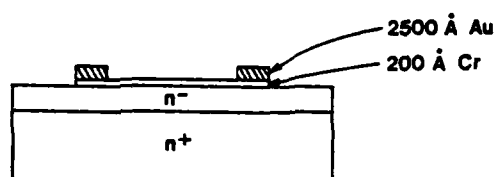
b) Planar Schottky (n-GaAs)
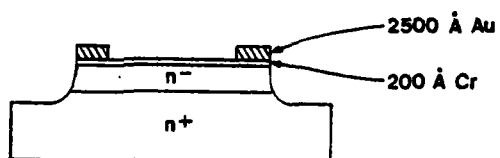
c) Mesa Schottky (n-Si)
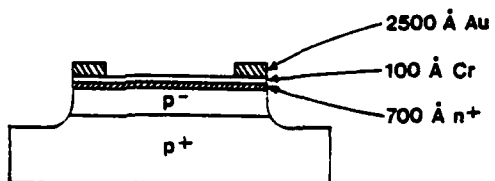
d) Mesa p-n (p-Si)

Figure 3.3. Top view and cross-sections of various test structures.

.010" (.254mm) in diameter, and is covered by a thin (100-200 Å) layer of metal.

The sample size was chosen to satisfy two important criteria: first, chips are required to fit into X-band microwave diode packages. Second, the sample diameter should be much larger than the sample length, so that edge effects can be justifiably neglected.

Chromium was selected as the metallization for Schottky barrier test structures on n-type silicon and gallium arsenide because continuous chromium layers as thin as 40 Å can be thermally evaporated. In addition, chromium has a work function of 4.6 eV,[67] and Cr contacts to n-type silicon or gallium arsenide have barrier heights of 0.7 to 0.8 volts. Other advantages of chromium are that it is insensitive to moderate temperatures such as those encountered during bonding (300-400ºC), and it has a lower density (7.2 grams/cm^3) than most other metals, and is therefore more transparent to the incident beam.

In the present work three different device structures were used; these are shown in Figure 3.3. A planar Schottky barrier was employed on n-type GaAs (Figure 3.3b), after attempts at producing mesa structures with sufficiently high breakdown voltages failed. However, it was found that the mesa structure did indeed considerably improve the characteristics of Schottky barriers fabricated on n-type Si (Figure 3.3c).

Barrier heights of metal contacts to p-type silicon are low (on the order of 0.20 to 0.25 volts[68]); consequently a mesa p-n structure was necessary to obtain acceptable p-Si samples (Figure 3.3d).

The starting wafers were as follows:

n-type Si: (111)n-/n$^+$ wafers with epitaxial layers approximately 5 micrometers thick were purchased from Semimetals, Inc.

n-type GaAs: (100) n-/n$^+$ wafers were obtained from two sources: Fujitsu Corp. furnished several vapor phase epitaxial (VPE) layers approximately 7 micrometers thick, liquid phase epitaxial (LPE) layers 2 and 3 micrometers thick were grown at Cornell University.

p-type Si: (111) n$^+$p$^-$p$^+$ material was provided by Texas Instruments, Inc. The p$^-$ test region has a thickness of roughly 10 micrometers. The n$^+$ layer is about 700 Å thick with a doping of 10^{19}/cm^3.

Many of the n-type layers were initially thinned to facilitate measurements at a number of different sample lengths. The devices were fabricated using standard photolithographic techniques; a detailed account of the wafer processing appears in Appendix B. Wafers were then scribed and broken into individual die. After visual inspection and checking device I-V

characteristics using a Tektronix type 576 curve tracer
and associated probe station, a few of the best devices
(i.e., high breakdown, low leakage) were mounted in
Interceram model #AV-170 X-band Gunn diode packages
(Figure 3.4a) with Epo-Tek H20-E conductive epoxy. This
two component silver-filled epoxy was subsequently cured
at 150°C for 20 minutes. Finally, wires were bonded
from the package upper lip to the gold ring on the
sample, as shown in Figure 3.4b. n-type samples were
wirebonded at 300°C with a Kulicke and Soffa
thermocompression bonder, whereas wirebonding to the p-
Si samples was performed with a Westbond ultrasonic
bonder at room temperature.

3.1.3   Characterization

I-V characteristics were once again observed with a
curve tracer to determine whether the bonding procedure
had altered device performance. In general, breakdown
voltages changed by less than .5%. Breakdown voltage,
defined here as the voltage at which reverse leakage
current exceeds 20 microamperes, is shown in Table 3.1
for samples of various types and thicknesses. It should
be noted that the current $\underline{density}$ corresponding to this
value of total current is 1.76×10^{-2} amps/cm^2.

Measurements of sample differential capacitance as
a function of reverse bias voltage provide important
information. Specifically, the doping profile,
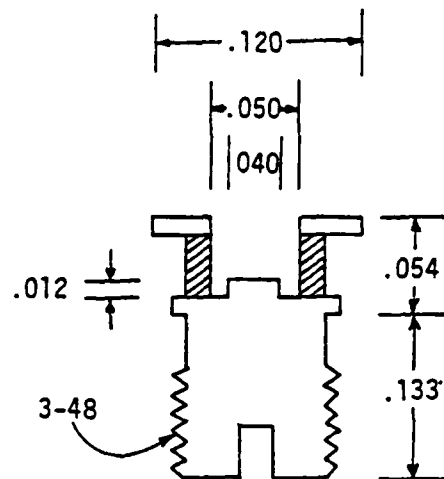
ALL DIMENSIONS IN INCHES
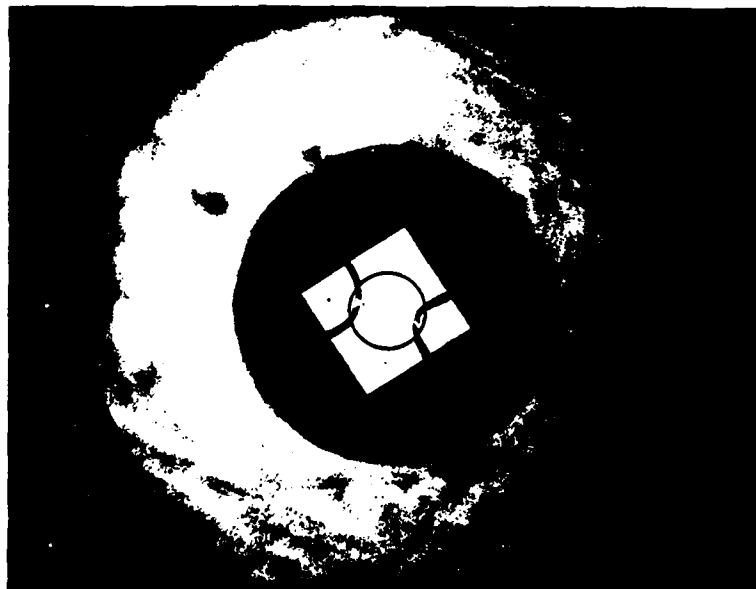
Figure 3.4. Interceram model #AV-170 microwave diode
package.

variation of depletion width (i.e. sample length) with bias voltage, and the junction built-in potential are all determined from C-V measurements. Sample capacitance for a fully depleted 10 micrometer thick layer is on the order of 1.2 pF. Conventional 1 MHz C-V profilers lack the resolution necessary to accurately measure such small capacitances; samples are therefore C-V profiled using an alternative technique, described in Appendix B, which entails measuring the 100 MHz reflection coefficient of a packaged test diode in a coaxial environment. The measurement scheme, in addition to improving resolution and accuracy, has an inherently lower magnitude of undesirable parasitic capacitance than that typically associated with 1 MHz profiling techniques.

C-V measurements were performed on each sample prior to use in the microwave time-of-flight experiment. Depletion width versus voltage and carrier conce ⁻ration versus distance are calculated according to the equations presented in Appendix C. Built-in potential is evaluated from a plot of $1/C^2$ vs V.

In Figures 3.5 - 3.7 we present carrier concentration profiles for a number of samples, each of which is representative of a specific material and layer thickness. The variation of depletion width with bias voltage is shown in Figures 3.8 and 3.9 for two of the samples. The depletion width in n-Si sample #65 is seen
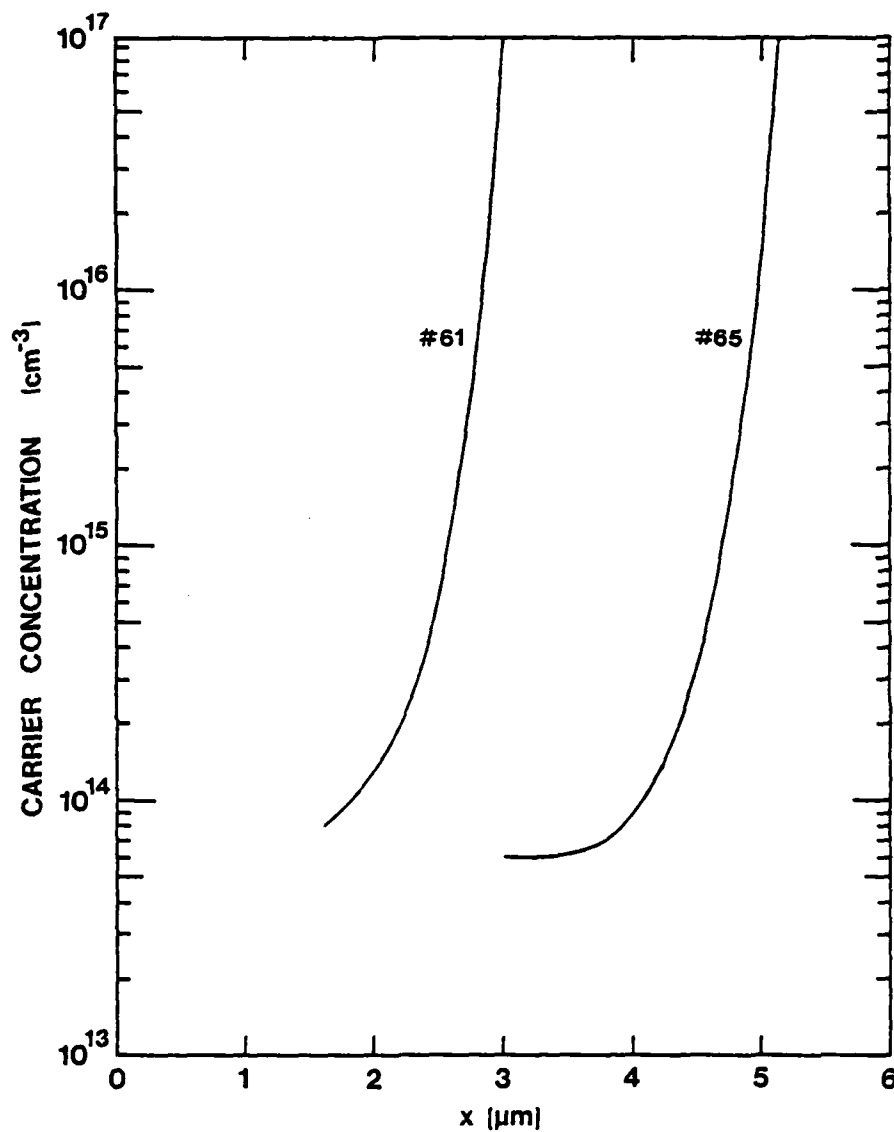
Figure 3.5. Doping profiles of two n-Si samples. #61 was

obtained by thinning a 5 μm epitaxial layer.
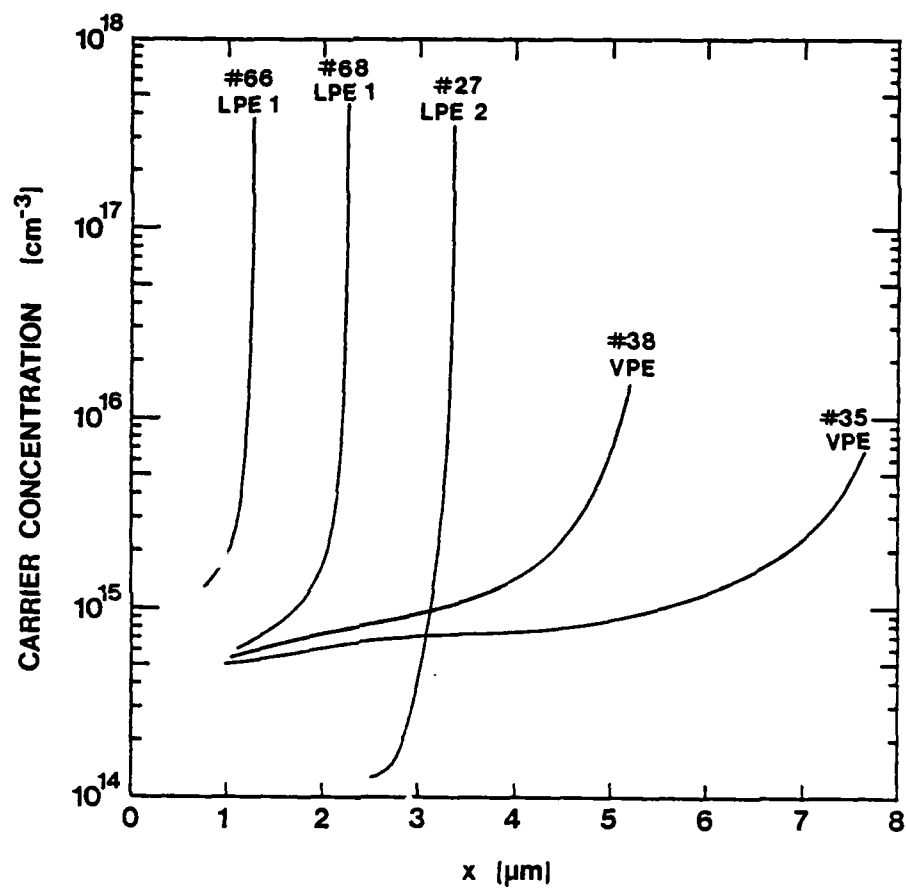
Figure 3.6.   Doping profiles of five n-GaAs samples.   #66

    is a thinned version of #68; #38 is a thinned version

    of #35.
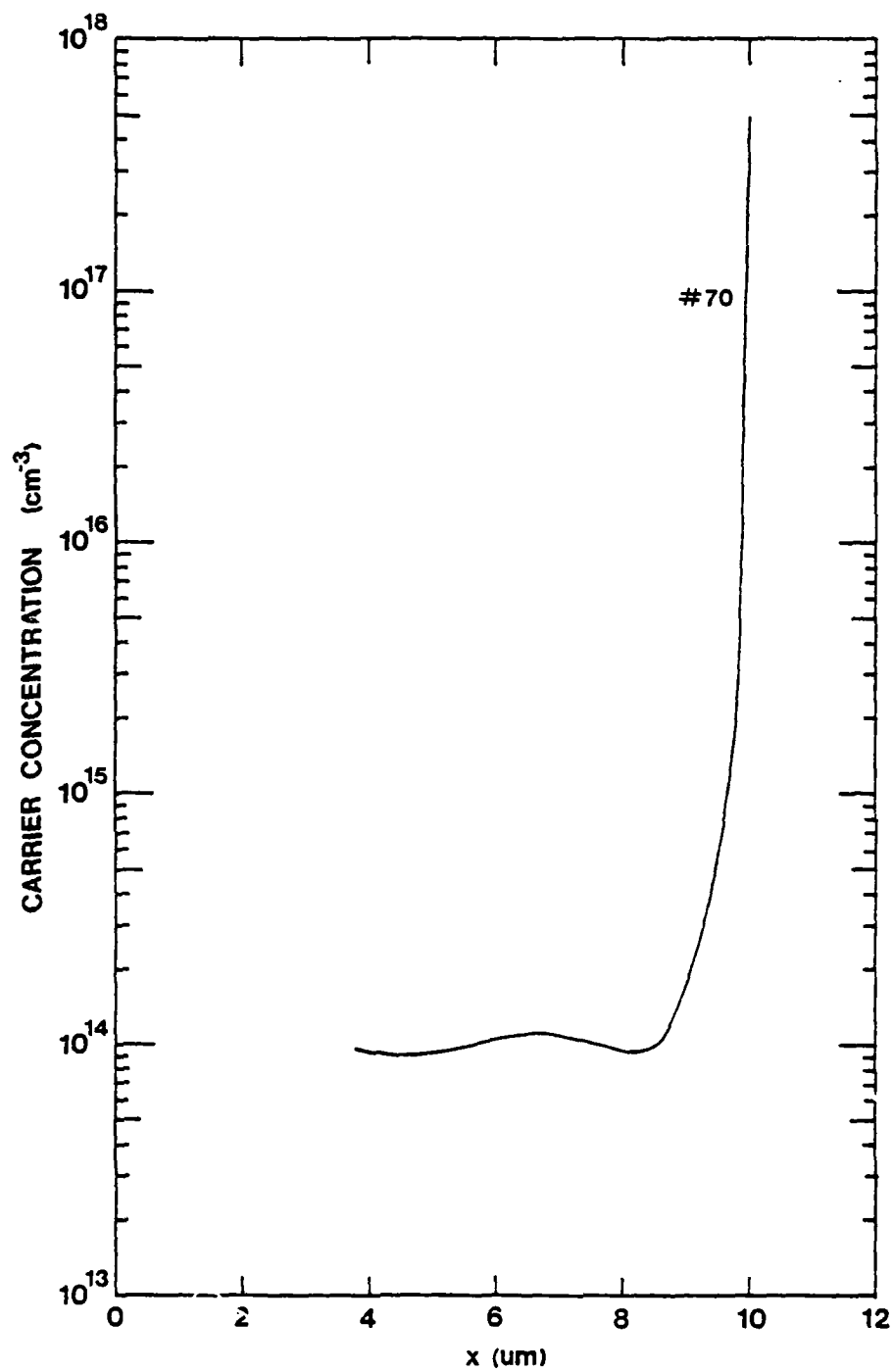
Figure 3.7. Doping profile of a p-Si sample. In this case thinning would have removed the n^+ surface layer.
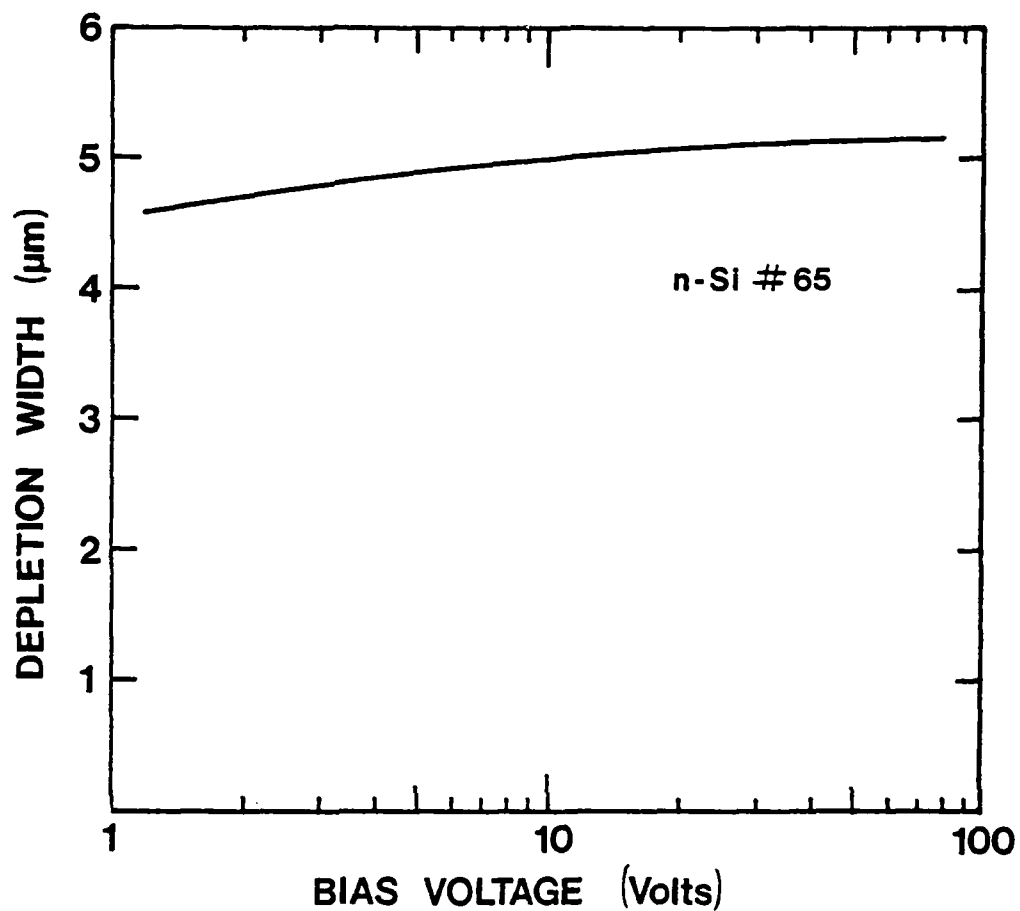
Figure 3.8. Depletion width as a function of reverse bias voltage for n-Si sample #65 of Figure 3.5.

1.0

1.1

1.25

2.8 2.5

3.2 2.2

3.6

4.0 2.0

1.8

1.4 1.6

MICROCOPY RESOLUTION TEST CHART
NATIONAL BUREAU OF STANDARDS 1963 A
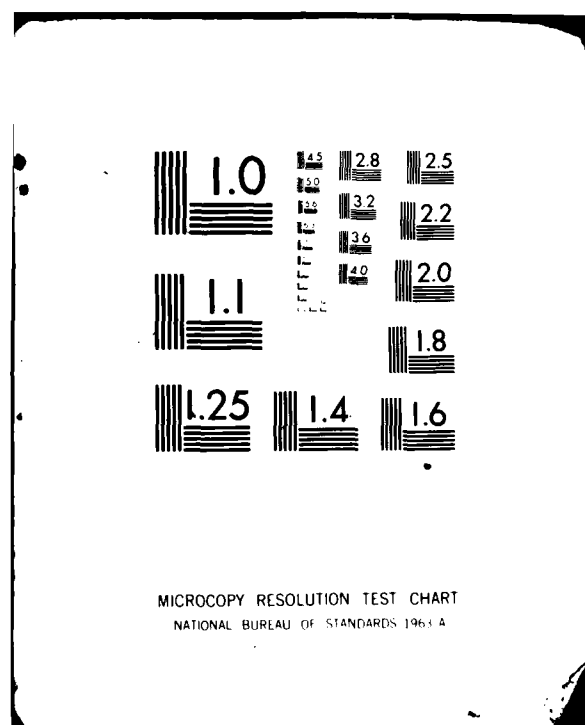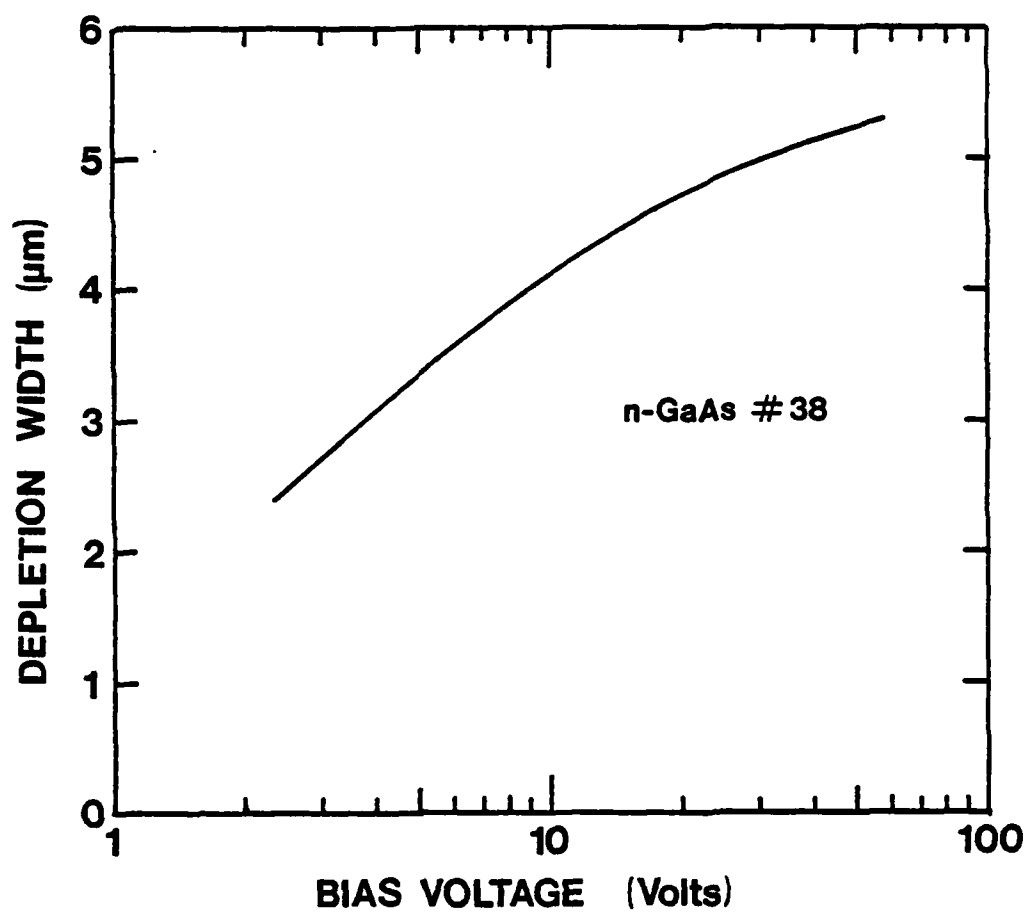
Figure 3.9. Depletion width versus reverse bias voltage
for n-GaAs sample #38 of Figure 3.6.

to be nearly constant with bias voltage, while that of
n-GaAs sample #38 varies significantly.

Electric field profiles computed for these same two
samples with computer program "E", using the carrier
concentration versus distance dependences obtained from
C-V measurements, are shown in Figures 3.10 and 3.11.
The electric field in sample #65 is seen to more nearly
uniform than that in sample #38 for equal values of
average electric field.

Junction built-in voltage, as well as depletion
width and corresponding average electric field at
breakdown, are tabulated in Table 3.1 for the samples of
Figures 3.5 - 3.7.

To summarize, I-V characteristics are used only to
determine suitability for microwave time-of-flight
testing. C-V measurements, on the other hand, provide
information which is essential to the analysis of
experimental data. In particuar, sample length and
built-in potential are critical in determining the
experimental velocity-field dependence. Knowledge of
the carrier concentration permits the solution of
Poisson's equation, yielding the electric field
distribution and hence the degree of electric field non-
uniformity.
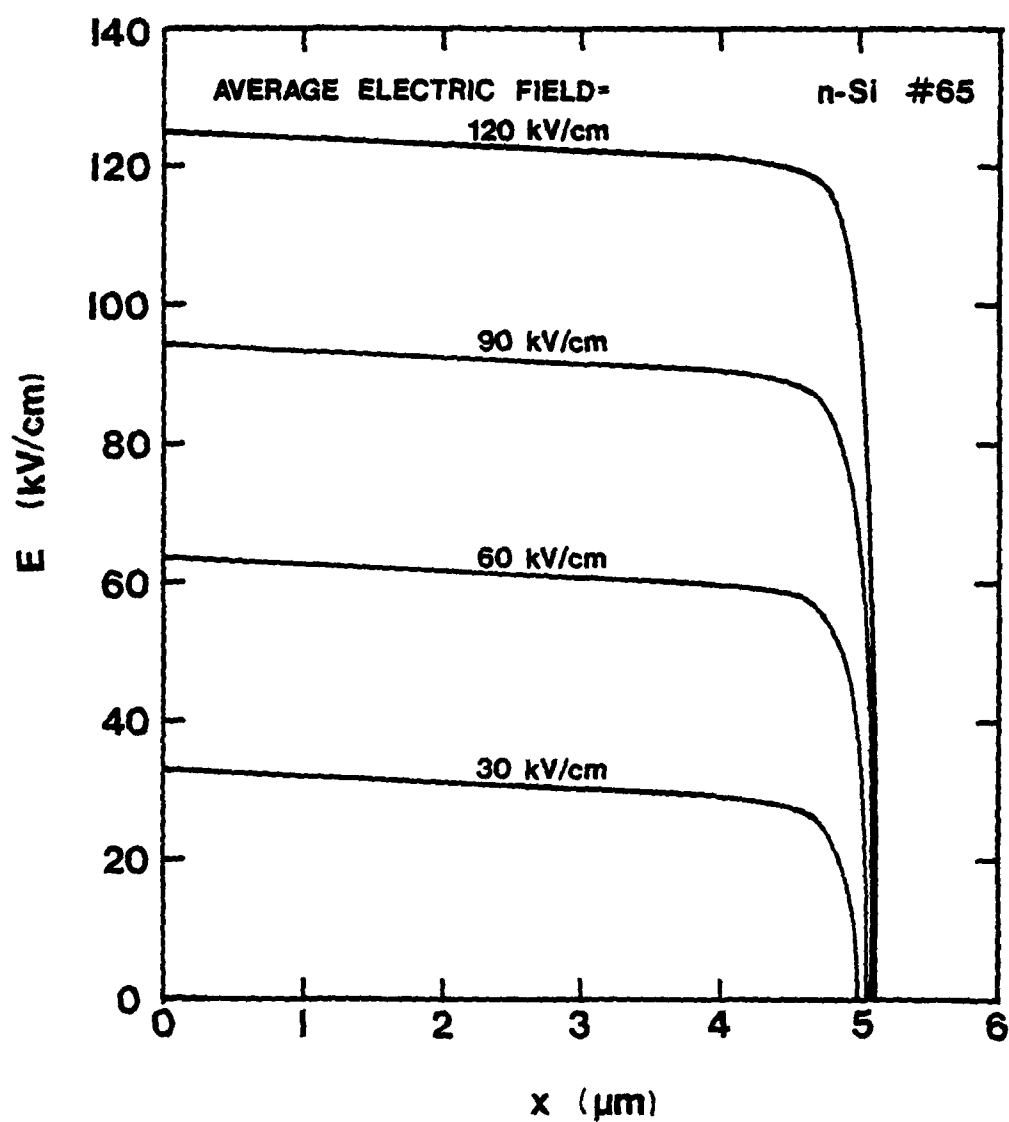
Figure 3.10. E(x) calculated for n-Si sample #65 at
different values of average electric field.
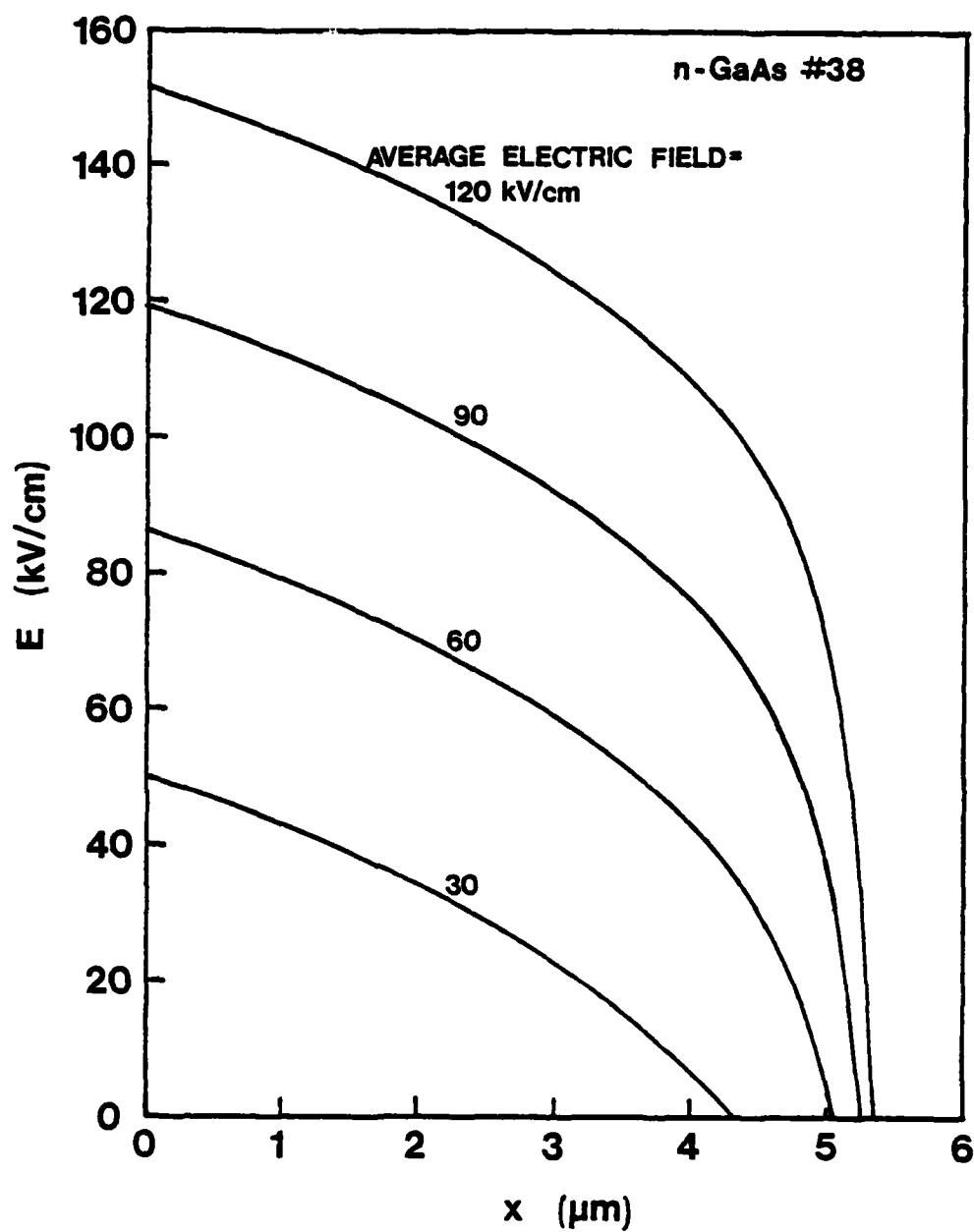
Figure 3.11. E(x) calculated for n-GaAs sample #38 at different values of average electric field.

Table 3.1

Measured Parameters for the Samples of Figures 3.5-3.7.

Sample		V_{br}(volts)	$\ell_{V=V_{br}}$ (μm)	V_{bi}(volts)	E_{max}(kV/cm)
n-Si	#61	40	3.02	0.62	135
	#65	65	5.14	0.58	128
n-GaAs	#66	24	1.28	0.84	194
	#68	45	2.26	0.80	202
	#27	57.5	3.37	0.82	173
	#38	64	5.35	0.68	122
	#35	80	8.01	0.72	101
p-Si	#70	232.5	9.98	0.69	234

3.2. Sample Holder

The sample holder was designed to allow electron beam irradiation of the packaged sample through an aperture, and propagation of the induced electro-magnetic wave along an appropriate transmission line. Thus, the beam end of the sample holder must be maintained at high vacuum, with the opposite end at atmospheric pressure so that microwave test equipment can be connected.

The sample holder constructed for this experiment is illustrated in Figure 3.12. A coaxial transmission line was selected since it is compatible with the cylindrically symmetric diode packages, and permits them to be located at the end of a center conductor. The characteristic impedance of the coaxial line is designed to be 50 ohms over the entire length of the sample holder, in regions of both air and teflon dielectric, so that the sample holder can be mated to 50 ohm microwave components.

With the sample holder cap off, a diode is screwed onto the exposed center conductor end. A gasket formed from .030" diameter indium wire is then carefully placed on the upper lip of the package. The cap is replaced, being tightened as far as the outer coaxial conductor will allow, slightly compressing the indium gasket. The indium thus insures that electrical contact occurs simultaneously at both the inner and outer conductor

TEFLON DIELECTRIC

APERTURE POSITION
ADJUSTMENT

INDIUM
GASKET
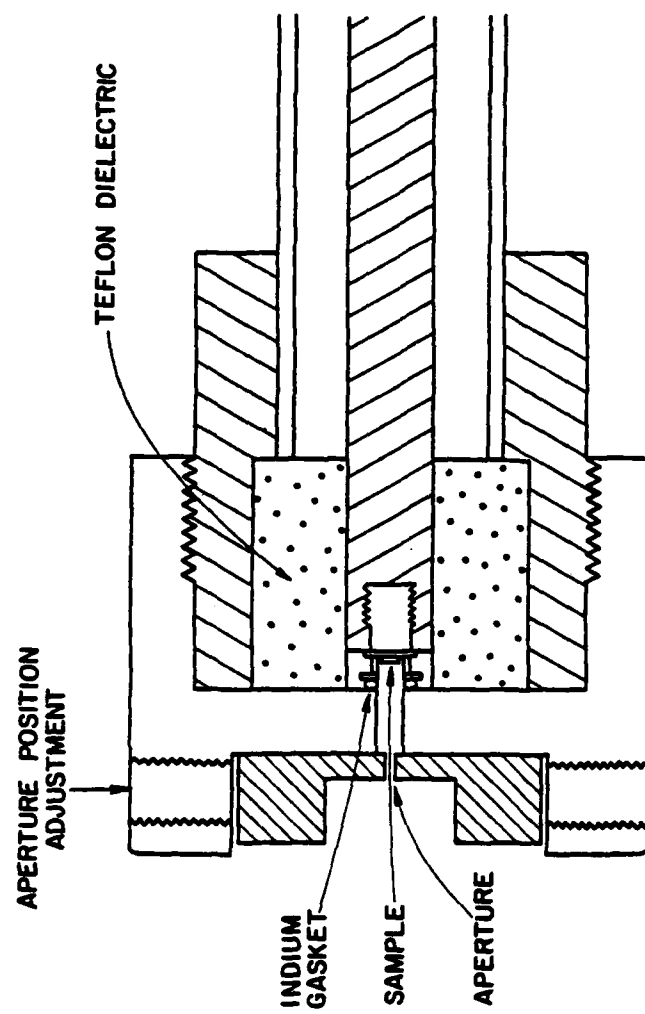
SAMPLE

APERTURE

Figure 3.12. Sample holder (to scale).

surfaces.

The .013" diameter aperture is an integral part of the sample holder, and as a result can be accurately positioned directly in front of the sample target area. This is accomplished by viewing the sample through the aperture at 50x under a metallurgical microscope, and adjusting three positioning screws spaced circumferentially at 120° intervals until both sample and aperture are concentric.

The sample holder <u>assembly</u> is shown in Figure 3.13. There is a female type N connection at one end of the sample holder. The vacuum to air transition is achieved by use of an OSM hermetic seal (with viton O-ring). A type N to OSM adaptor is thus required between the sample holder and the hermetic seal. Finally, the assembled components are encased by a 1" diameter stainless steel tube which can be inserted into a 1 inch "quick-connect" vacuum coupling on the experimental system, a design which enables one to change samples quickly.

3.3 Hewlett Packard Network Analyzer System

Microwave time-of-flight measurements are performed with a Hewlett Packard manual network analyzer system composed of an 8410A network analyzer mainframe, 8413A phase-gain indicator and 8411A harmonic frequency converter. The system is both sensitive and accurate:

VACUUM

1 ATMOSPHERE

1" DIAMETER
STAINLESS STEEL

OSM HERMETIC SEAL

VITON O-RINGS

QUICK-CONNECT

N/OSM
ADAPTOR

SAMPLE
HOLDER

TEFLON
SPACER

e-BEAM
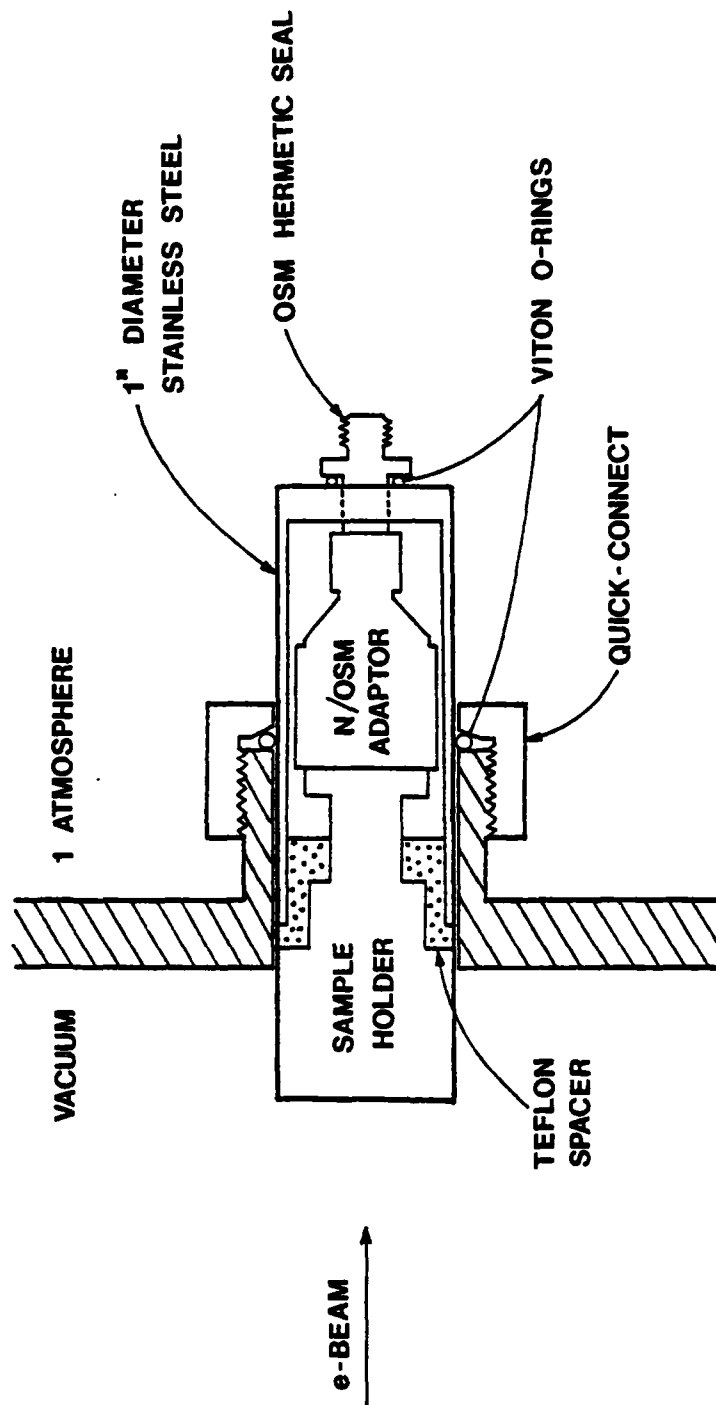
Figure 3.13. Sample holder assembly (not to scale).

test signals between -10 dBm and -78 dBm (system noise level)[8] can be detected, and phase accuracy is on the order of half a degree. The frequency range of the system, in this case 0.11 - 12.4 GHz, is limited by the operating range of the harmonic frequency converter.

In a microwave network analyzer the test signal and a reference signal of identical frequency (and power level between -16 and -44 dBm[69]) are fed into the harmonic frequency converter, which down-converts them to two 278 kHz waves with the same relative phase and amplitude as the original RF inputs. The 8410A network analyzer then evaluates the ratio of test to reference signals and displays the resulting complex quantity on the phase-gain indicator.

3.4. Low Noise Amplifier

Since our test signals are of extremely low power (in the picowatt regime), they must be amplified so that reasonably large signal to noise ratios are obtained. A low noise, high gain amplifier is thus required. A Watkins-Johnson GaAs FET amplifier, designed to provide at least 40 dB gain over the frequency range 8.0 to 12.0 GHz with a 5 dB maximum noise figure, was used.

At 10.6 GHz, one operating frequency of this experiment, this amplifier had a small signal gain of 39.7 dB and a noise figure of 4.3 dB. Gain was found to be constant for supply voltages between 9.5 and 14.0

volts. At 5.3 GHz, the second operating frequency of this experiment, our "X-band" amplifier had a gain of 40.3 dB for supply voltages from 11.0 to 14.0 volts. The same amplifier was thus used at both 5.3 and 10.6 GHz.

3.5 Microwave Deflection cavity

The electron beam is deflected at a microwave frequency by passage through a resonant cavity structure which possesses large electric fields in a direction transverse to the beam axis. We have seen in Chapter 2 that terminal current phase is proportional to frequency, and can thus be resolved more accurately at higher frequencies. The network analyzer functions up to 12.4 GHz. Since measurements are to be made at the cavity resonant frequency and its second harmonic, the deflection cavity should be designed to resonate between 5 and 6 GHz.

The TE_{111} mode in a right circular cylindrical cavity has the correct electric field pattern for transverse beam modulation: at the center plane, the E-field reaches its maximum value and is normal to the axis of the cylinder. Unfortunately, this structure requires large amounts of RF input power to produce sufficiently large electric fields, and hence adequate deflection.

A pair of ridges can be inserted at the center plane of the cavity, as shown in Figure 3.14, to significantly increase the electric field strength attainable with a fixed input power. This is the deflecting structure utilized in the present work. If the ridge separation is smaller than the ridge width the field is virtually constant over a large area, and all portions of the beam are deflected by precisely the same amount, thus preserving the beam shape. In addition, if the ridge thickness is small compared with the distance traveled by the beam during one period of oscillation, then the motion of the beam in the sample plane is sinusoidal in time. Note that the preceding two conditions need not be satisfied to apply the analytical theory set forth in Chapter 2. However, they are essential to our treatment of diffusion via numerical simulation.

Excitation of the cavity is achieved with the coupling scheme illustrated in Figure 3.14b. A loop of copper wire joins the inner and outer conductors at the end of a coaxial transmission line. Current flowing through the loop produces a magnetic field in the appropriate direction for the TE_{111} mode to be excited.

The addition of ridges to any cavity results in a change in the resonant frequencies of the various modes, the largest such shift occurring for modes having electric field patterns which are most significantly
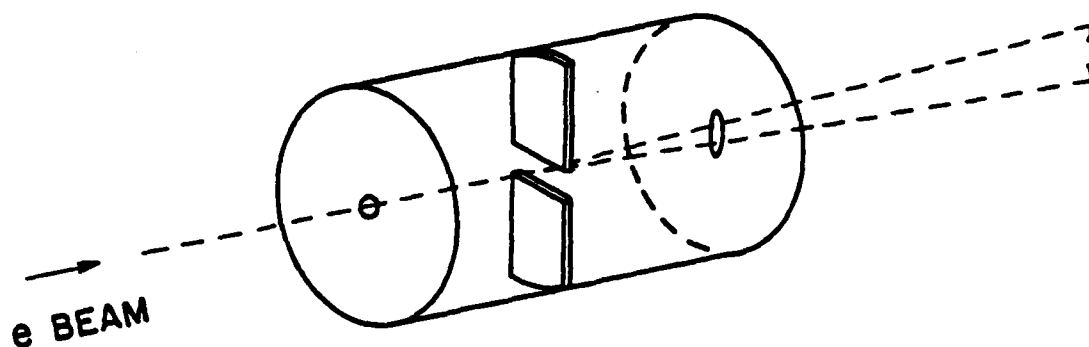
a) Overall view
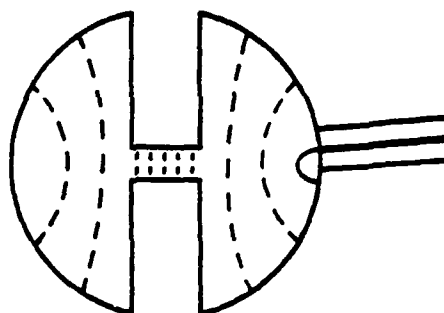
b) Cross-section at center plane

Figure 3.14. Microwave deflection cavity. a) Right cir-
cular cylindrical cavity with ridges inserted at center
plane. b) Cross-section at center plane, indicating
electric field lines.

altered. Although perturbational methods exist which allow calculation of shifts in resonant frequency when small ridges are introduced into a cavity, these are not valid for ridges of our size and narrow separation. An empirical approach was thus taken to design a suitable deflection cavity.

A ridge width of .250 inches and separation of .100 inches were selected to provide a window large enough for the beam to pass through while still maintaining sufficiently high electric fields. A ridge thickness of .0625 inches was also chosen.

It was known that perturbation of cavity electric fields by a conductor (i.e. ridge, tuning screw, etc.) would decrease the resonant frequency.[70] A circular cylindrical cavity of height 1.142 inches and radius 0.563 inches was constructed. The TE_{111} mode of this ridgeless cavity was calculated to resonate at 8.03 GHz. Resonant frequencies of higher order modes were calculated as well.[71,72] Ridges were then introduced into the cavity in stages, the ridge separation being initially equal to the cavity diameter, and thereafter decreased by .100 inch increments until it was equal to the desired .100 inches. This method allows unambiguous identification of each mode, in particular the TE_{111} mode, as ridge separation decreases. At a ridge separation of .100 inches, our first cavity possessed a TE_{111} resonance at 3.65 GHz, which was considered to be

unacceptably low.

A second cavity having height 1.201 inches, radius 0.406 inches, and a computed unperturbed TE_{111} resonance at 9.85 GHz was then constructed. When ridges were inserted with .100 inch spacing, the desired resonance was found to occur at 5.30 GHz, an acceptable value. The size of the coupling loop was then adjusted to optimize external coupling. When critically coupled, all of the incident power is transferred to the cavity, and the cavity reflection coefficient vanishes.

This cavity is used to produce microwave deflection of the electron beam. This deflection, visible with the aid of a phosphor screen, is illustrated in Figure 3.15. The deflection amplitude, equal to one half the total deflection, is dependent upon several parameters, including the drift length, deflecting electric field strength, and electron velocity. Deflection amplitude, measured at the plane of the sample and plotted in Figure 3.16 as a function of cavity input power, is seen to be proportional to the square root of the input power, and hence is directly proportional to the deflecting electric field.

If the field acts upon the electrons for a short time Δt, it imparts to them a transverse velocity

$$v_t = \frac{qE\Delta t}{m} \quad . \tag{3.1}$$
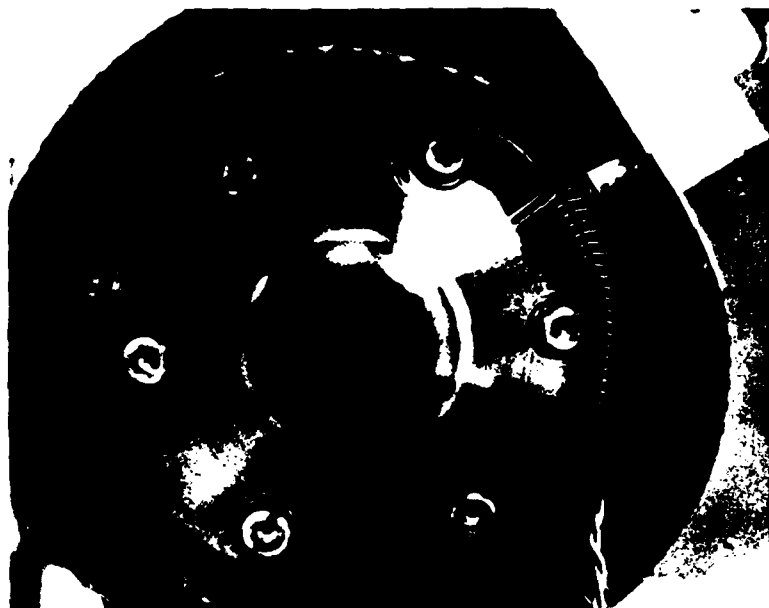
a) No input power
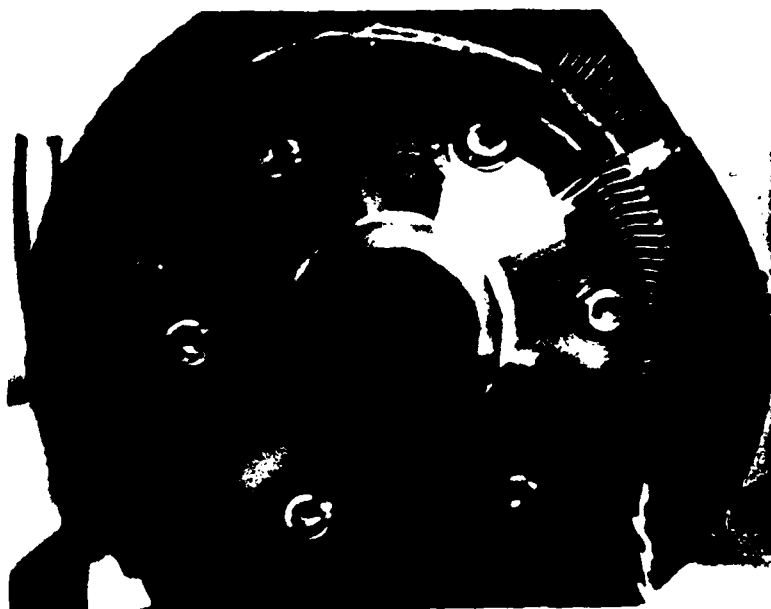
b) Input power = 20 mW

Figure 3.15. Beam deflection, viewed using a phosphor

screen. a) Cavity input power = 0. b) Cavity input

power = 20 mW.
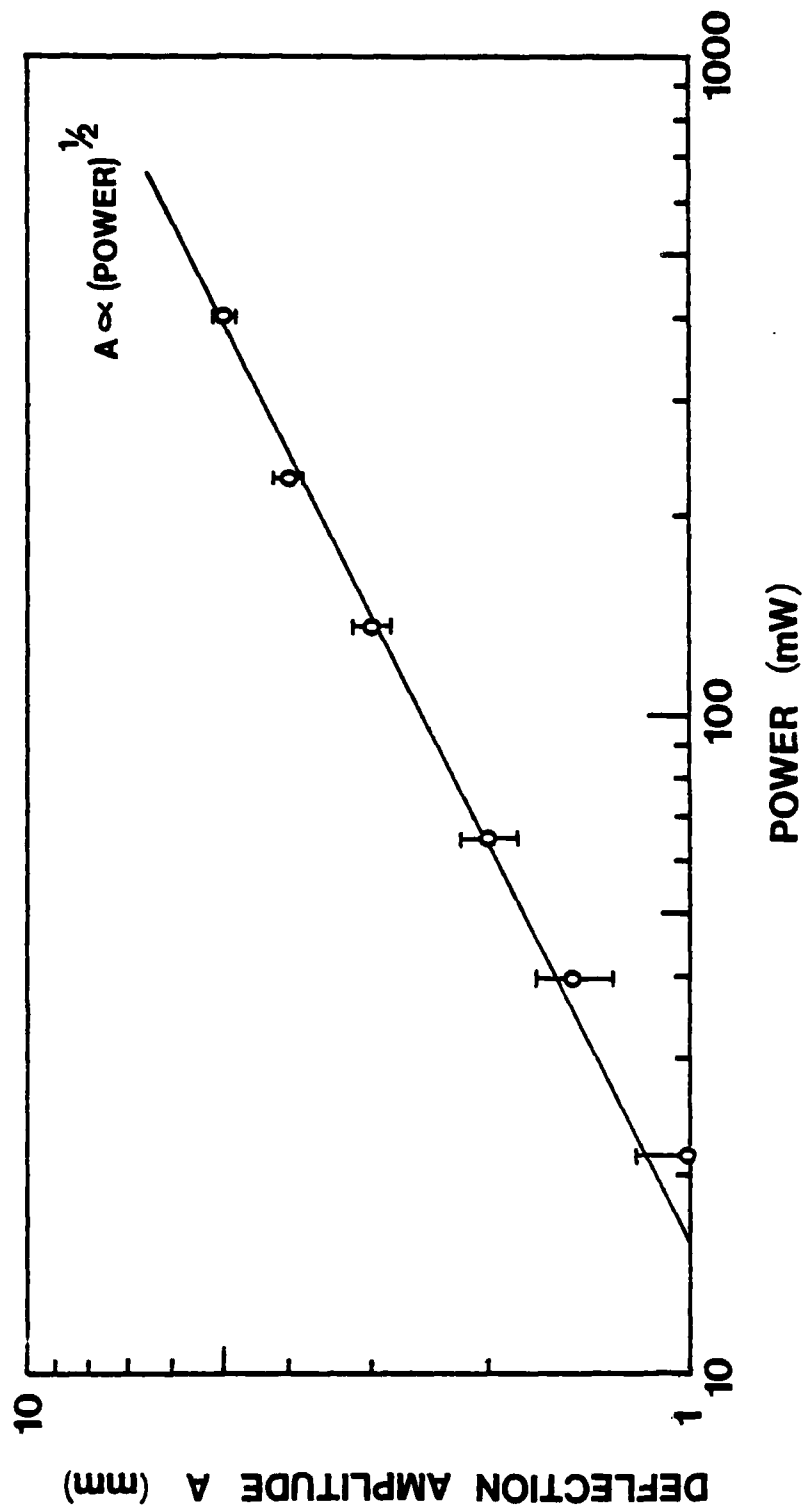
Figure 3.16. Deflection amplitude vs. cavity input power.

This analysis can be extended to derive the following expression for the maximum value of electric field:

$$E = \frac{2VA}{\ell b} \tag{3.2}$$

where

V = beam accelerating potential (2.5kV)

A = deflection amplitude

ℓ = distance from ridges to sample plane (7.25 inches)

b = ridge thickness (.0625 inches).

The electric field and deflection amplitude are indeed linearly related, as already verified experimentally. Furthermore, the maximum electric field can be calculated for normal operating conditions of this experiment, yielding a value of 192 V/cm for a cavity input power of 20 mW.

3.6. Electron Gun

The electron beam produces the secondary carriers whose motion is studied in this experiment. The beam must create an appropriate number of secondaries with appreciable microwave modulation. To achieve this, the beam spot size at the sample should be of the same order of magnitude as the sample size. Beam current must be

large enough to induce measurable test device terminal current, yet sufficiently small to prevent carrier-carrier interaction, heating and other effects associated with large current densities. Additionally, the choice of a suitable beam accelerating potential involves a compromise between the higher multiplication offered by a high beam voltage and the shorter penetration depth resulting from low beam voltages. Finally, simulations of the type described in Chapter 2 require adequate knowledge of the spatial distribution of the beam in a plane transverse to its axis.

For this experiment an accelerating potential of 2.5 kV was considered to be suitable since 2.5 keV electrons do not penetrate too deeply into the semiconductor sample, while still creating an appreciable number of electron-hole pairs. The sample target area is .010 inches in diameter; a beam spot of comparable size at the target would therefore be acceptable, although it is in practice difficult to achieve since the distance from electron gun to sample is approximately 10 inches, and appreciable beam spreading can be expected to occur over such a length. A great deal of effort was expended in an attempt to reduce the spot size.

A model CE-507 electron gun, designed to operate at 2.5 kV, was purchased from Cliftronics, Inc.[73] The gun contains a thorium coated iridium emitter which does not require an activation cycle, nor is it poisoned by

exposure to air after use, as are most other emitters. The gun is sealed into a 1-7/16 inch diameter glass tube and is mounted on the system with a "quick-connect" vacuum coupling.

Electrical connections to the various grids are shown in Figure 3.17. Grid currents are small; a voltage divider therefore provides bias voltages for the cathode, modulator and first anode. Note that the experimental system is grounded, while the emitter is maintained at -2.5 kV. The filament draws approximately 5 amperes of current at 2.0 to 2.5 volts, supplied by a 6.3 volt lead-acid battery capable of holding a charge of 90 amp-hours. As filament voltage is increased, emitter temperature rises and electron emission, and hence beam current, increase.

Total beam current is also controlled by the modulator grid (also known as the extractor cup), which is biased negatively with respect to the emitter. As the modulator grid voltage is made more negative, fewer emitted electrons are extracted and beam current therefore decreases.

The gun also possesses both x and y deflection plates, these being necessary to properly align the beam with the microwave deflection cavity,. Deflection is "balanced", meaning that voltages on opposing plates are of equal magnitude but opposite sign. A simple op-amp circuit mirrors the voltage applied to one plate of each

1 Filament/Cathode (2500 V)
2 Modulator Grid (2525 V)
3 First Anode (2040 V)
4 Second Anode (Ground)
5 X-Deflection Plates
6 Y-Deflection Plates
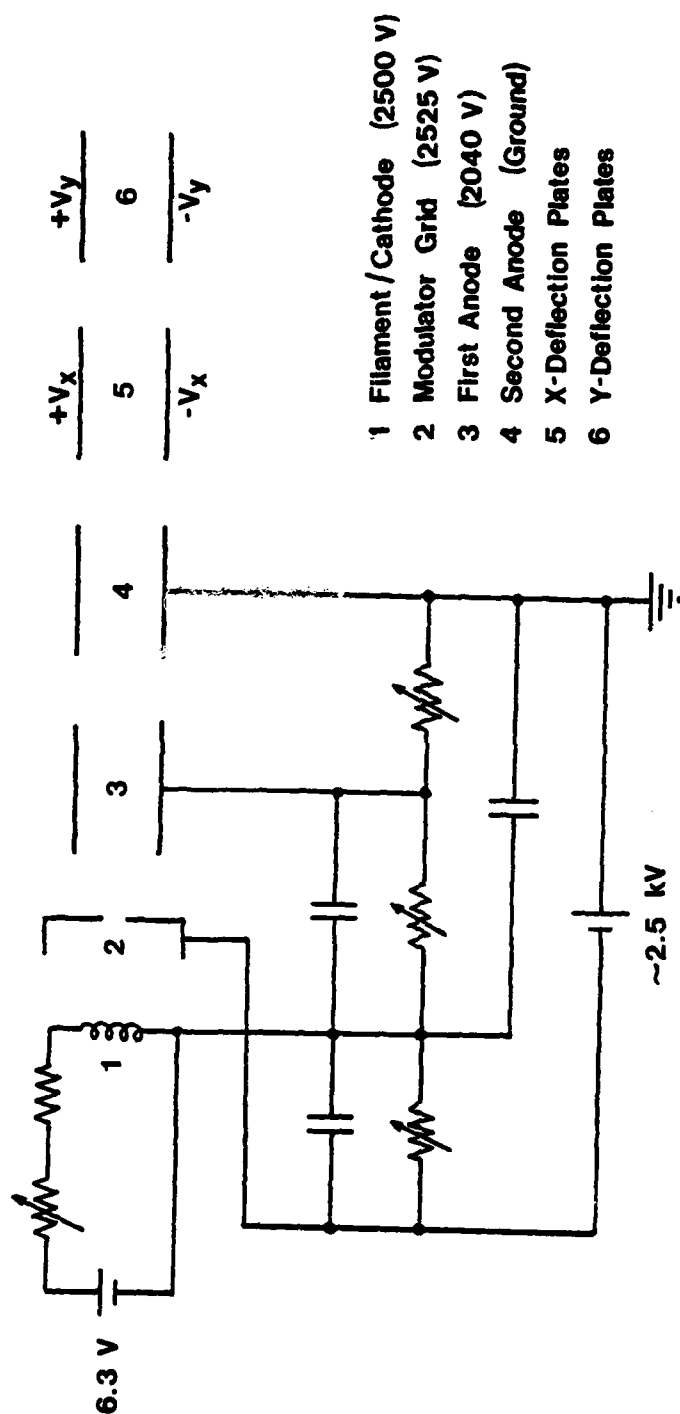
Figure 3.17. Electron gun electrical connections, and typical operating voltages.

pair. Deflection voltages are varied with ten-turn
helipots; it was found that the beam could be moved in the
sample plane by distances as small as 5 micrometers.

A phosphor viewing screen was fabricated by painting
an aqueous phosphor solution on the closed flat end of a
one-inch glass tube and subsequently baking until dry.
The screen mounts interchangeably with the sample holder,
and is used to visually position the beam, adjust the
focus, and determine the qualitative effects of varying
the grid voltages, etc.

A number of steps were taken to minimize defocusing
effects, thereby improving the beam. Magnetic fields are
the primary source of unwanted beam disturbance. DC
magnetic fields, such as those which arise due to the
permanent magnet in the ion pump, do not cause defocusing
but will prevent the electrons from traveling in a
straight line, and might therefore pose a problem. AC
magnetic fields, such as those produced by 60 cycle
current passing through a wire, will defocus the beam.

Magnetic shielding was installed around all portions
of the electron beam path. At least two concentric layers
of Conetic magnetic shielding fabric were wrapped around
all parts of the vacuum chamber. Stitch-welded mu-metal
cylinders encase the gun itself, thus necessitating the
addition of a blower to provide adequate cooling.
Although vacuum components are composed of type 304
stainless steel, they were degaussed. All unnecessary

magnetic materials (e.g., rotating machinery) were removed
from the vicinity of the experiment. The filament current
of 5 amperes was originally drawn from an AC supply, but
replacement by a DC source resulted in a considerably
samller spot size.

It was discovered that the emitter, modulator and
first anode voltages had significant 60 Hz ripple, on the
order of 100 mV peak to peak. Three filter capacitors,
visible in the circuit diagram of Figure 3.16, provide a
low impedance AC path to ground, effectively short
circuiting this ripple. In addition, shielded cables were
used for all gun connections, and a shielded box was
constructed to house the electron gun terminal strip.

Techniques were developed to allow profiling the
beam, as well as accurate calibration of the x and y
deflection settings. These consist of measuring collected
beam current as a function of position in the sample plane
with various slits and apertures, and are described in
Appendix D.

From measurements it was determined that our beam has
a Gaussian cross-section, with physical size denoted by
the half-width σ. Although beam current is a function of
both filament voltage and modulator grid potential, a
total beam current of 10 μA with a half-width of .013
inches at the sample plane is obtained during typical
operation. It was found that as filament voltage is
increased from 2.0 to 2.5 volts, beam spot size remains

essentially constant, whereas beam current increases by a factor of four. Beam current density, and hence test device terminal current are greatest when the filament is operated at 2.5 volts.

3.7. Vacuum System

A vacuum system is required to achieve and maintain the low pressures necessary for acceptable propagation of the electron beam. Electrons collide with gas molecules present in the system; at a pressure of 10^{-6} Torr the mean free path for such collisions is on the order of 100 meters.

A diagram of the vacuum system of this experiment, originally assembled by T.J. Maloney, is presented in Figure 3.18. Pumping is performed by a GE model 22TP300 triode ion pump with a pumping speed of 500 liters per second. System roughing is accomplished with two molecular sieve sorption pumps. Neither the ion pump nor the sorption pumps use oil; as a result the system is free from contamination associated with such oils.

The pressure in the ion pump chamber is directly related to the ion pump current,[74] and during normal operation is roughly 2×10^{-8} Torr. The level of vacuum in the experiment chamber, measured with an ionization gauge, is worse by an order of magnitude due to the high impedance pumping path arising from small dimensions, 90 degree turns, etc.
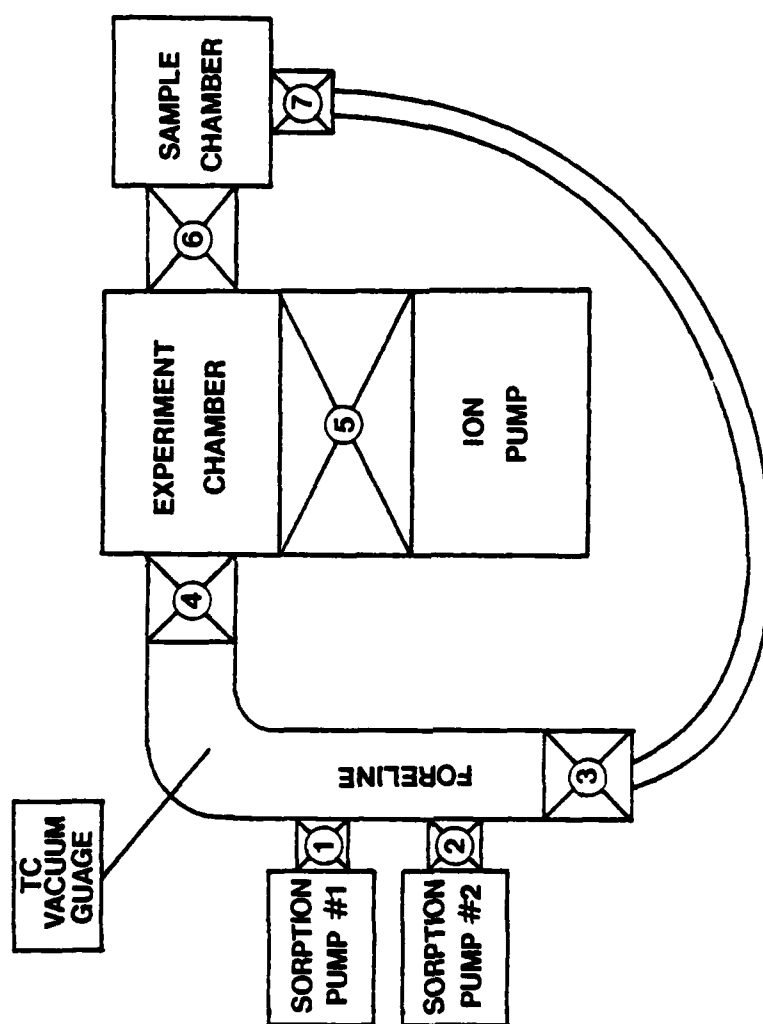
Figure 3.18. Vacuum system.

Hydrocarbon contamination was present in our experiment, as evidenced by the darkened area visible in the photograph of Figure 3.19. When the pressure is not low enough, a monolayer of hydrocarbons is deposited on the sample surface. If the aperture and sample are not precisely aligned, the hydrocarbons may cover the mesa edge, leading to eventual device failure. This contamination could be reduced by maintaining a pressure of less than 10^{-7} Torr.[75]

During normal operation, only valves 5 and 6 are open. To change samples, this procedure is followed:

1. Prechill sorption pump #2 with liquid nitrogen.

2. Close valve #6 (ball valve).

3. Change samples.

4. Open valve #2, valve #3 and valve #7.

5. When pressure on TC gauge is below 15 microns, close valve #7.

6. Close valve #3 and valve #2.

7. Slowly open valve #6.

8. Bakeout sorption pump if necessary.
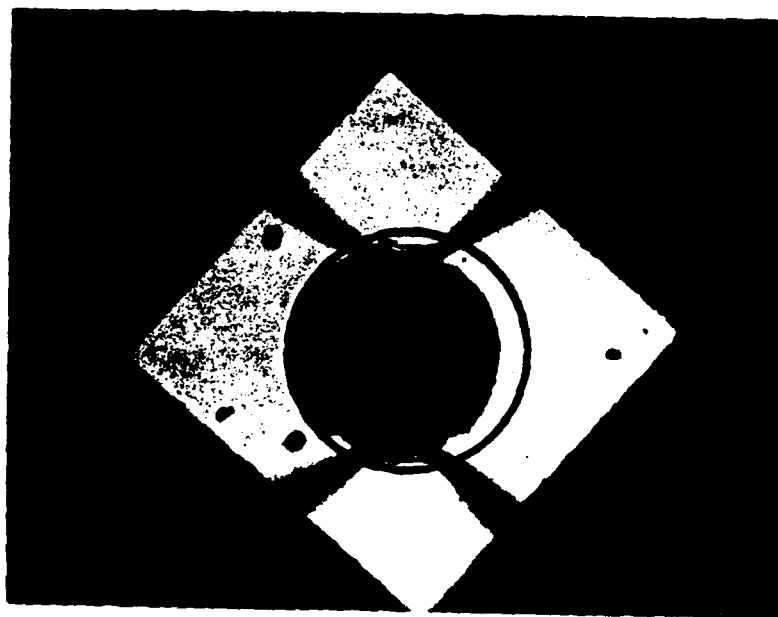
Figure 3.19.   Photograph of tested sample; note dark spot
due to hydrocarbon contamination.

CHAPTER 4

MEASUREMENTS

In this chapter the microwave time-of-flight measurement procedure is described. We explain the method of data analysis, which includes an empirical technique for removing diffusion and field taper effects.

Measured velocity-field curves are presented for electrons in Si and GaAs, and holes in Si. In all three cases the present results agree with previously published data at low fields, and are the first direct measurements in the very high field region. In addition, analysis of diffusion effects in GaAs samples has led to estimates of electron diffusivity at fields of 64 and 170 kV/cm.

4.1. Measurement Procedure

In the present work the amplitude and phase of 5.3 and 10.6 GHz components of the sample terminal current are measured as sample bias is varied continuously from zero to reverse breakdown. Experimental set-ups for 5.3 and 10.6 GHz operation are shown in Figures 4.1 and 4.2 respectively.

Analog outputs of the phase-gain indicator (part of the network analyzer system) drive the y channel of an x-y recorder while the x channel monitors bias voltage
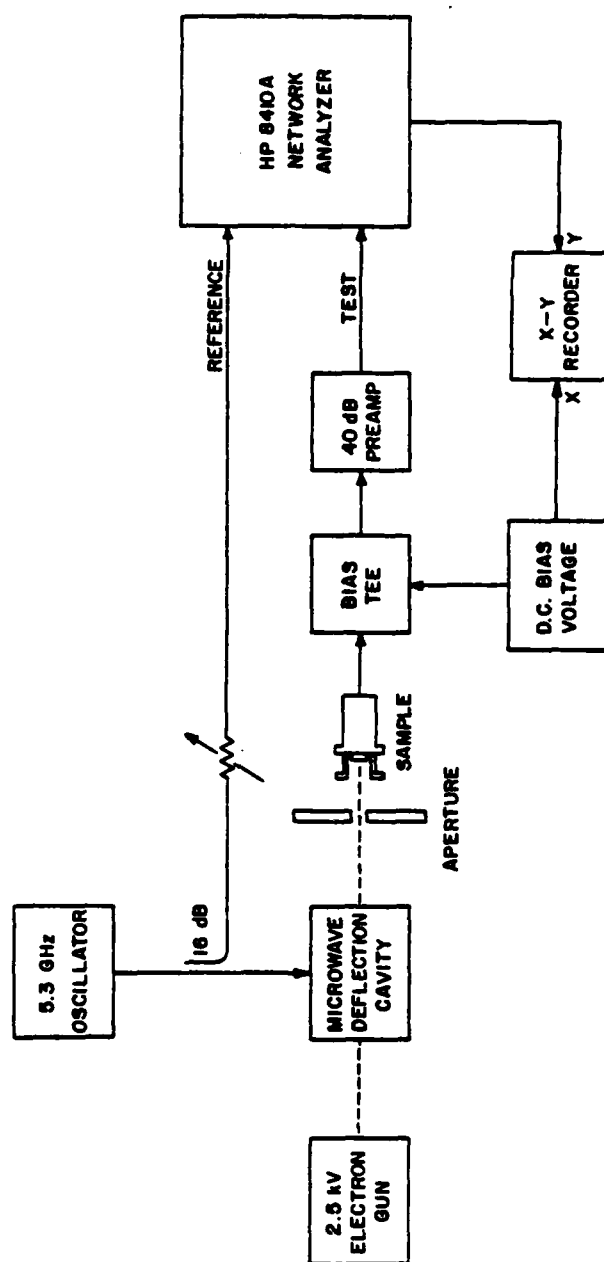
Figure 4.1. 5.3 GHz measurement scheme.
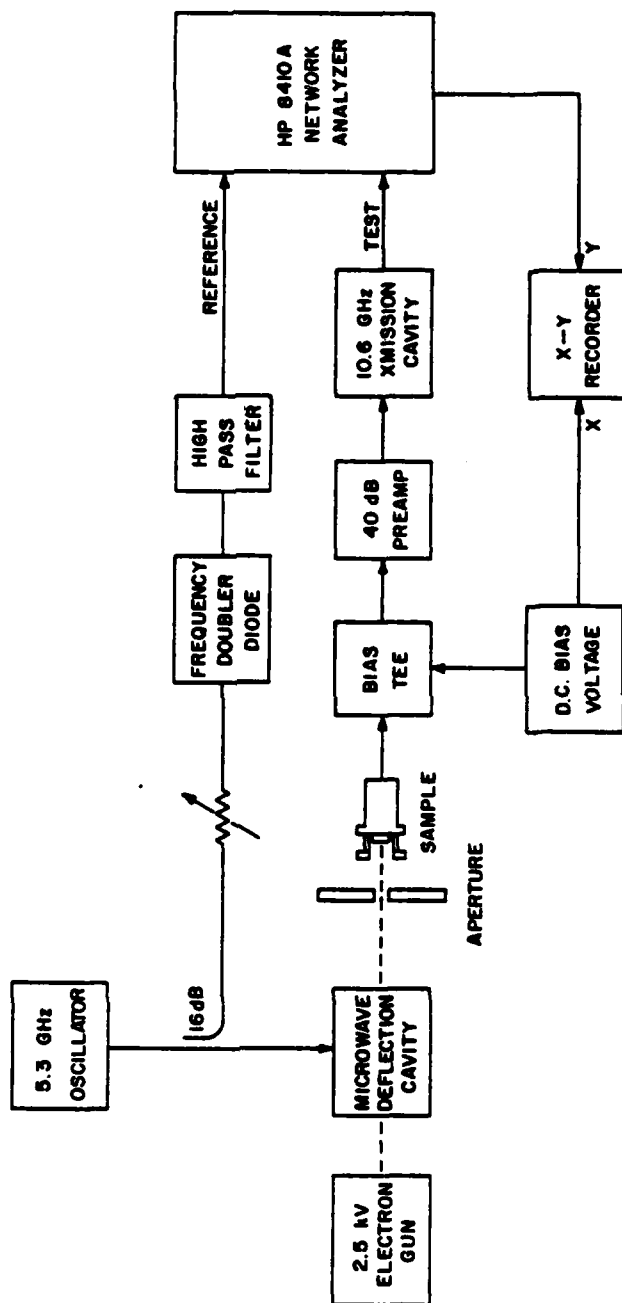
Figure 4.2. 10.6 GHz measurement scheme.

on the sample. An x-y recorder is ideal for these measurements since data can be taken very quickly, and spurious instabilities or discontinuities are easily visible. When discontinuities are observed, the measurement can be repeated until consistent results are obtained. Another advantage of the x-y recorder is that the position of amplitude minima and maxima can be determined more accurately than might be possible with discrete data points.

There are some obvious equipment differences between the 5.3 and 10.6 GHz measurement schemes. A 10.6 GHz reference signal is required for comparison with the 10.6 GHz test signal. A 1N23B mixer diode is used to double the frequency of a small portion of the power from the 5.3 GHz oscillator. The diode mount has a coaxial input and an X-band rectangular waveguide output. An X-band waveguide slide screw tuner allows the diode output to be matched, and is of sufficient length to severely attenuate any output power at the fundamental frequency, thereby acting as a high-pass filter. With 1.5 mW of 5.3 GHz input, a second harmonic output of 22μw is produced. This is within the reference channel power level specifications mentioned in Section 3.3.

Correct measurement of a single frequency component of terminal current requires that the signal entering either the reference or test channel of the harmonic

frequency converter must be spectrally pure (i.e. no harmonics). In the 5.3 GHz scheme it is the reference channel which is pure, since the oscillator (an HP 618C signal generator) has very low harmonic output. At 10.6 GHz, the frequency doubling diode has appreciable higher harmonics, and in this case a 10.6 GHz narrow band-pass cavity filter is used to insure that the test channel contains only a 10.6 GHz component. The filter which was constructed consists of a cylindrical cavity excited in the TM_{010} mode with input and output coupling and a mechanically tunable resonant frequency.

The general measurement procedure has three stages: first, the sample is inserted into the vacuum system and appropriate microwave equipment connected. With a small reverse sample bias, the modulated beam is turned on, and the desired frequency component is detected and its amplitude maximized by adjusting the beam position. Finally, bias voltage is varied and phase or amplitude is recorded. The specific measurement sequence appears in Appendix E.

4.2. Discussion of Data Analysis

Velocity-field results are derived from measured terminal current amplitude and phase. When necessary, corrections are applied for the two most important secondary effects, electric field non-uniformity and diffusion. Other second and third-order effects which

have been considered but can be shown to be negligible in the present circumstances will be discussed in the next chapter.

Since the forms of Equations (2.14) and (2.15) are fairly complex, v(x) can be determined from measured amplitude and phase only through an iterative procedure. A single computer program including both field taper and diffusion was found to require an excessive amount of computing time, making its use impractical in the present circumstances. It has been stated in Section 2.4, however, that when these effects are on the order of 10% or less, they can be treated separately using computer programs "E" and "EXPT", and the computed phase shifts can be added. In the next section the magnitude of secondary effects is evaluated by following this procedure.

Program "E", which quantifies the effect of E-field non-uniformity, uses the sample doping profile to calculate E(x) for a specified reverse bias voltage (see Figures 3.11 and 3.12), then combines this computed E(x) with an assumed v(E) and evaluates amplitude and phase of a given frequency component of the terminal current. Diffusion is not included in this program.

Program "EXPT" determines amplitude and phase when a specified diffusivity is introduced into a sample in which the carrier drift velocity is constant with position over the sample. Electric field variation is excluded from this program.

Once the magnitude of secondary effects has been evaluated, suitable corrections must be made. The phase is corrected using an empirical trial-and-error process to find out what an equivalent phase should be to achieve the measured $v(E)$, obtained from an equation that neglects both field taper and diffusion. Initially, a first-order $v(E)$ is obtained directly from the measured phase ϕ_m according to

$$v_1(E) = \frac{\omega \ell}{2\phi_m(E)}, \qquad (4.1)$$

An expression which ignores both field taper and diffusion. Assuming the $v_1(E)$ dependence of (4.1), programs "E" and "EXPT" compute the expected change in phase $\Delta\phi$, where

$$\Delta\phi(E) = \Delta\phi_E(E) + \Delta\phi_D(E) \qquad (4.2)$$

is the sum of the phase shifts due to the two secondary effects under consideration. Now,

$$\phi_1(E) = \phi_m(E) - \Delta\phi(E). \qquad (4.3)$$

In other words, for $v(E)$ to be correctly given by (4.1), the measured phase should be considered to be corrected by the amount $\Delta\phi$. If we now calculate

$$v_2(E) = \frac{\omega \ell}{2\phi_2(E)} \qquad (4.4)$$

where

$$\phi_2(E) = \phi_m(E) + \Delta\phi(E) \qquad (4.5)$$

i.e., ϕ_2 is displaced upward from ϕ_m by the same amount by which ϕ_1 is displaced downward, then our expected phase should be approximately equal to the measured phase ϕ_m. Thus, we have found a $v(E)$ which is consistent with our measured phase and includes field taper and diffusion. Of course, one may iterate once more, reevaluating $\Delta\phi$ assuming $v_2(E)$ and arriving at a $\phi_3(E)$ which in turn yields $v_3(E)$. However, it was found that additional iteration is usually not necessary if $\Delta\phi/\phi$ is small (i.e. less than 0.1).

Experimental data and derived velocity-field characteristics are presented in the next section. In all cases phase data is used to calculate some, if not all, of the velocity-field curve, and requires a reference point, as discussed in Chapter 2. Extrema in the amplitude data provide discrete, absolute points. If enough points are available, one can thus determine a $v(E)$ dependence; if only one or two such points are observed they can serve as references for the phase measurements.

ELECTRIC FIELD
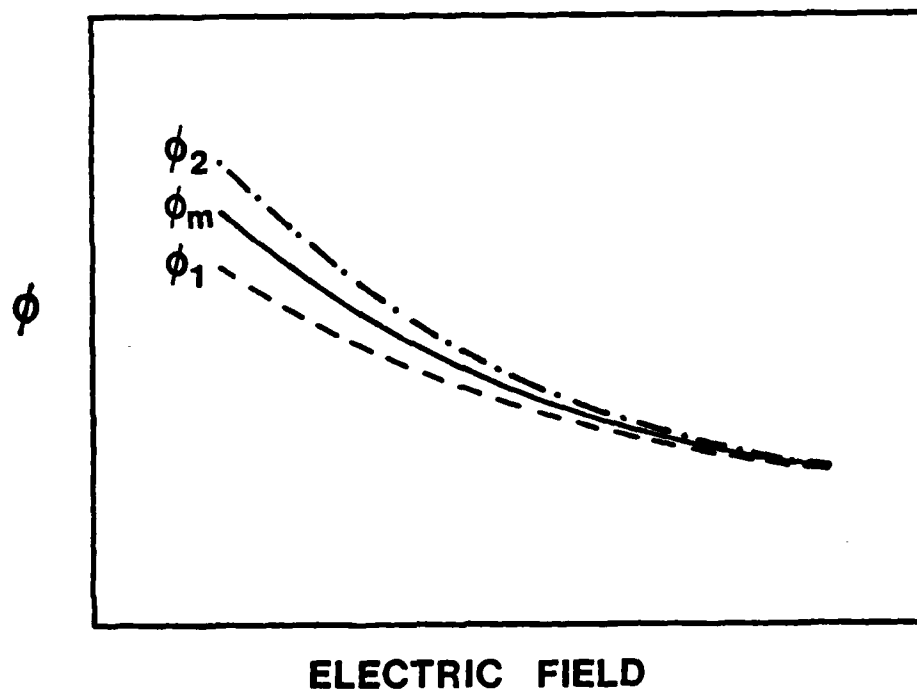
Figure 4.3. Illustration of iterative procedure used in
correcting phase for secondary effects.

A series of preliminary measurements was performed on n-Si samples in order to verify that the experimental system was functioning properly. Amplitude and phase were measured several times for a given sample, and found to be highly reproducible, with no discernible differences from one run to the next. At least three or four samples of a specific material and thickness were tested, always with good agreement of results. Consequently, results are normally reported for only one sample of each type and thickness.

4.3. Results and Discussion

4.3.1.   Electrons in Silicon

Results obtained with the two silicon samples whose doping profiles appear in Figure 3.5 are presented in this section. A thorough explanation of the data reduction procedure is given for the first sample discussed, #65.

Sample #65

The measured amplitude and phase at 5.3 and 10.6 GHz for 5.14 μm thick sample #65 are shown in Figures 4.4 - 4.7. Test channel signal level varied with bias voltage but was typically on the order of 1 microwatt. Data is analyzed in two steps:

1.   Obtain absolute point(s) from amplitude extrema.

2.   Match phase to absolute point, obtain v(E).
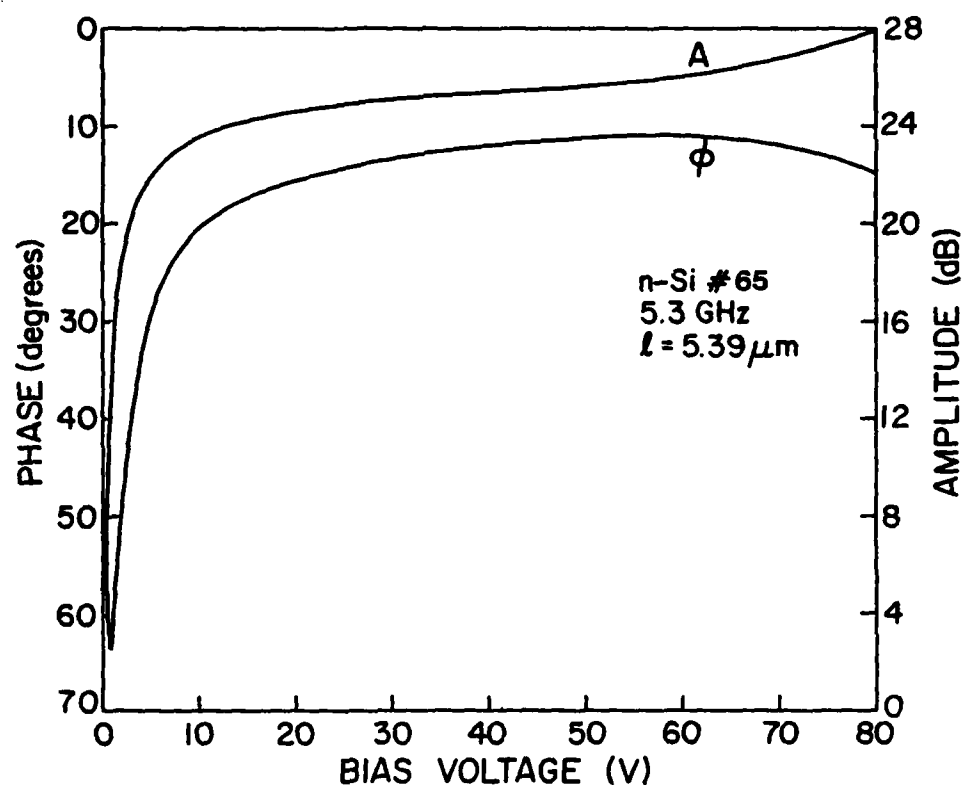
Figure 4.4. 5.3 GHz amplitude and phase data for n-Si
sample #65.
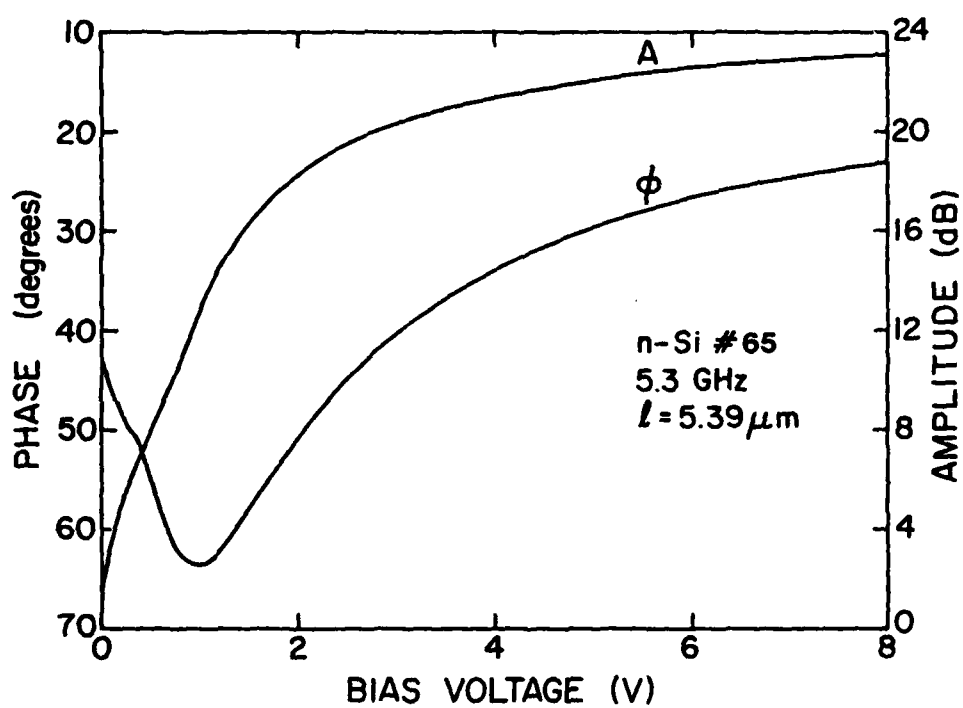
Figure 4.5.   5.3 GHz amplitude and phase data for n-Si
sample #65 at low reverse bias.
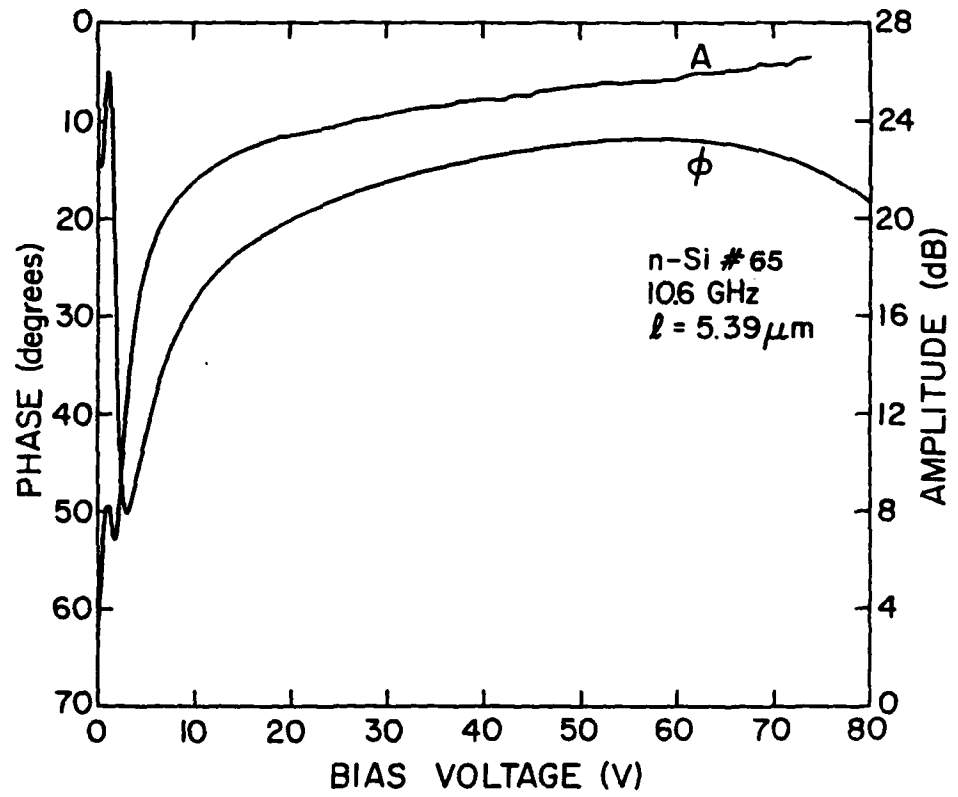
Figure 4.6.   10.6 GHz amplitude and phase data for n-Si
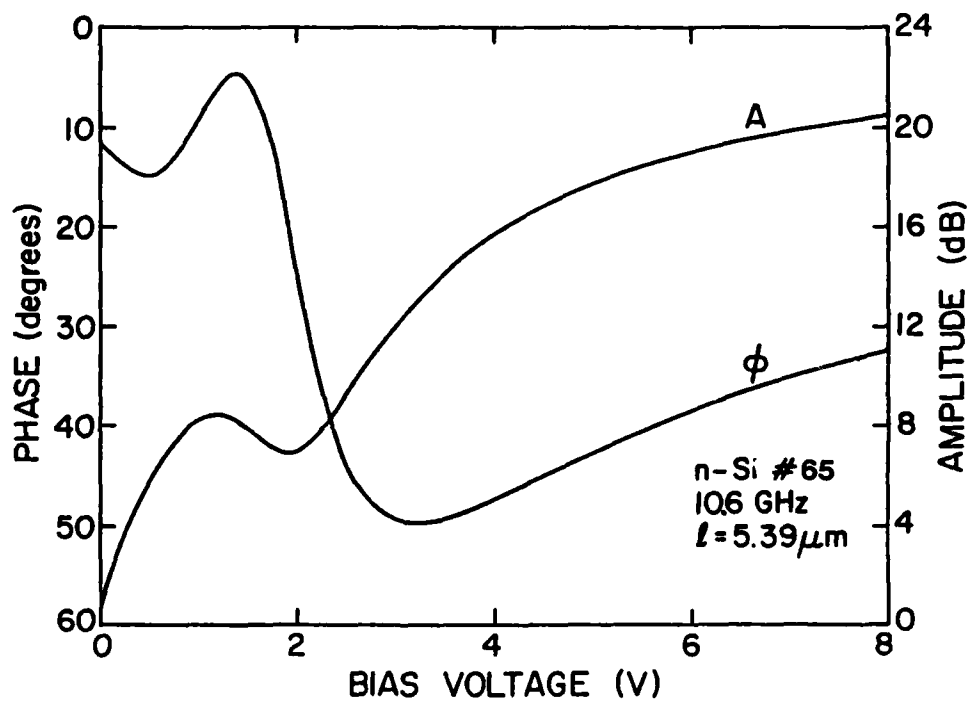
sample #65.

Figure 4.7. 10.6 GHz amplitude and phase data for n-Si
sample #65 at low reverse bias.

Two extrema are observed in the 10.6 GHz amplitude shown in Figure 4.7: a relative maximum occurs at 1.2 volts and a relative minimum occurs at 1.9 volts. Recall from Chapter 2 that the location of extrema can be determined from the phase as well, since the phase changes direction in the vicinity of minima. An extremum occurs at approximately the midpoint of a monotonic portion of the phase curve (see Figure 2.3, for example). The voltages at which the two extrema occur as determined from the phase are 0.95 and 2.1 volts.

The small but nonetheless important discrepancies between observed locations of the amplitude extrema might be due to thermal noise which increases with increasing electric field, and in general has a more pronounced effect on amplitude than phase. The open-circuit mean-square voltage of thermal or Nyquist noise is given by[47]

$$\langle V_n^2 \rangle = 4kTBR \tag{4.6}$$

where k is the Boltzmann constant, T the electron temperature, B the bandwidth and R the real part of the device terminal impedance. As electric field increases, carrier temperature, and hence noise, will increase. This is also evidenced in Figure 4.6: at a bias voltage of 55 volts, where the phase is constant, the amplitude should also be constant, but is in fact increasing with bias.

The locations of amplitude extrema are therefore obtained from the phase data. Electron velocity at the minimum and maximum is given by

$$V = \frac{f\ell}{n} \qquad (4.7)$$

where $n = 1.0$ and 1.430 respectively, and the average electric field by

$$\langle E \rangle = \frac{V_{bias} + V_{bi}}{\ell} \qquad (4.8)$$

The two points thus obtained are plotted in Figure 4.8.

It was shown in Chapter 2 that diffusion does not shift the velocity at which amplitude extrema occur, whereas electric field taper does. It is therefore necessary to correct the two points only for field taper. A correction procedure similar to that described in the last section is employed.

First, a $v(E)$ is assumed which passes through the experimentally observed points. Program "E" is run for a number of bias voltages, and the computed amplitude is used to pinpoint the position of expected extrema to a desired level of accuracy. A second $v(E)$ is assumed which is shifted upward from the first $v(E)$ by the same amount by which the calculated extrema were shiftward downward. When "E" is run again, calculated extrema agree exactly with observed extrema.
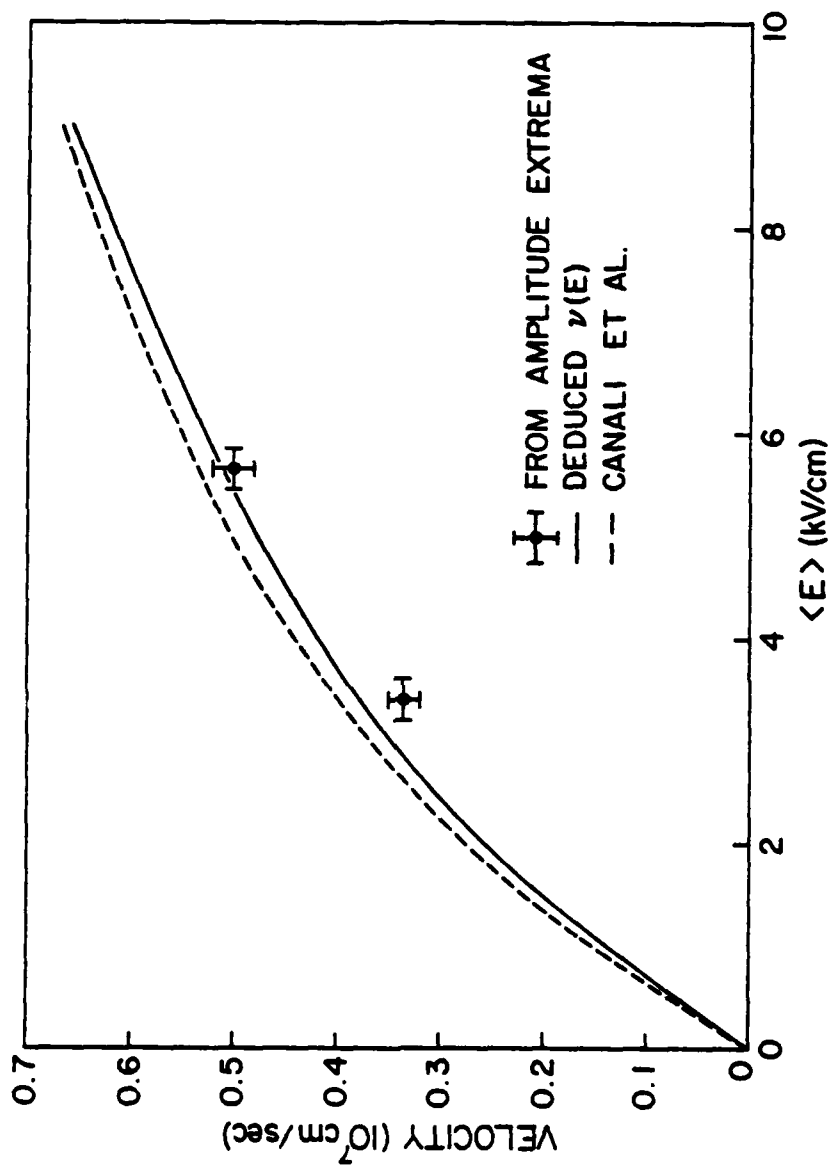
Figure 4.8. v(E) points derived from amplitude extrema, and deduced v(E) curve corrected for field taper.

The v(E) curve deduced in this manner, plotted in Figure 4.8, is most accurate in the vicinity of the measured points, i.e. the observed extrema. A velocity of 0.50×10^7 cm/sec at a field of 5.45 kV/cm is used as an absolute reference point to which the phase can be matched.

The 10.6 GHz phase is not well defined at an amplitude minimum (i.e. the reference point chosen) so the 5.3 GHz phase must be used. At the field of the reference point, 5.35 kV/cm, both diffusion and field non-uniformity may be important. In order to quantify these secondary effects, a reasonable v(E) dependence must be assumed.

A first-order v(E) is obtained by neglecting secondary effects again using the constant velocity expression (2.17), and matching to the predetermined reference point. The data reduction appears in Table 4.1. Although measured phase is a continuous function of bias voltage, calculations are necessarily performed at a series of discrete points. Average electric field is computed using (4.8). The reference value of velocity is used to calculate the phase ϕ_1 at 5.46 kV/cm. The measured phase ϕ_m is then shifted by 50.1 degrees, i.e.

$$\phi_1(E) = \phi_m(E) + 50.1^\circ \qquad (4.9)$$

Finally, electron velocity is determined according to

Table 4.1

Data Reduction Procedure Used to Determine First-order $v(E)$

from 5.3 GHz Phase

$V_{bias}(V)$	$\ell(\mu m)$	$<E>(kV/cm)$	ϕ_m	ϕ_1	$v(10^7 cm/sec)$
2.0	4.73	5.46	40.0°	90.1°*	.501
3.0	4.82	7.43	30.0	80.1	.574
4.0	4.86	9.42	23.3	73.4	.632
5.0	4.89	11.4	19.3	69.4	.672
7.5	4.95	16.3	13.7	63.8	.740
10.0	4.98	21.2	10.5	60.6	.784
15.0	5.02	31.0	7.3	57.4	.834
20.0	5.06	40.7	5.7	55.8	.865
25.0	5.07	50.5	4.3	54.4	.889
30.0	5.08	60.2	3.5	53.6	.904
35.0	5.09	69.9	2.6	52.7	.921
40.0	5.10	79.6	2.0	52.1	.934
45.0	5.11	89.2	1.5	51.6	.945
50.0	5.12	98.8	1.2	51.3	.952
55.0	5.13	108	1.0	51.1	.958
60.0	5.14	118	1.0	51.1	.959
65.0	5.14	128	1.2	51.3	.955
70.0	5.14	137	1.8	51.9	.944
75.0	5.14	147	3.0	53.1	.923
80.0	5.14	157	4.9	55.0	.891

*Matched to reference point

$$\phi_1 = \frac{\Omega\ell}{2v} = \frac{2\pi(5.3\times10^9 Hz)(4.73\times10^{-4}cm)}{(2(.501\times10^7 cm/sec)} = 90.1°$$

$$v(E) = \frac{\omega \ell (E)}{2\phi_1(E)} \cdot \qquad (4.10)$$

The phase shifts produced by field taper and diffusion can now be computed for the assumed first-order $v(E)$. In the diffusion analysis, the $D(E)$ dependence measured by Canali[77] over the field range 0 to 50 kV/cm was utilized, and the diffusivity was assumed to be 10 cm^2/sec for fields greater than 50 kV/cm.

The calculated phase shifts are listed in Table 4.2. It can be seen that the effect of electric field taper on phase is less than 5% at 5.45 kV/cm and decreases rapidly with increasing field. The magnitude of this effect was expected to be small, given the nearly ideal electric field profiles of sample #65 which are shown in Figure 3.11. The effect of diffusion is 3% at 5.45 kV/cm, and also decreases with field, albeit more gradually, due to decreasing diffusivity and increasing velocity (see discussion of Section 2.4).

$\Delta\phi$ is added to ϕ_1, yielding ϕ_2. However, ϕ_2 must now be shifted so that the calculated $v(E)$ curve will pass through the reference point. Thus

$$\phi_3(E) = \phi_2(E) - 6.7^\circ \qquad (4.11)$$

and velocity is calculated from $\phi_3(E)$.

Table 4.2

v(E) derived from 5.3 GHz phase corrected for E-field
taper and diffusion

$\langle E \rangle$ (kV/cm)	ϕ_1	$\Delta\phi_E$	$\Delta\phi_D$	ϕ_2	ϕ_3	$v(10^7$ cm/sec)
5.46	90.1°	4.0°	2.7°	96.8°	90.1°*	.501
7.43	80.1	2.7	1.7	84.5	77.8	.591
9.42	73.4	1.3	1.0	75.7	69.0	.672
11.4	69.4	0.8	0.9	71.1	64.4	.724
16.3	63.8	0.3	0.6	64.7	58.0	.814
21.2	60.6	0	0.5	61.1	54.4	.873
31.0	57.4	0	0.5	57.9	51.2	.935
40.7	55.8	0	0.4	56.2	49.5	.975
50.5	54.4	0	0.4	54.8	48.1	1.01
60.2	53.6	0	0.4	54.0	47.3	1.03
69.9	52.7	0	0.4	53.1	46.4	1.05
79.6	52.1	0	0.4	52.5	45.8	1.06
89.2	51.6	0	0.3	51.9	45.2	1.08
98.8	51.3	0	0.3	51.6	44.9	1.09
108	51.1	0	0.3	51.4	44.7	1.10
118	51.1	0	0.3	51.4	44.7	1.10
128	51.3	0	0.3	51.6	44.9	1.09
137	51.9	0	0.3	52.2	45.5	1.08
147	53.1	0	0.3	53.4	46.7	1.05
157	55.0	0	0.3	55.3	48.6	1.01

* Matched to reference point.

The resulting velocity-field curve is shown in Figure 4.9. Although measurements were extended up to 157 kV/cm, impact ionization is considered to be appreciable for bias voltages in excess of 65 volts, as evidenced by the upturn in amplitude visible in Figure 4.4 at high reverse bias. As a result v(E) is reported only up to a field strength of 135 kV/cm.

It will now be shown that the 10.6 GHz phase is consistent with the 5.3 GHz phase when field taper and diffusion are taken into account. Recall that in the constant velocity, diffusion-free case, phase is proportional to frequency. The change in phase over a given field range at 10.6 GHz should thus be equal to twice the change in phase at 5.3 GHz over the same field range.

Figure 4.10 shows that agreement is very good. The largest difference occurs at low fields, and is due to the fact that field taper and diffusion are more important at 10.6 GHz than at 5.3 GHz. The fractional changes in phase $\Delta\phi/\phi$ calculated at both frequencies are listed in Table 4.3. Note that at 9.4 kV/cm the total relative change in phase at 5.3 GHz due to both effects is 3.2%, while at 10.6 GHz the relative change in phase is 10.7%, the difference being 7.5%. It can be seen in Figure 4.10 that at 9.4 kV/cm the difference between the two curves is 9.9° or 7.2%. Agreement is also excellent at other fields, supporting the validity of the model used to correct for
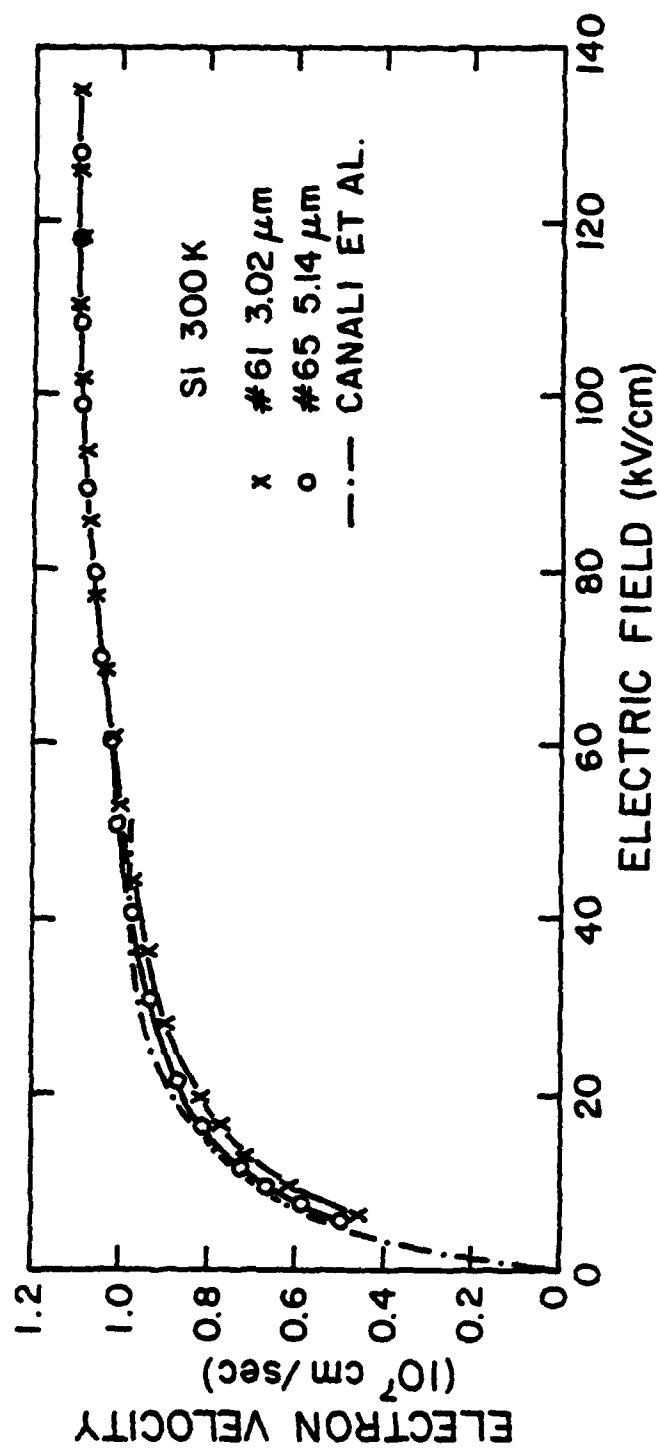
Figure 4.9. Electron drift velocity as a function of electric field for (111) silicon at 300 K.
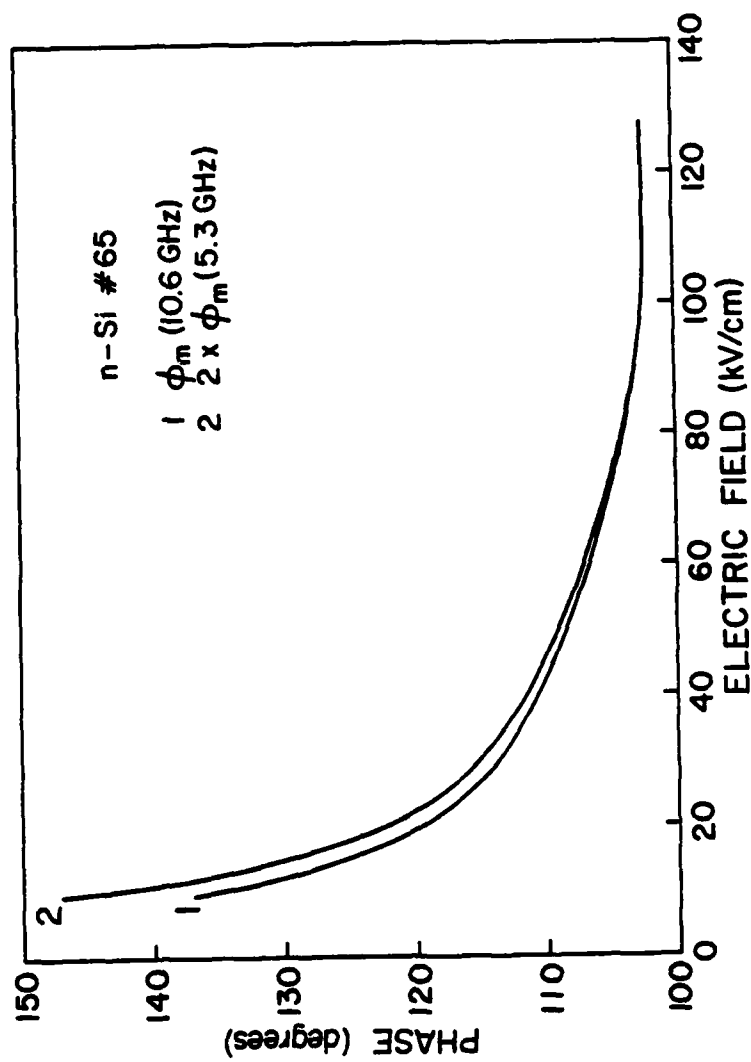
Figure 4.10. Comparison of measured phase at 10.6 GHz with twice the measured

phase at 5.3 GHz. Curves are matched at 120 kV/cm.

Table 4.3

Fractional changes in phase due to E-field

taper and diffusion at 5.3 and 10.6 GHz for sample #65

$<E>$ (kV/cm)	E-field taper $\dfrac{\|\Delta\phi_E\|}{\phi}$		Diffusion $\dfrac{\|\Delta\phi_D\|}{\phi}$	
	5.3 GHz	10.6 GHz	5.3 GHz	10.6 GHz
5.5	.044	—	.030	—
7.4	.034	.158	.021	.106
9.4	.018	.059	.014	.048
11.4	.012	.033	.013	.039
16.3	.005	.016	.009	.023
50.5	0	0	.009	.014

secondary effects.

Sample #61

Sample #61 has an epitaxial layer which is 3.02 μm thick, significantly thinner than that of sample #65. As a consequence, no amplitude extrema are observed. In this case the 5.3 GHz phase is matched to the saturated velocity measured in sample #65 at 120 kV/cm.

Bott and Hilsum[78] have shown theoretically that at high fields electron temperature can be sufficiently high that optical-phonon emission will dominate all other scattering processes. Saturated drift velocity is therefore expected to be independent of low-field mobility. Several workers[19,34,79] have discussed this phenomenon in the light of experimental results.

5.3 GHz phase data were corrected for field taper and diffusion; the magnitude of these effects is nearly the same as it was in sample #65. The resulting v(E) curve is plotted in Figure 4.9.

Discussion

The following conclusions are drawn from the results given in Figure 4.9:

1. A saturated velocity of $1.10 \pm .08 \times 10^7$ cm/sec was measured. This value agrees with the high-field results of Stubbs[80] (1.08×10^7 cm/sec at 120 kV/cm) and Duh and Moll[18] (1.05×10^7 cm/sec at 300 kV/cm). The

estimated error is attributed to errors in the initial amplitude minimum determination, uncertainty in the phase measurement, and errors in the secondary effect calculations. However, the <u>shape</u> of the v(E) curve is believed to have an accuracy better than 1-2%.

2. Agreement of the velocity-field curve derived from sample #65 with the time-of-flight results of Canali et al[40] is excellent at low fields, although they show a measured velocity saturation at a field of only 40 kV/cm. It is believed that avalanche effects may have caused a premature downturn of their v(E) curve in the same manner as seen in our results at fields greater than 135 kV/cm.

3. The thinner sample, #61, is observed to have a lower low-field mobility than sample #65: mobilities are estimated to be 1100 vs. 1350 cm^2/v-sec. This is probably due to imperfect crystal quality near the epi-layer/substrate interface which has a more pronounced effect on velocity in the thinner sample.[81] Note that the two measured v(E) curves converge at approximately 60 kV/cm, the same field at which electron velocity in silicon-on-sapphire films was found to be independent of low-field mobility.[19] From this one might infer that optical phonon scattering is the predominant scattering mechanism in silicon at fields greater than 60 kV/cm.

4.3.2. Electrons in GaAs

In this section results obtained with the n-GaAs

samples of Figure 3.6 are given and discussed. Data is again reduced in two steps:

1. Use a sample of appropriate length to allow observation of an amplitude null.

2. Match the 5.3 GHz phase data of several samples to the reference point found in step 1. (5.3 GHz phase data is preferred over 10.6 GHz phase data since it was seen in the last section that both field taper and diffusion have a smaller effect at 5.3 GHz).

Amplitude Null

A minimum observed in the 10.6 GHz amplitude of sample #35 at a bias voltage of 47 volts leads to a calculated velocity

$$v = f\ell = (10.6 \times 10^9 \text{Hz})(7.45 \times 10^{-4}\text{cm}) = 0.79 \times 10^7 \text{cm/sec} \qquad (4.12)$$

at an electric field of 64 kV/cm. As seen in Figure 4.13, the minimum is relatively sharp, and its position is thus insensitive to field dependent thermal noise. As before, a correction must be applied to account for field non-uniformity.

The effect of field taper on the position of the amplitude minimum was calculated using a v(E) consisting of the low field (0-14 kV/cm) results of Ruch and Kino[34] combined with the high field (14-100 kV/cm) results of Houston and Evans. The calculated minimum led to a

velocity 1% lower than the assumed curve; the velocity
indicated by our amplitude null was therefore increased by
1%, to 0.80 x 10^7 cm/sec.

5.3 GHz Phase

The velocity-field curve for electrons in GaAs will
be determined here from measured 5.3 GHz phase for four
samples of different lengths using 0.80 x 10^7 cm/sec at 64
kV/cm as a reference point. It was seen experimentally
that as sample length decreases, both the variation in
phase over a given range in field and the test channel
signal level decreased. The observed phase behavior was
expected from (2.17); the signal level dependence is
attributed to circuit effects, as explained in the next
chapter.

First, field taper effects are considered. As a
first approximation to v(E) we combine the low field
results of Ruch and Kino with the v(E) given by

$$v(E) = \frac{\omega \ell (E)}{2\phi (E)} \tag{4.13}$$

after ϕ(E) has been matched to the reference point.
Results of calculations performed with computer program
"E" are plotted in Figure 4.11 and are summarized as
follows:

1. As was seen to be the case in the n-Si samples,
there exists some value of electric field (in this case 10
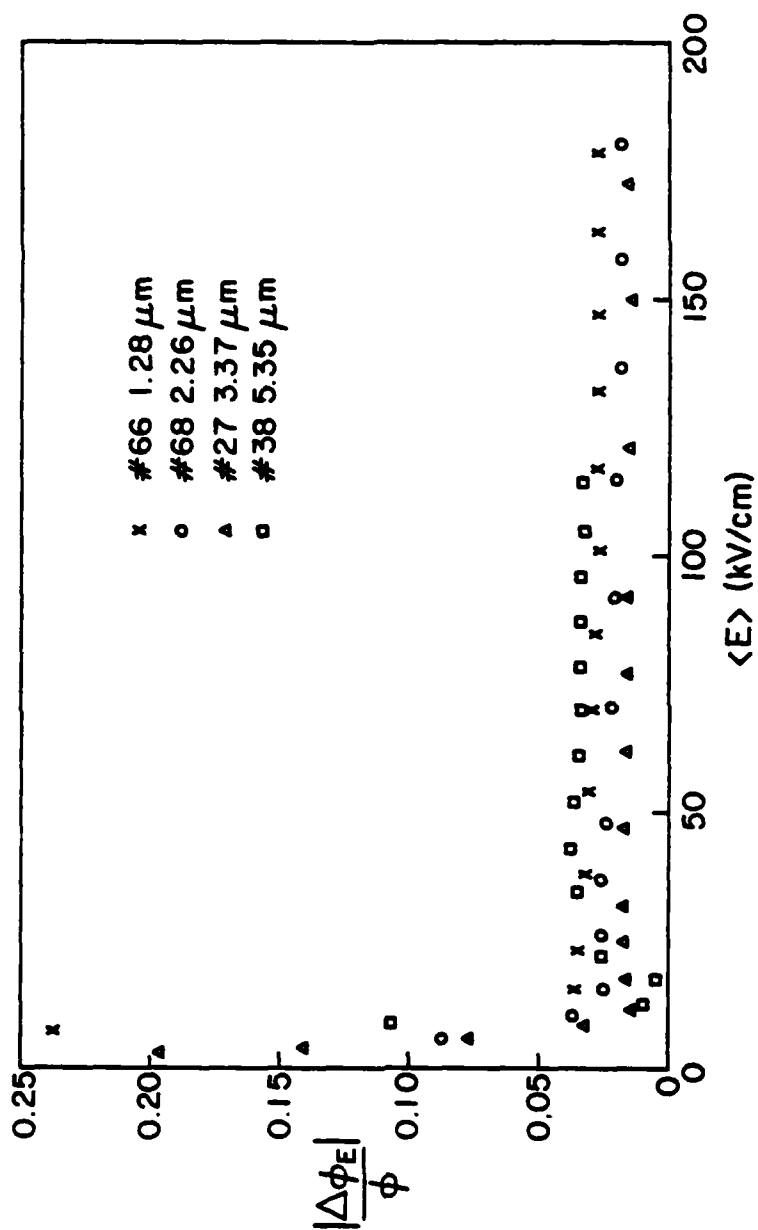
Figure 4.11. Computed relative phase shifts due to field taper vs. average electric field for four n-GaAs samples.

kV/cm) below which the effect of field taper increases dramatically.

2. The computed phase shift $\Delta\phi_E$ is opposite in sign to that calculated for the n-type silicon samples over the entire field range studied. This is due to the fact that in GaAs at fields greater than 3 to 4 kV/cm, the first derivative of $v(E)$ is negative, and hence $v(x)$ is an increasing function of x over most of the sample, not as is the case in n-Si or the example of Section 2.3.

3. The computed relative change in phase remains essentially constant over a wide range of electric field (not as in silicon), and varies from about 1.6% for sample #27 to 3.5% for sample #38. The effect is more pronounced in samples which have less ideal doping profiles, i.e. relatively high epi-layer doping and a gradual transition from layer to substrate.

The velocity-field curve can be corrected for field taper following the same general procedure outlined for silicon. However, since the magnitude of the effect is independent of field, and variation of phase with field is small (on the order of 25%), the entire phase curve is shifted by approximately the same amount; hence the net effect of field taper is reduced when the phase is matched to the reference point. Consequently, the effect of field taper on the velocity-field curves which are calculated from (4.13) and plotted in Figure 4.12 is less than 1% for all points shown.
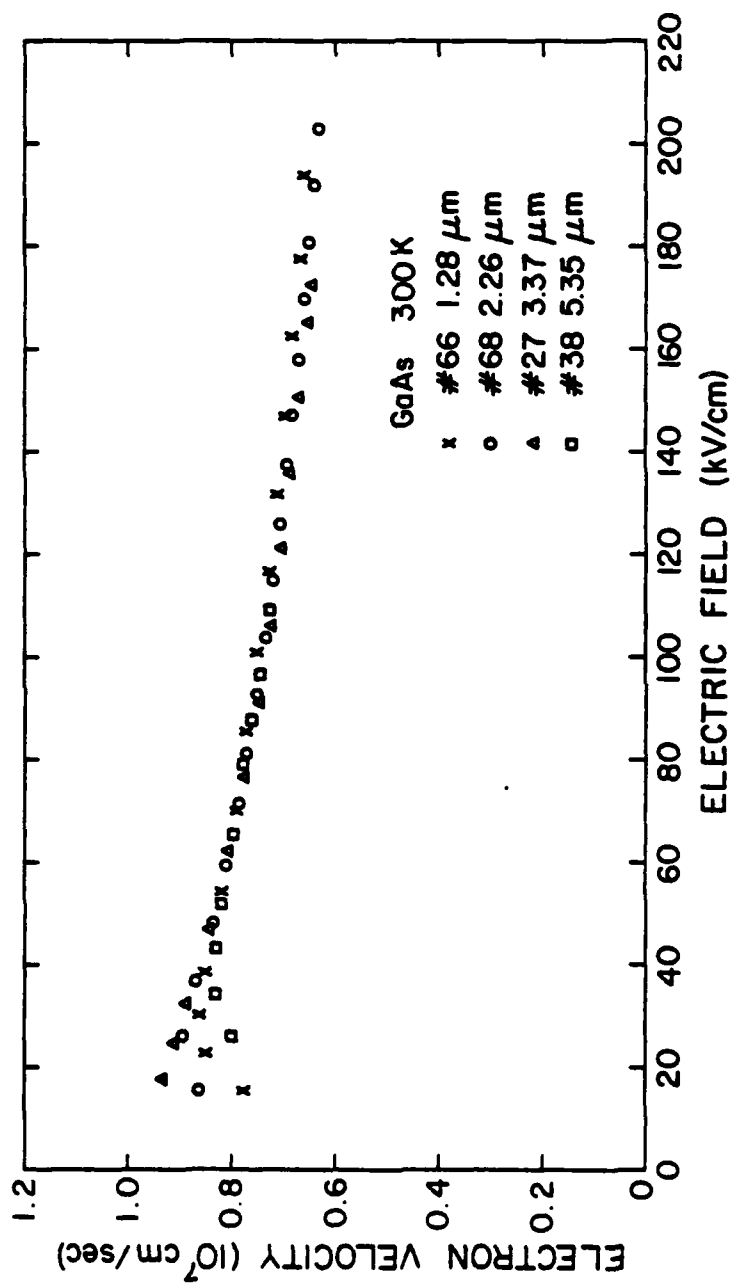
Figure 4.12. Electron velocity vs. electric field for (100) GaAs at 300 K, calculated from measured 5.3 GHz phase.

The experimental data for layers of different thickness are seen to be in good agreement over most of the measured field range, with two notable exceptions:

1. At fields below 40 kV/cm the curves for different samples diverge. This is believed to be due to the existence of an undepleted region of the epitaxial layer adjacent to the substrate, and is discussed further in the next chapter. Since this effect is related to electric field non-uniformity, it is not surprising that the sample sequence in which the v(E) curves "roll off" is identical to that seen in Figure 4.10 for increasing relative effect of field taper.

2. At high fields a small yet discernible trend is observed: as sample thickness decreases, the corresponding v(E) curves are displaced upward. This is attributed to diffusion, which has a more pronounced effect in thinner samples, and is analyzed later in this section.

The effect of field taper is least important in sample #27, and is in fact sufficiently small that we may make some qualitative observations at fields as low as 3 kV/cm. The results of Ruch and Kino are shown in Figure 4.13. If their velocity-field dependence is used as a first guess, calculations including field taper indicate that we should measure for sample #27 an apparent velocity given by (4.13) which is about 15% higher than our actual measured apparent velocity. It should be obvious that a

v(E) curve slightly lower than Ruch and Kino's, having a peak velocity of 1.9 to 2.0 x 10^7 cm/sec, would be consistent with our measurements. Such a curve has in fact been obtained by Braslau and Hauge.[82]

Since diffusivity is known to be large in GaAs at low fields, it may have a significant effect on the results shown in Figure 4.13. A number of low-field D(E) characteristics, obtained both experimentally[34] and theoretically[83-86] using Monte Carlo techniques, have been reported. However agreement is poor, the diffusivity at threshold field, in particular, varying from about 250 cm^2/sec[83,84] to 950 cm^2/sec.[34,35] Calculations for sample #27 using the curve of Fawcett and Rees[83] lead to apparent velocities which are 7 to 15% higher than the assumed values. Much higher values of diffusivity, such as those of references 5 and 14, would have a significantly greater effect, and are felt to be inconsistent with our measurements.

Recall that the high-field results of Figure 4.12 have not yet been corrected for diffusion. Unfortunately, experimental information on diffusivity at high fields is scarce. An indirect measurement performed by Castelain et al[87] is claimed to show that the diffusivity at fields of 50 and 150 kV/cm does not exceed 20 and 50 cm^2/sec, respectively. We present here a technique for determining diffusivity with the microwave time-of-flight experiment.
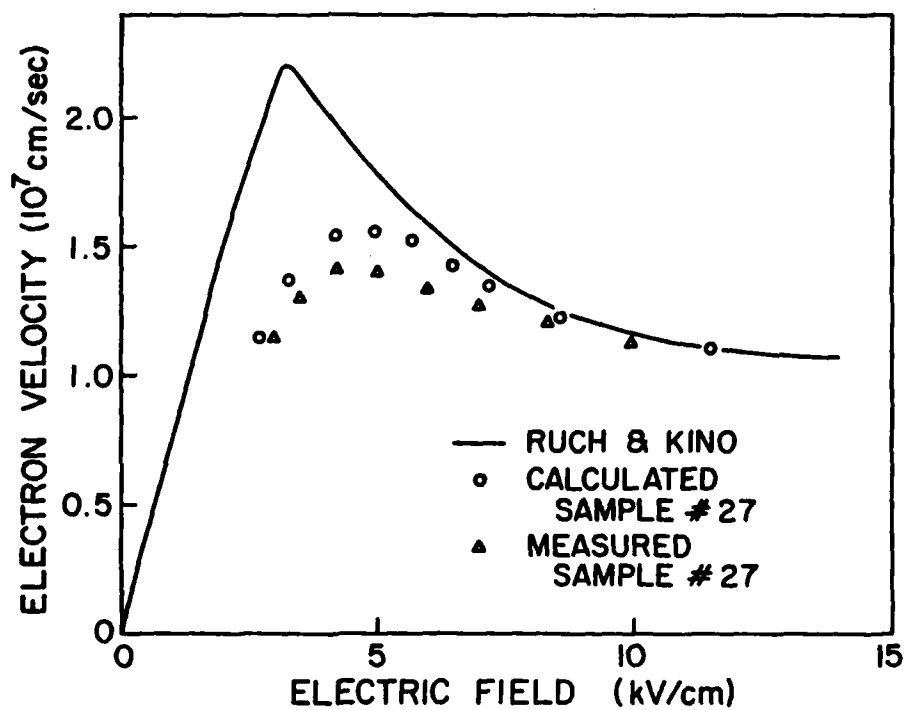
Figure 4.13. Comparison of measured low-field apparent velocity for sample #27 with calculations including field taper which assume v(E) of Ruch and Kino[34].

It was shown in Chapter 2 that diffusion causes the
amplitude at a minimum to be non-zero. The degree to
which this minimum is smoothed out is dependent on the
diffusivity, as is illustrated in Figure 4.14. When D = 0
the amplitude computed for sample #35 with program "EXPT"
possesses a minimum which is sharply defined. As D
increases, the minimum becomes less pronounced. For a
diffusivity of 20 cm^2/sec, agreement with experimental
data is excellent. Of course, this interpretation is
valid only if the effect of field taper is insignificant,
since field taper also causes amplitude nulls to be
smoothed out.

It is seen in Figure 4.15, however, that field taper
is primarily responsible for the observed amplitude versus
bias voltage dependence. Diffusion, which would further
alter the observed amplitude curve, is thus considered to
be minimal; hence the diffusivity at 64 kV/cm is believed
to be less than 10 cm^2/sec.

It was stated in Chapter 2 that when the phase is
less than π, as in all of our 5.3 GHz measurements
reported thus far, diffusion causes the apparent velocity
to be greater than the actual value. The effect was
predicted to be greatest in thinner samples. It is seen
in figure 4.12 that at 170 kV/cm the 2.26 μm and 1.28 μm
sample length curves are 1.5% and 4.0% higher,
respectively, than the 3.37 μm curve. First, it may be
concluded from the shape of the curves that the
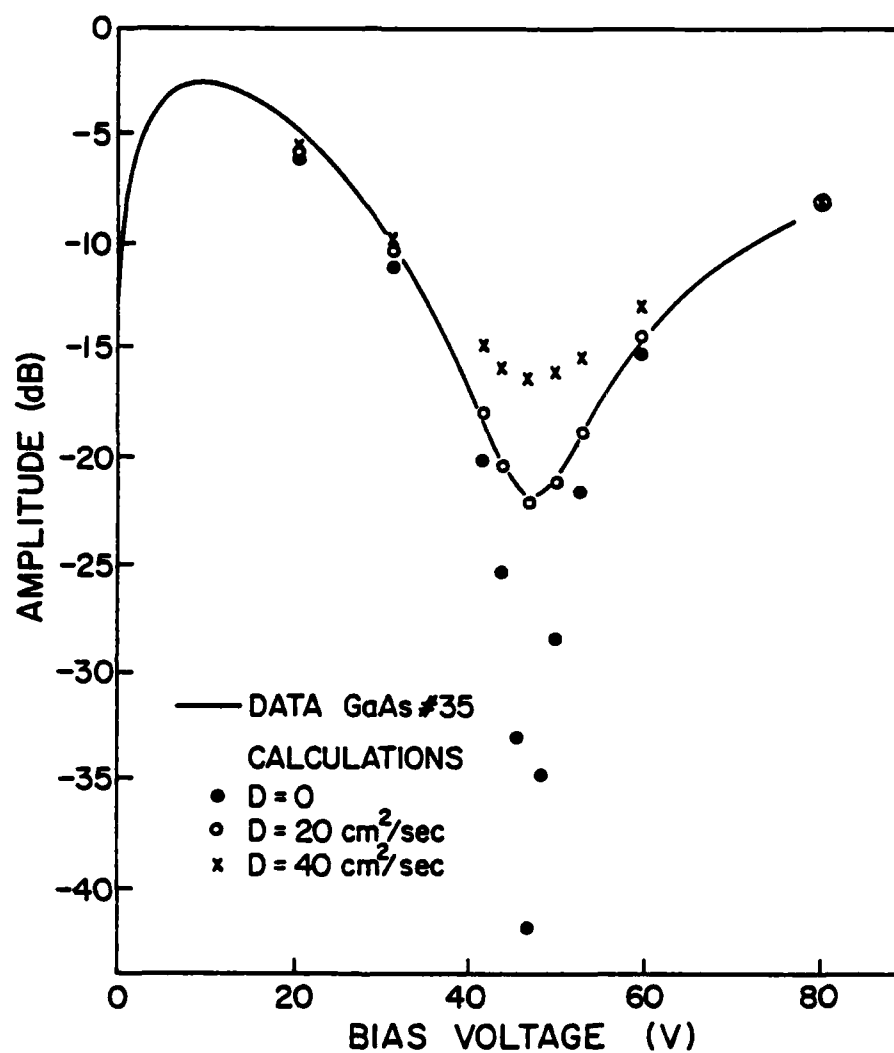
Figure 4.14. Comparison of observed amplitude null with

calculations performed for various diffusivities.
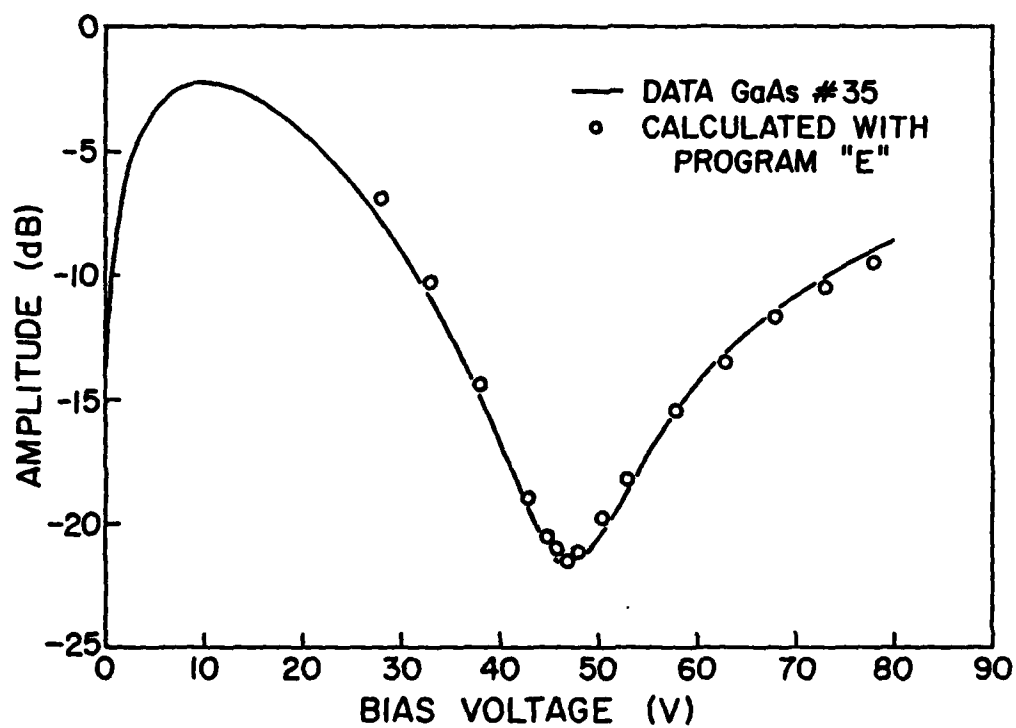
Figure 4.15.   Comparison of observed amplitude null with
calculations including field taper.

diffusivity is larger at 170 kV/cm than at 64 kV/cm.
Next, given the diffusivity at 64 kV/cm, we can determine
a 170 kV/cm diffusivity which is consistent with the
observed v(E) spreading. Results are as follows: when
D(64 kV/cm) is 0, D(170 kV/cm) = 25 cm^2/sec. For D(64
kV/cm) equal to 10 cm^2/sec, a D(170 kV/cm) of 33 cm^2/sec
is obtained. Thus,

$$D(64 \text{ kV/cm}) = 5 \pm 5 \text{ cm}^2/\text{sec}$$

$$D(170 \text{ kV/cm}) = 29 \pm 4 \text{ cm}^2/\text{sec}$$

The effect of diffusion is subsequently removed from
the results of Figure 4.12. The resulting velocity-field
characteristic, which lies slightly below the 3.37 μm
curve, is shown in Figure 4.16.

Discussion

Measured electron velocity in GaAs is seen to
decrease steadily from 0.86 x 10^7 cm/sec at 40 kV/cm to
0.60 x 10^7 cm/sec at 205 kV/cm. Our measurements agree
with the room temperature results of Houston and Evans[44]
to within 3% to their measurement limit of 100 kV/cm,
although our curve descends more rapidly, as is also the
case with the results of Bastida et al.[20]

Given the temperature dependence observed by Houston
and Evans, our velocity-field relation agrees with the
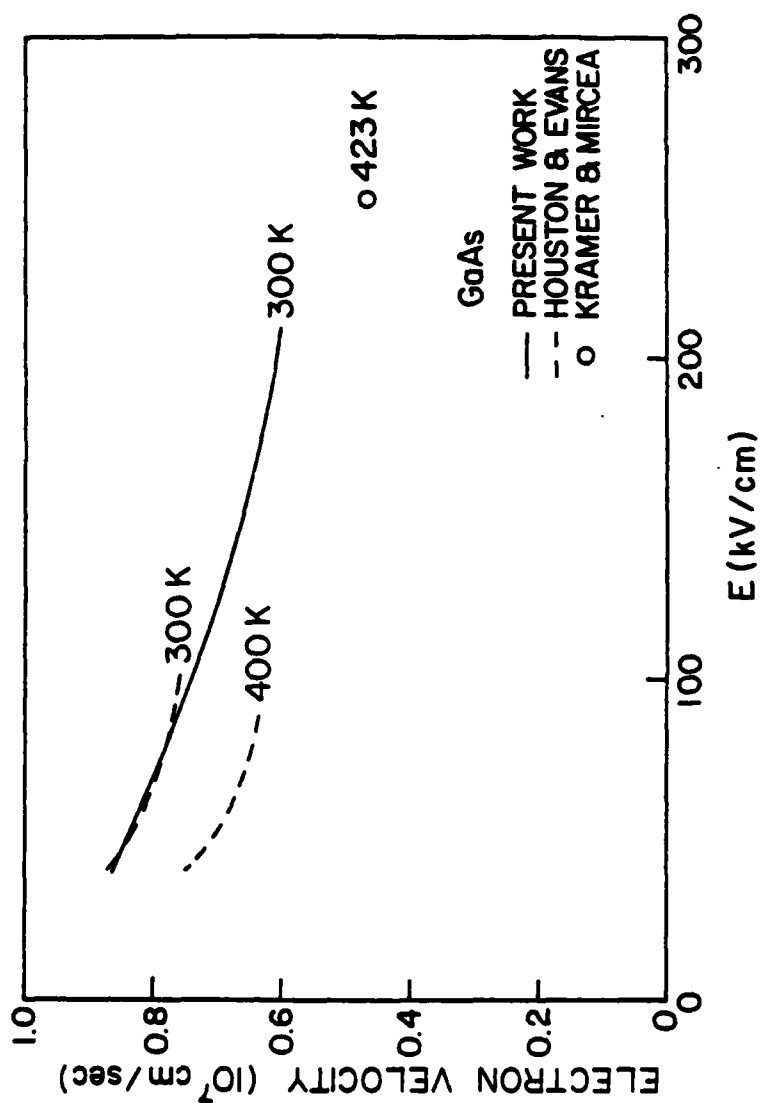
Figure 4.16. Electron velocity versus electric field for (100) GaAs.

point obtained by Kramer and Mircea.[31] Our results are also consistent with the room temperature saturation velocity of 0.57 ± 0.03 x 10^{7} cm/sec determined by Okamoto and Ikeda.[30] It should be noted that both of these high field results were derived indirectly from measurements of the space-charge resistance of IMPATT diodes.

Although several workers[20,44,88,89] have reported velocity-field characteristics in the 20 to 100 kV/cm field range, the results given here are the first direct measurements of electron velocity at fields greater than 100 kV/cm.

4.3.3. Holes in Silicon

The drift velocity as a function of electric field measured for holes in silicon is presented here. A representative sample doping profile appears in Figure 3.7.

10.6 GHz data for sample #70 is presented in Figure 4.17. The amplitude possesses two minima and three maxima, from which a total of five absolute v(E) points are found via Equation (2.19). Points obtained in this manner for four samples at both 5.3 and 10.6 GHz are plotted in Figure 4.18. At fields below 30 kV/cm it was necessary to apply a small correction to account for field taper; the method by which this was done has been described in detail in Section 4.3.1.
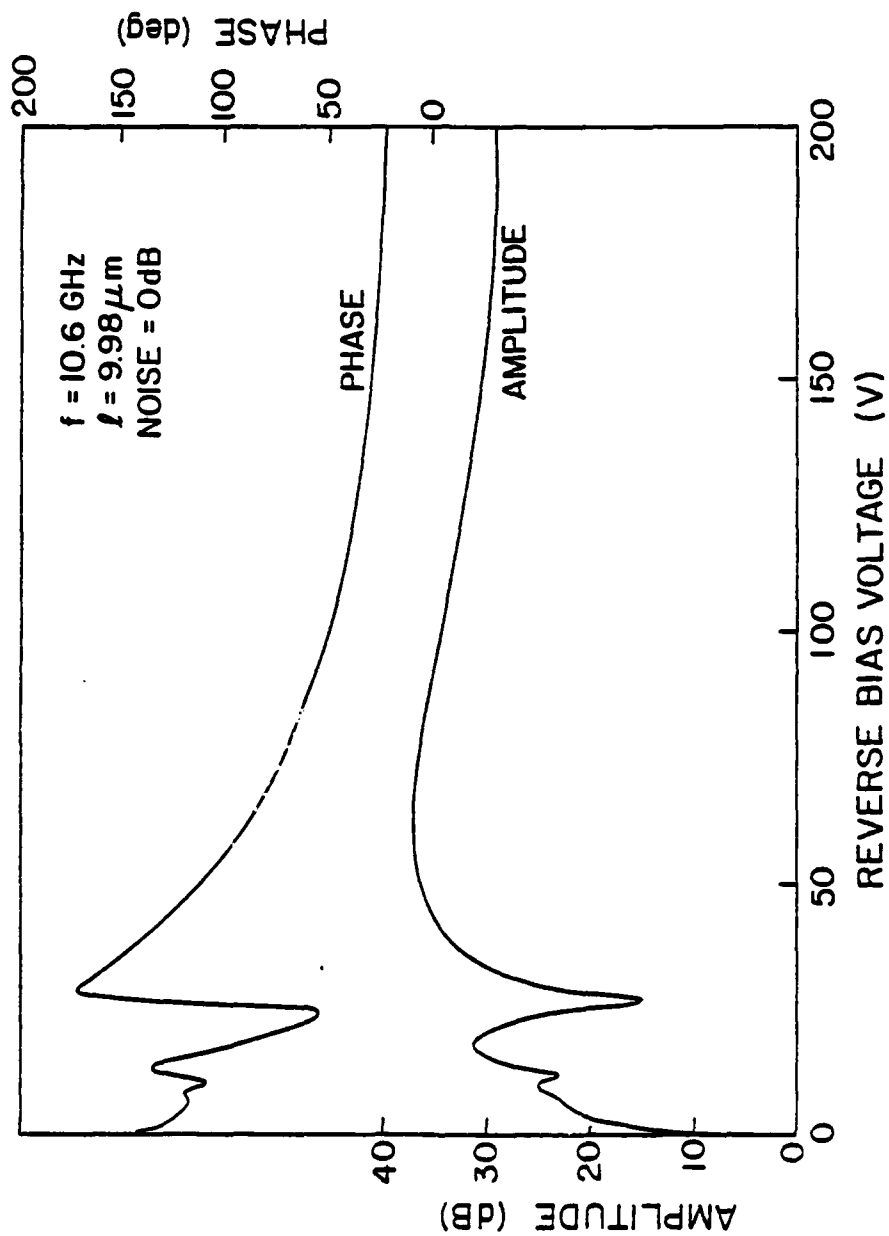
Figure 4.17.   10.6 GHz data of sample #70.
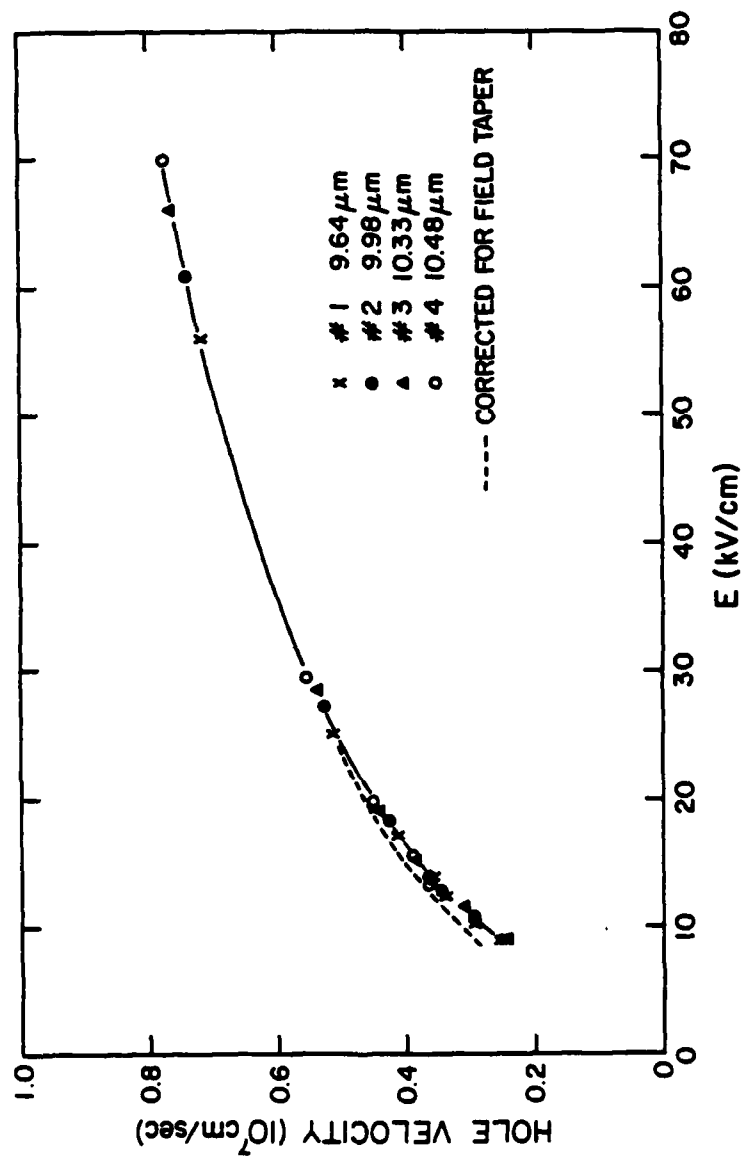
Figure 4.18. Velocity-field curve obtained from extrema in the amplitude data.

A continuous high-field portion of the v(E) curve, shown in Figure 4.19, was derived from phase measurements, with the absolute points in the vicinity of 60 kV/cm serving as a reference. The effect of diffusion on measured phase was calculated assuming the D(E) dependence reported by Nava et al,[43] extrapolating their value of 4 cm^2/sec at 50 kV/cm to higher fields, and was found to be negligible. Similarly, field taper had an insignificant effect on the phase results.

Upon combining amplitude and phase results, and including the field taper correction at low fields, the composite curve of Figure 4.20 is obtained. For fields below 50 kV/cm our results agree with those of Nava et al to within 3%. The observed saturation velocity is 0.96 ± .05 x 10^7cm/sec, with saturation occurring at 175 kV/cm. Previous measurements[11-13,40,43,90] of hole drift velocity in silicon were confined to substantially lower fields; hence this is the first reported observation of hole velocity saturation in silicon.[91]
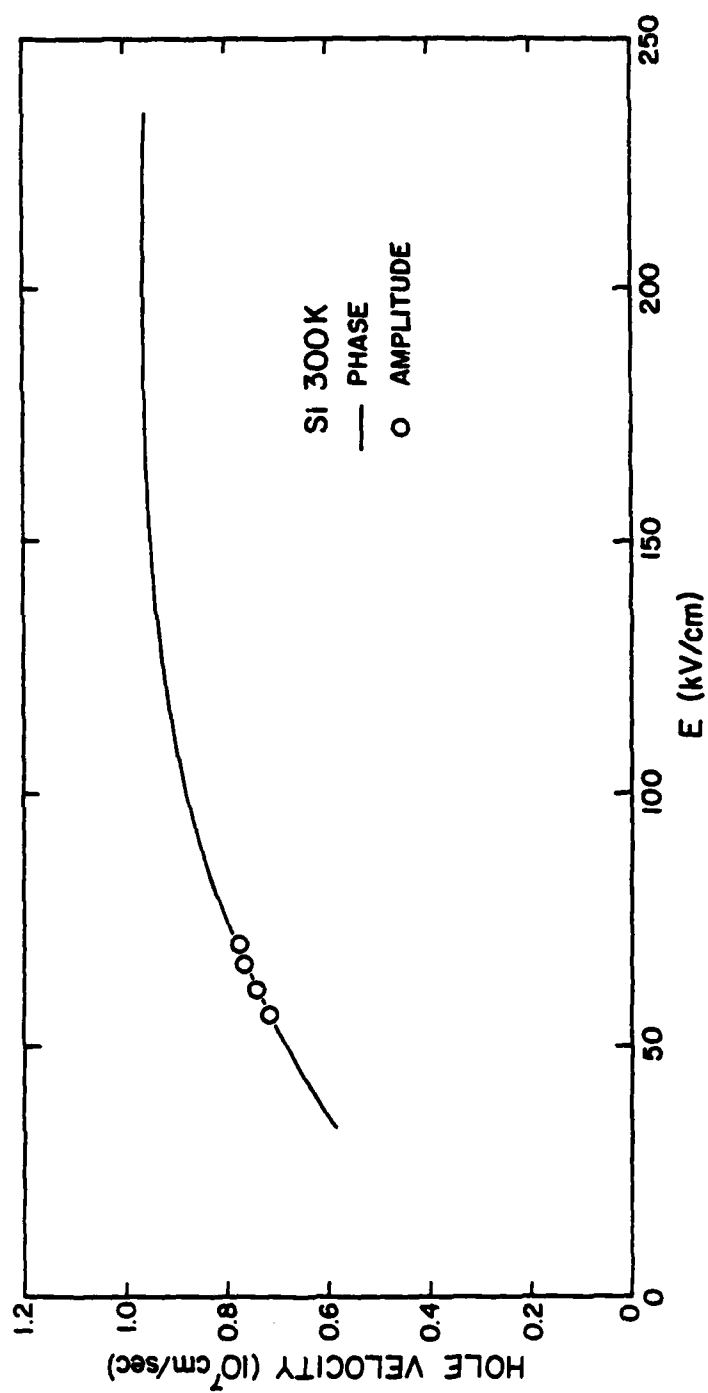
Figure 4.19. High-field velocity determined from phase measurement.
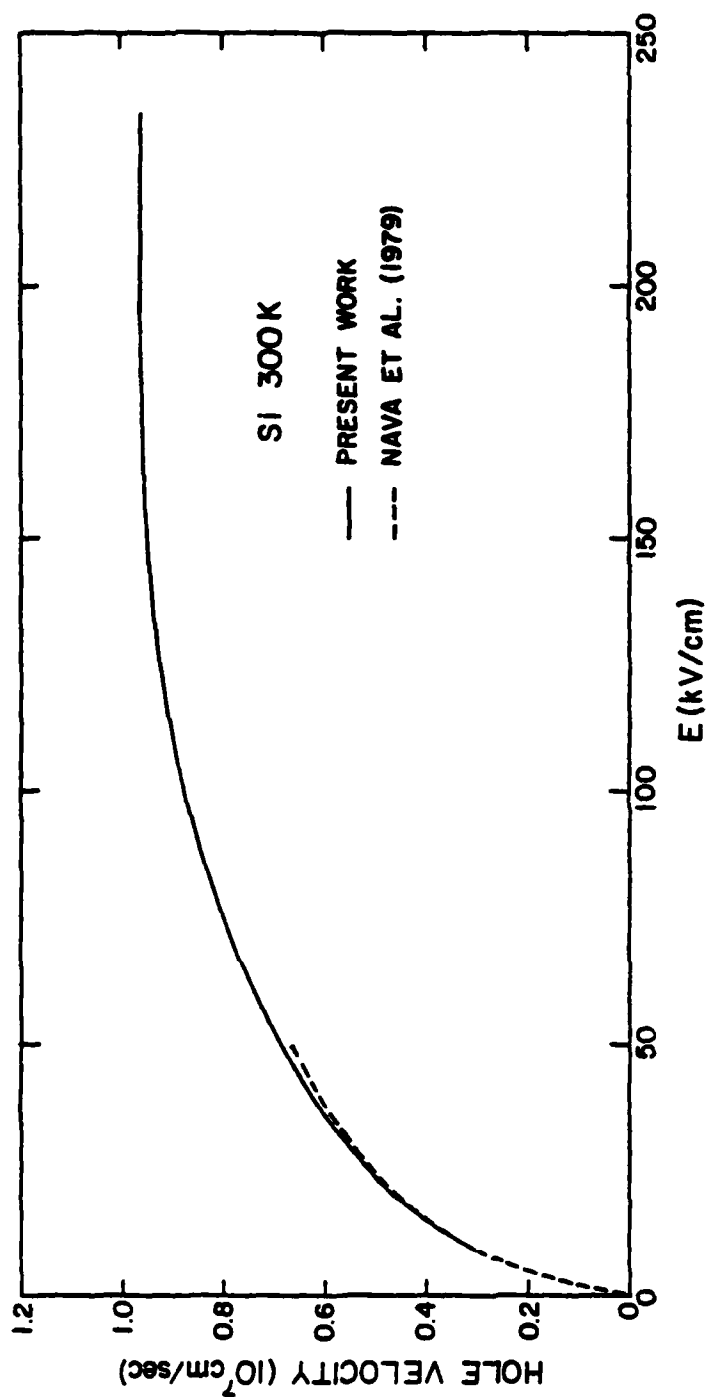
Figure 4.20. Hole drift velocity as a function of electric field for (111) silicon at 300 K.

CHAPTER 5

SOURCES OF ERROR

In this chapter real and potential sources of error
are examined. A conventional analysis of experimental
errors appears in Section 5.1. The remainder of the
chapter deals with several secondary effects which could
be important in this experiment, including practical
considerations such as circuit effects and stability,
and physical phenomena such as avalanche processes,
electron-hole pair creation, trapping, space charge and
thermal effects. In particular, several assumptions
upon which the theoretical work of Chapter 2 has been
based are justified here; whenever possible,
experimental evidence is presented.

5.1. Error Analysis

In this experiment sample length is derived from
100 MHz C-V measurements according to

$$\ell(V) = \frac{\varepsilon a}{C(V)} \tag{5.1}$$

in which the low frequency dielectric permittivity ε, as
distinguished from the high frequency or optical
dielectric constant, is well known for most
semiconductors. As stated in Appendix C, capacitance C
can be measured to within 1%.

The samples are circular, ranging in diameter from 361 to 380 μm due to variations in the mask sets and undercutting of mesas. The diode diameter d is measured to within 1% with a Unitron model MMU no. 34610 metallurgical microscope with calibrated 10X objective, and checked with another calibrated microscope. The physical size of the metal contact on the surface is therefore known quite accurately.

However, Equation (5.1) is accurate only if the diode diameter is much greater than the layer thickness ℓ. If this condition is not satisfied, edge effects (i.e. fringing fields at the periphery of the diode) could be important. In this case we must define an effective area a_{eff} larger than the physical area a such that

$$\ell(V) = \frac{\epsilon a_{eff}}{C(V)} \tag{5.2}$$

An exact three-dimensional calculation of the capacitance of a circular metal pattern separated from an infinite conducting plane by a dielectric of uniform thickness is needed, but such a calculation is too involved for the present work. Instead, we somewhat arbitrarily estimate that the effective sample radius increases by less than a third of the sample thickness; for our thickest sample, with $\ell = 10$ μm, the effective area differs from the physical area by less than 3%. Estimated error in diode area is thus the sum of the error in the determination of

the physical size (1%) and the error arising from the use of Equation (5.1) in cases where edge effects are not negligible (3%), and can be as high as 4%.

Maximum uncertainty in sample length is roughly equal to the sum of the maximum error in diode area (4%) and the uncertainty in the measured capacitance (1%) and is therefore 5%.

Carrier velocity is derived from amplitude extrema using the relation

$$v = \frac{f\ell}{n}. \tag{5.3}$$

According to the manufacturer's specifications, the HP 537A frequency meter can determine f with an accuracy of $\pm$ 0.2%. Since n is known precisely, error in velocities obtained from amplitude extrema is less than 5%, and is due almost exclusively to the uncertainty in sample length.

Velocity is related to phase by

$$v = \frac{\omega \ell}{2\phi(V)} \tag{5.4}$$

where

$$\phi(V) = \phi_{meas}(V) - \phi_o \tag{5.5}$$

$\phi_{meas}(V)$ can be determined to within half a degree. Since

ϕ is proportional to sample length, the relative uncertainty in phase will be smaller for thicker samples. Velocity derived from phase measurements will have an associated uncertainty which is the sum of two components: error in the reference point and errors in the quantities ω, ℓ, and ϕ.

5.2. Circuit Effects

In this section we present an equivalent circuit model for the microwave time-of-flight sample and external measurement circuit, and use it to examine some importnat effects. A general equivalent circuit[92,93] appears in Figure 5.1. Most of the elements shown are of a parasitic nature. A two-port network described by four H-parameters[94] is used to model all microwave components between the sample and an ideal network analyzer whose load impedance Z_L is equal to 50 ohms. The components, including the sample holder, bias tee, low noise amplifier and various adapters, are thus assumed to be linear for the small signal swings in this experiment.

As discussed in Appendix C, package capacitance C_p and fringing capacitance C_f are equal to 0.31 and 0.08 picofarads, respectively. Four bonding wires were attached to each sample in an effort to minimize bonding wire parasitics L_w and R_w. Since the addition of four more bonding wires did not affect measured phase, R_w and L_w can be safely neglected.

$$\tilde{H} = \begin{pmatrix} H_{11} & H_{12} \\ H_{21} & H_{22} \end{pmatrix}$$

PACKAGED DEVICE   **MEASUREMENT CIRCUIT**
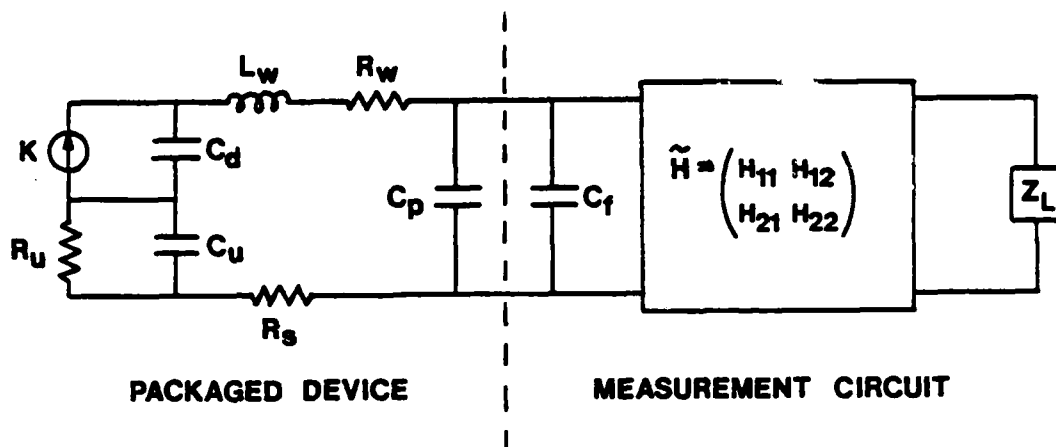
K = Terminal current

C_d = Depletion layer capacitance

L_w = Bonding wire inductance

R_w = Bonding wire resistance

R_u = Undepleted zone resistance

C_u = Undepleted zone capacitance

R_s = Substrate resistance

C_p = Package capacitance

C_f = Fringing capacitance

$\tilde{H}$ = H-parameters of 2-port network

Z_L = Load impedance

Figure 5.1.   General equivalent circuit for microwave
time-of-flight measurements.

Substrate resistance R_s is the sum of two components: the resistance of the ohmic contact covering the back surface of the chip and the bulk substrate resistance given by

$$R = \frac{\rho L}{A} \qquad (5.6)$$

where resistivity ρ is less than 0.01 ohm-cm, L is on the order of 400 μm, and A is approximately 4.0×10^{-7} m^2. R_s can be determined from measurement of the diode reflection coefficient at high frequencies.

For the sample thicknesses used (between 1 and 10 μm), depletion layer capacitance C_d varied from 1 to 10 pF. At the operating frequencies of this experiment, capacitive reactance ranged from 1.5 to 30 ohms, and thus dominated the circuit impedance.

If the sample reverse bias is not sufficiently large, the epitaxial layer will not be fully depleted. This is illustrated in Figure 3.11 at an average electric field of 30 kV/cm. The undepleted zone has a resistance given by

$$R_u = \frac{1}{a} \int_{\ell}^{\ell_o} \rho(x) \, dx \qquad (5.7)$$

where ℓ is the location of the depletion layer edge, ℓ_o is the epitaxial layer thickness, and a is the diode area. Undepleted zone capacitance is given by

$$C_u = \frac{\epsilon\ a}{(\ell_o - \ell)} \quad . \tag{5.8}$$

For the epitaxial layer resistivities and frequencies of this experiment, the undepleted zone resistance is approximately one-tenth the undepleted zone capacitive reactance, so the latter is neglected.

With the simplified circuit of Figure 5.2a, the voltage across the load, V_2, can be determined as a function of $\tilde{H}$, C_d, R and K. Note that the undepleted zone resistance has been lumped together with the substrate resistance, and that both C_p and C_f are now included in the two-port described by $\tilde{H}$.

By definition,[94]

$$V_1 = H_{11}I_1 + H_{12}V_2 \tag{5.9}$$

$$I_2 = H_{21}I_1 + H_{22}V_2 \tag{5.10}$$

From Figure 5.2a it is also obvious that

$$I_1 = K + j\omega\ C_d\ (V_1 - I_1 R) \tag{5.11}$$

$$I_2 = \frac{V_2}{Z_L} \tag{5.12}$$

The following expression for V_2 is obtained from Equations (5.9)-(5.12):
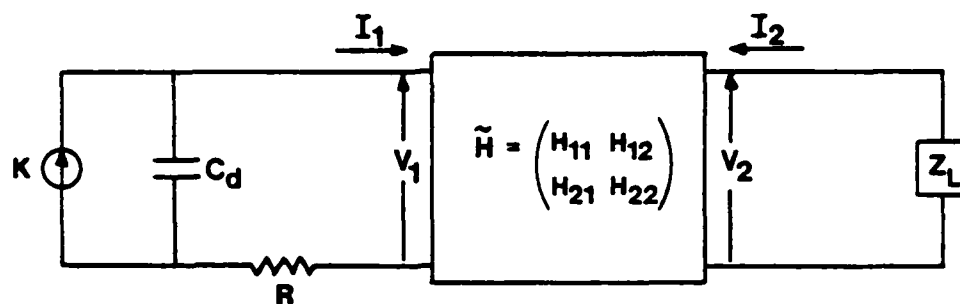
a) Simplified equivalent circuit
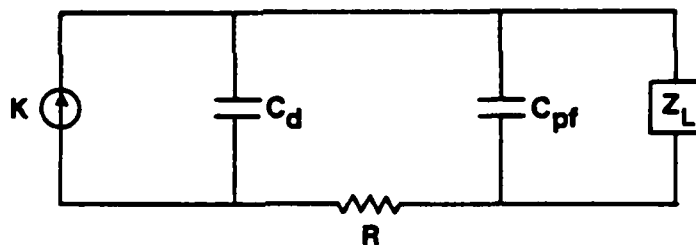
b) $\tilde{H}$ replaced by shunt capacitance

Figure 5.2.   a) Simplified equivalent circuit.   b) Circuit
obtained when $\tilde{H}$ is replaced by a shunt capacitance.

$$V_2 = \frac{KZ_L H_{21}}{[(1-H_{22}Z_L)(H_{11}j\omega C_d - 1 - j\omega C_d R) + H_{12}H_{21}j\omega C_d Z_L]} \qquad (5.13)$$

An important result is obtained: V_2, the voltage measured by the network analyzer, is directly proportional to the terminal current K. As a result, variations in the relative amplitude and phase of K can be measured accurately by the network analyzer, regardless of the values of the circuit elements, provided these circuit elements do not vary with bias voltage.

If all microwave components between the sample and ideal network analyzer are taken to be lossless and perfectly matched, then the two-port network shown in Figure 5.2a consists solely of a shunt capacitance C_{pf} equal to the sum of the package and fringing capacitances, and the equivalent circuit of Figure 5.2b results. Equation (5.13) can be simplified further, and some qualitative observations made.

For a shunt capacitor, by (5.9) and (5.10),

$$H_{11} = 0 \qquad (5.14)$$

$$H_{12} = -H_{21} = 1 \qquad (5.15)$$

$$H_{22} = j\omega C_{pf} \qquad (5.16)$$

with these values, (5.13) becomes

$$V_2 = \frac{K Z_L}{(1 - j\omega C_{pf} Z_L)(1 + j\omega C_d R) + j\omega C_d Z_L} \qquad (5.17)$$

For the parameters of this experiment, $j\omega C_d Z_L$ is the largest term in the denominator. Hence, the detected voltage varies approximately inversely with both frequency and depletion layer capacitance. Both of these dependences were verified experimentally.

As before, the measured voltage is proportional to the terminal current, provided the values of the circuit elements are independent of bias voltage. However, C-V measurements of our samples indicate that the depletion width, and hence both depletion layer capacitance C_d and undepleted zone resistance R_u, are functions of bias voltage.

R_u and C_d both increase with decreasing bias voltage. At some point the ratio of R_u to capacitive reactance $1/\omega C_d$ will be large enough to cause an appreciable phase shift, thereby distorting the measurement of terminal current. This condition is written as

$$R_u = \frac{B_1}{C_d} \qquad (5.18)$$

where B_1 is an undetermined constant. Combining constants, this can be rewritten as

$$\ell_o - \ell = B_2 \ell \qquad (5.19)$$

Since for a given velocity the measured terminal current phase is proportional to sample length, an added fixed phase shift due to circuit effects will have a greater effect on the measured velocity in thinner samples. Hence, the left hand side of (5.19) is normalized to the epitaxial layer thickness:

$$\frac{\ell_o - \ell}{\ell_o} = B_2 \ell \qquad (5.20)$$

Equation (5.20) gives the sample length ℓ at which circuit effects (i.e. voltage dependent depletion layer capacitance and undepleted zone resistance) will cause the measured velocity to deviate from the actual value by a fixed percentage.

Some n-GaAs samples were found to have depletion widths which varied substantially with bias voltage; one example is shown in Figure 3.9. v(E) curves measured for several GaAs samples were seen in Figure 4.11 to "roll-off" at low fields. Sample #27 is the most ideal sample (i.e. high resistivity, constant depletion width); its v(E) characteristic is thus considered to be unaffected at fields above 15 kV/cm, and is used as a reference. The average electric field $<E>_c$ at which measured velocity has

dropped by 5% from the reference curve is listed in Table 5.1 for four GaAs samples of different lengths.

In Table 5.1, B_2 of Equation (5.20) is evaluated for these samples; the average value is 0.027 μm^{-1}. Thus, circuit effects are important when

$$\ell \leq \frac{\ell_o}{1 + .027\ell_o} \qquad (5.21)$$

Equation (5.21) can now be used to find the average electric field below which circuit effects will be appreciable in other samples as well; results are listed in Table 5.1. In GaAs sample #27, which we used as a reference, this field is quite low - 3.5 kV/cm.

In summary, the measured voltage has been shown to be proportional to the terminal current K for the equivalent circuit presented here. The constant of proportionality is complex, and is a function of several circuit elements. Some of these elements, in particular depletion layer capacitance and undepleted zone resistance, are in fact voltage dependent; this dependence is seen to introduce error into the measurements at low fields. The precise evaluation of all circuit parameters is a prerequisite to the accurate correction for circuit effects.

5.3. Avalanche Phenomena

Impact ionization effects determine the diode reverse breakdown voltage, and hence the maximum electric field at

Table 5.1

Critical field $\langle E \rangle_c$ below which

circuit effects are important, and evaluation of B_2

of Equation (5.20)

Sample		$\langle E \rangle_c$ (kV/cm)	ℓ (μm)	ℓ_o (μm)	$B_2 = \dfrac{\ell_o - \ell}{\ell \ell_o}$ (μm^{-1})
n–GaAs	66	26	1.24	1.28	.025
	68	19	2.15	2.26	.023
	38	36	4.59	5.35	.031
	35	35	6.43	7.96	.030
	27	3.5*	3.09*	3.37	
n–Si	61	11.3*	2.79*	3.02	
	65	3.1*	4.51*	5.14	
p–Si	70	6.0*	7.86*	9.98	

*Derived from (5.21)

which microwave time-of-flight measurements are possible. The electron ionization rate α is defined as the number of electron-hole pairs generated by an electron per unit distance. β is the analogously defined ionization rate for holes. Measured ionization coefficients for Si[95] and GaAs[96] are plotted in Figure 5.3 as functions of the electric field.

α and β for both materials show a strong dependence on electric field, rising very rapidly at fields between 150 and 300 kV/cm. Measurements of α and β are usually fit to the following equation:

$$\alpha, \beta = Ae^{-(a/E)^2} \tag{5.22}$$

where the constants A and a are chosen to give the best fit. We infer from the strong field dependence of the ionization coefficients that avalanche effects will not be important in our samples at low fields, but will cause a sharp increase in measured amplitude at some critical field close to the breakdown field.

When the avalanche process is initiated by electrons, the breakdown condition is given by[97]

$$\int_0^\ell \alpha \exp\left[-\int_x^\ell (\alpha-\beta)dx'\right] dx = 1 \tag{5.23}$$

Alternatively, when holes initiate the process, breakdown is governed by
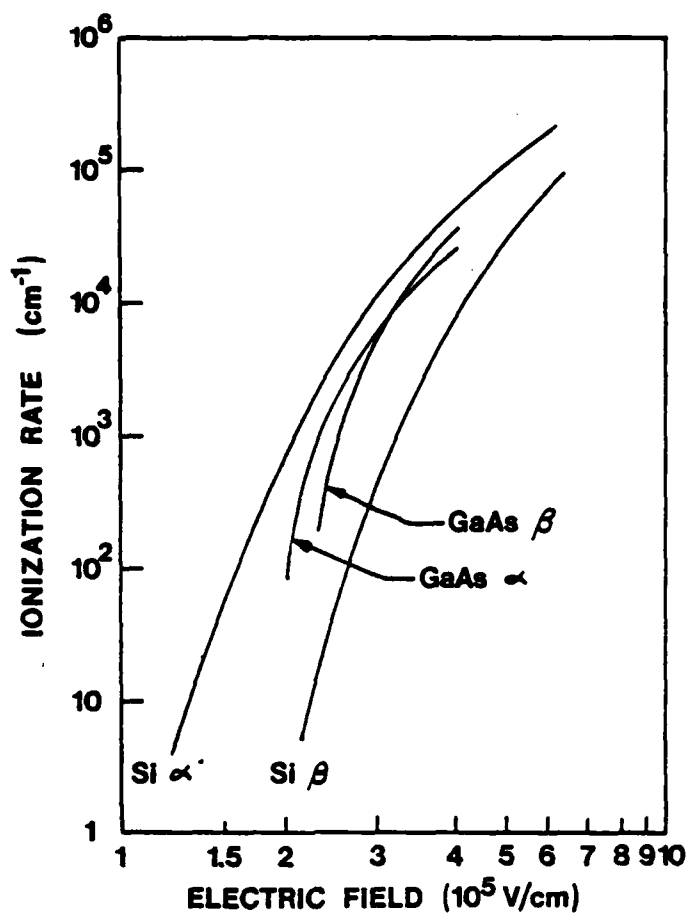
Figure 5.3. Measured ionization coefficient vs. electric
field for Si and GaAs (after Lee et al.[95], Law and
Lee[96]).

$$\int_0^{\ell} \beta \exp \left[- \int_0^{x} (\beta - \alpha) dx'\right] dx = 1 \qquad (5.24)$$

Thinner samples would thus require larger values of α and β (i.e. higher fields) to meet the criterion for breakdown. This is seen experimentally in Table 3.1. The ability of the microwave time-of-flight technique to measure carrier velocity at fields far in excess of those possible with conventional time-of-flight techniques is a direct result of the fact that the avalanche integrals, (5.23) and (5.24), are satisfied at very high electric fields given the small values of ℓ in this experiment.

As might be expected, the maximum fields attained in n-Si (135 kV/cm), n-GaAs (205 kV/cm), and p-Si (235 kV/cm) are in order of decreasing ionization coefficients apparent from Figure 5.3. Although hole velocity in GaAs was not measured in this experiment, it is seen in Figure 5.3 that electron and hole ionization coefficients in GaAs are nearly equal, so that we would expect to be able to measure hole velocity up to a maximum field comparable to that reached in n-type GaAs samples, about 200 kV/cm.

5.4. Electron-Hole Pair Creation

Energetic primary electrons lose energy as they penetrate into a semiconductor. They experience large angle, elastic phonon scattering as well as inelastic

collisions with crystal atoms which ionize the atoms, creating electron-hole pairs. The fraction of incident primary energy needed to form one such pair is independent of the incident electron energy, and is approximately 3 times the band-gap energy.[98]

Measurements of energy dissipation versus penetration distance with primary electron energy as a parameter[61] indicate the distance R over which most of the energy is dissipated (and secondary carrier creation occurs). With slightly different definitions of R, Everhart and Hoff[61] found that in Si

$$R = .017 \ (E_p \ (kV))^{1.75} \ \mu m \qquad (5.25)$$

while Martinelli and Wang[13] determined that, for GaAs,

$$R = .027 \ (E_p(kV))^{1.46} \ \mu m \qquad (5.26)$$

where E_p is the primary electron energy.

It was mentioned in Chapter 2 that 2.5 kV beam electrons lose energy as they pass through the thin surface metallization: upon transmission through a 200 Å Cr film, average energy decreases to approximately 1.7 kV. If this energy is substituted into the above equations, the corresponding range in Si and GaAs is found to be .043 and .058 μm, respectively. However, the depth at which secondary carriers originate, on average, is roughly one-

half of the range.

Thus, for sample length ℓ between 1 and 10 micrometers,

$$R << \ell \tag{5.27}$$

and the approximation that secondary carrier generation occurs at the surface of our samples is valid. Some experimental verification is obtained since the microwave time-of-flight results were unaffected by an increase in beam energy from 2.5 to 3.0 kV.

Note that when (5.27) is not satisfied, the spatial dependence of the pair creation process can be included in an analysis of microwave time-of-flight data, but the contribution of both electrons and holes to the terminal current must be taken into account.

We have assumed in Chapter 2 that the time required for the electron-hole pairs to be created and reach their equilibrium velocity is short relative to the transit time; this assumption is now examined.

In the semiconductor detector literature[100,101] one finds a plasma time τ_p defined as the time required for an external field to separate oppositely charged particles in a plasma. τ_p is proportional to the square of the ratio of the plasma density to the applied field,[101] and for weakly ionizing particles and high fields (as in this experiment) is negligible.

The time necessary for the various scattering
processes to bring secondary carriers created by ionizing
radiation to an equilibrium state is expected to be small
on theoretical grounds, although experimental evidence for
this simply does not exist. In GaAs, for example,
electron-hole pair formation energy is 4.6 eV, of which
the majority is transferred to the electron (by
conservation of momentum and energy, 4.0 eV). Phonon
scattering occurs within times of the order of 10^{-14}
seconds, and calculated scattering rates increase rapidly
with carrier energy.[102] Note that Monte Carlo calculations
of the type reported in [9] can not be used to model this
phenomenon since the band structure is not known at such
high energies.

Despite the apparent lack of conclusive information,
we can infer from our experimental results that the
"relaxation" time discussed above is short relative to the
transit time. One would expect such effects, if
appreciable, to result in v(E) curves which are apparently
functions of the sample length. This was not the case:
in n-GaAs, sample length was varied by a factor of six,
with no significant disagreement between the measured
velocity-field characteristics.

5.5. Trapping

While in transit across a sample, electrons can be
immobilized by "traps", causing the terminal current to

decay with time, resulting in erroneous determination of the carrier velocity. The carrier lifetime, or trapping time τ, is given by [103]

$$\tau = \frac{1}{v N_t \sigma} \tag{5.28}$$

where v is the velocity, N_t the trap density and σ the cross-section for capture. Trapping effects are important in this experiment only when the trapping time is comparable to the transit time.

For neutral material carrier lifetime is of the order of microseconds in Si, and can be less than 100 picoseconds in GaAs.[104] Carrier trapping in a depletion region is less frequent; Ruch and Kino[34] measured a τ of 1 to 10 nanoseconds for depleted GaAs.

Ruch and Kino also found that observed trapping times varied radically for GaAs samples from different wafers, and even for samples from different parts of the same wafer. Hence the consistency of our experimental $v(E)$ curves shown in Figure 4.11 obtained for four GaAs samples from three different wafers leads us to conclude that significant trapping is not present in GaAs samples. Note that transit times for these samples ranged from 8 to 35 picoseconds, much less than any possible trapping times.

5.6. Space Charge Effects

Microwave time-of-flight measurements were performed under small signal conditions: that is, the number of injected carriers is small enough so as not to significantly perturb the static field distribution.

The maximum beam current capable of striking the sample at a given time is approximately one microampere. If the multiplication is 100, and carrier velocity is 5 x 10^6 cm/sec, then the maximum density of beam induced carriers n is given by

$$n = \frac{j}{qv} = 1.3 \times 10^{11} \text{ cm}^{-3} \tag{5.29}$$

By Poisson's equation, such a charge density would produce a change in electric field across a 10 μm GaAs sample of less than 0.02 kV/cm, which is negligible compared to the static electric field strengths used in this experiment.

Space charge instabilities (i.e., Gunn domains) can arise in material such as GaAs which possesses bulk negative differential mobility. The formation of such instabilities is dependent upon the availability of sufficient charge and adequate sample length. More specifically, the following criterion for large space-charge growth (i.e. domain formation) has been derived for GaAs:[105]

$$n_o \ell > 10^{12} \text{ cm}^{-2} \tag{5.30}$$

where n_o is the density of mobile charge, in this case given by (5.29). For the samples of this experiment, the product of charge concentration and sample length is less than 10^8 cm^{-2}; space charge instabilities are therefore not important in the present experiment.

The absence of space-charge effects was confirmed experimentally. Decreasing the incident electron beam current by a factor of fourteen had no discernible effect on measured phase for a 5.35 μm GaAs sample of about 10^{15}cm^{-3} doping.

5.7. Heating

Power flows into the samples from two sources - the beam of energetic electrons impinging on the surface and the external bias voltage supply.

The maximum incident beam current is on the order of one microampere. Thus the power transferred from the 2.5 kV beam to the sample can not exceed

$$(1 \ \mu A)(2.5 \ kV) = 2.5 \ mW.$$

The external bias supply provides power via two components of sample current - the terminal current K, seen in Figure 2.14 to be less than 20 μA for a 5 μm sample, and the parasitic reverse leakage current, which is also less than 20 μA. For the largest bias voltage

used, 200 volts, power into the sample might be as high as

(40 µA) (200 V) = 8 mw.

In this worst case analysis, total power flowing into the device is thus about 10 mW, a level sufficiently small that no significant heating occurs, given that samples are mounted in packages which are relatively efficient heat sinks.

For comparison, it should be mentioned that an IMPATT diode of comparable size with a power input of a few watts operates at 200°C. By crude scaling, one can estimate the temperature rise in our devices to be less than one degree Kelvin, i.e. negligible with respect to variations in "room temperature".

5.8. Stability

To be meaningful, an experiment requires at least some degree of stability. As a rule, experimental parameters must remain constant during the time required to perform the necessary measurements. In this experiment, drift in quantities such as frequency, beam accelerating potential, and x-y deflection voltages can interfere with measurement accuracy. In the present work an effort has been made to reduce both drift and its effects.

1.0

1.1

1.25   1.4   1.6

45   2.8   2.5

50   3.2   2.2

36

40   2.0

1.8
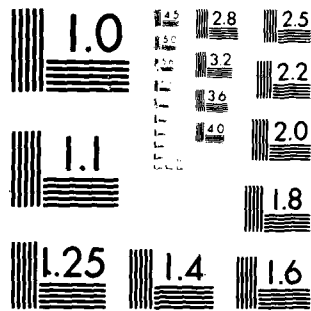
MICROCOPY RESOLUTION TEST CHART
NATIONAL BUREAU OF STANDARDS 1963-A

Equipment is warmed up prior to measurements. In addition, a regulated power supply provides constant ac voltage to the most critical equipment, i.e. the electron gun high voltage supply and x-y deflection source.

The velocity of beam electrons is given by

$$v = (\frac{2qV}{m})^{1/2} = 2.97 \times 10^7 \text{ m/sec} \tag{5.31}$$

where q is the electronic charge, V the accelerating potential, and m the electronic mass. The number of periods corresponding to frequency f required for an electron to travel from the deflection cavity to the sample, a distance of 18 cm, is given by

$$n = \frac{(18 \text{cm}) (f)}{(\frac{2qV}{m})^{1/2}} \tag{5.32}$$

and is 32.2 at 5.3 GHz. From (5.30) it can be shown that if the frequency changes by 1 MHz or the accelerating potential by 1 volt, a phase shift of approximately 2° results. Measured quantities are thus sensitive to minute variations in f or V.

The effect of frequency drift is reduced when the network analyzer reference and test channels are of equal electrical length. In the present experiment, this is accomplished by adding an appropriate length of coaxial cable to the reference channel.

A typical measurement, in which amplitude or phase is recorded as a function of bias voltage, requires less than 10 seconds. After taking the precautions stated above, experimental stability over such times was found to be good, i.e. data was highly reproducible.

CHAPTER 6

TRANSIENT EFFECTS

6.1. <u>Velocity Overshoot</u>

Monte Carlo calculations have shown[9,106-108] that
when an electric field is instantaneously applied to a
semiconductor containing carriers at thermal equilibrium,
on average, the carriers reach a new steady-state drift
velocity within a time which is of the order of the
energy relaxation time. If the field is large enough
carriers can be accelerated within this time to average
velocities in excess of the final equilibrium value
before momentum and energy relaxation processes cause the
system to reach a steady state. This velocity
"overshoot" phenomenon can strongly influence the
performance of devices with sub-micron
dimensions.[109,110]

Recent experiments[111,112] are claimed to have
confirmed the existence of velocity overshoot in GaAs.
These experiments, based upon optical phenomena such as
photoconduction[112] and the Franz-Keldysh effect,
suffer from the disadvantage of being rather indirect.
One of the original objectives of this work was to
detect and quantify the velocity overshoot effect in
GaAs.

179

6.2. Experimental Detection

Since the overshoot phenomena rarely last for greater than one micron of transit length, time-of-flight experiments to detect overshoot must be performed on samples of length 1 μm or less. For such short samples and the range of electron drift velocity in GaAs, no amplitude extrema will be observed since the phase ϕ is much less than π; for example, at 5.3 GHz phase for a 1.28 um GaAs sample was measured as less than 20° for all bias voltages. It was seen in Chapter 2 that when the phase is small, the amplitude remains virtually constant with velocity; only phase data is therefore useful in thin layers.

Since the general expression for phase, Equation (2.15), can be evaluated if $v(x)$ is known, it was possible to compute expected phase differences for typical overshoot velocity-distance behavior calculated by Monte Carlo methods.[9] Computer program "CALC" was used to calculate the 5.3 GHz phase ϕ which would be measured in GaAs samples of 0.5 and 1.0 μm length at the fields shown. The "apparent" velocity, defined by

$$V_{app} = \frac{\omega \ell}{2\phi} \qquad (6.1)$$

is plotted in Figure 6.1 along with the steady-state velocity-field characteristic. Although the form of
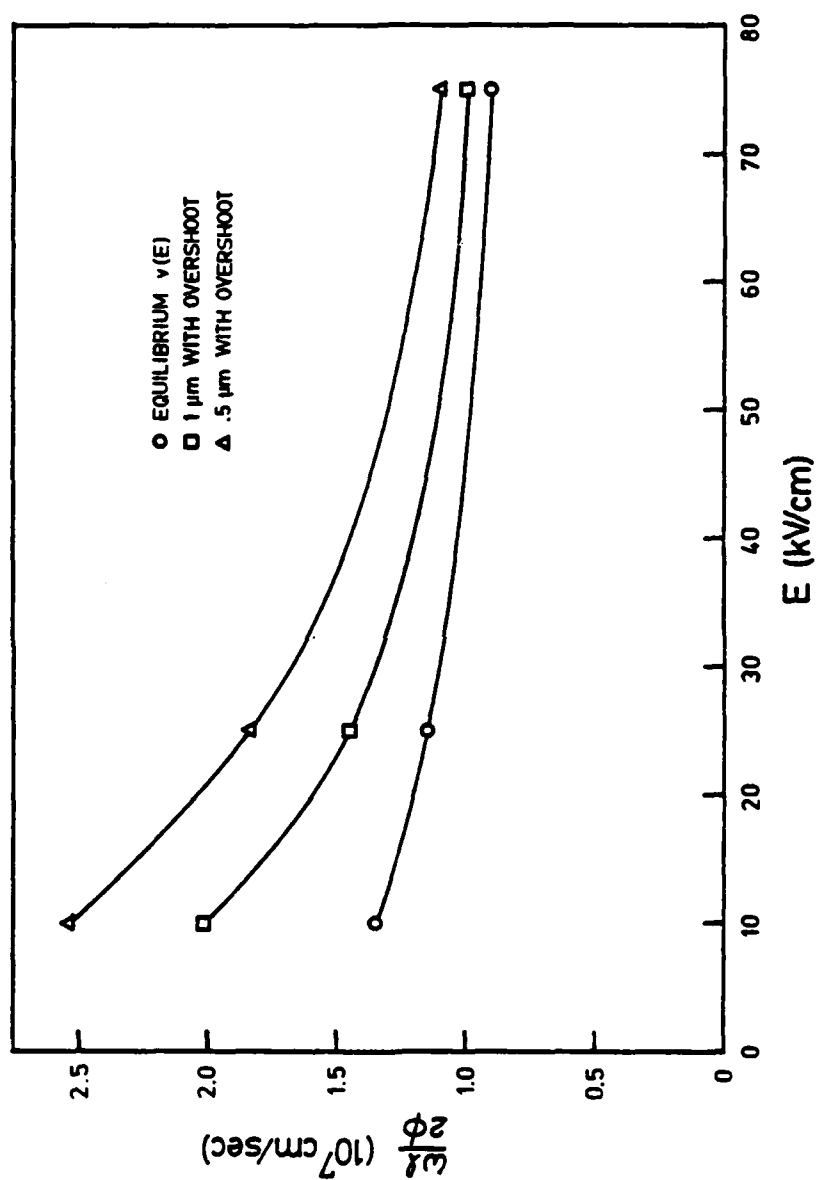
Figure 6.1. Apparent velocity vs. field calculated for thin GaAs layers.

(2.15) is complex, calculations have shown that for small phase angles the apparent velocity is approximately equal to the average velocity given by

$$v_{ave} = \frac{\ell}{\tau} \tag{6.2}$$

where the transit time τ is given by

$$\tau = \int_0^x \frac{dx'}{v(x')} \tag{6.3}$$

Two conclusions can be drawn from Figure 6.1: first, the apparent velocity increases as sample length decreases, and overshoot becomes more important. Second, for the fields shown, the effect of overshoot on measured phase, and hence average velocity, decreases with increasing field.

A microwave time-of-flight measurement to observe overshoot could be performed as follows: a thick (3 to 4 μm) epitaxial GaAs layer could be thinned selectively, producing samples with thicknesses ranging from 0.5 to 4 μm. Since the effect of transients decreases with field, and absolute velocity determination in thin layers is impossible, measured phase for these samples must be matched at the highest field possible, yielding curves which are expected to diverge at low fields as do those of Figure 6.1. One could then iteratively apply Equation (2.15) to determine a $v(x)$ which is consistent with the

measured behavior. In order to resolve features of the 10 kV/cm v(x) curve of reference 9, however, samples as thin as 0.2 μm would required, and a number of problems might arise. These include non-negligible beam penetration distance, potentially inadequate phase resolution, and circuit effects due to the large sample capacitance.

For valid results to be obtained, samples must be from the same starting wafer, since electron drift velocity is dependent upon low-field mobility (i.e. doping and defect density, quantities which can vary substantially from one wafer to the next). Also, it is invalid to perform measurements on a single thin layer and compare results to an equilibrium v(E) generated by Monte Carlo calculations since such a v(E) may disagree with steady-state experimental results. For example, the steady-state v(E) calculated by Kratzer was found to differ from the experimental results of Chapter 4 by as much as 20%. It is important to recognize the fact that Monte Carlo calculations can be relatively inaccurate, since they are based on material parameters which may not be known with certainty, and are normally adjusted to give the best agreement with experimental results.

Does this experiment have the resolution necessary to measure the small changes in phase produced by velocity overshoot? At 10 kV/cm the calculated phase for a 1 μm sample decreases by 2.35 degrees when overshoot is included. Experimental resolution is illustrated in

Figure 6.2, which presents phase data for the thinnest
sample tested, a 1.28 μm GaAs layer. In this case,
relative phase can be determined to within ± .2°. Since
the phase data is matched at a high field point the low
field phase has an associated error of ± .4°, and
resolution should therefore be sufficient to permit the
detection of overshoot in a 1 μm sample. Note that a
phase resolution of 0.4° corresponds to a transit time
resolution of approximately .4 pSec.

Measured v(E) was reported in Figure 4.11 for two
GaAs samples of different thickness from the same wafer;
samples #66 and #68 have lengths of 1.28 and 2.26 μm,
respectively. From the discussion presented thus far one
would expect that the velocity-field curve of the thinner
sample should lie above that of the thicker sample at
fields below about 25 kV/cm. However, due to the
relatively high doping level ($\sim 10^{15}/cm^3$) of both samples
and resulting undepleted epitaxial regions, circuit
effects are important in both samples at fields below 40
kV/cm, and v(E) results are inconclusive. Recall from
Chapter 5 that correction for circuit effects is possible
only after accurate evaluation of all equivalent circuit
parameters, and that the accuracy of such a correction
would be limited by the inaccuracy of the equivalent
circuit values. The estimated uncertainty associated with
a single equivalent circuit parameter is on the order of
10%. Since an expression used to correct measured phase
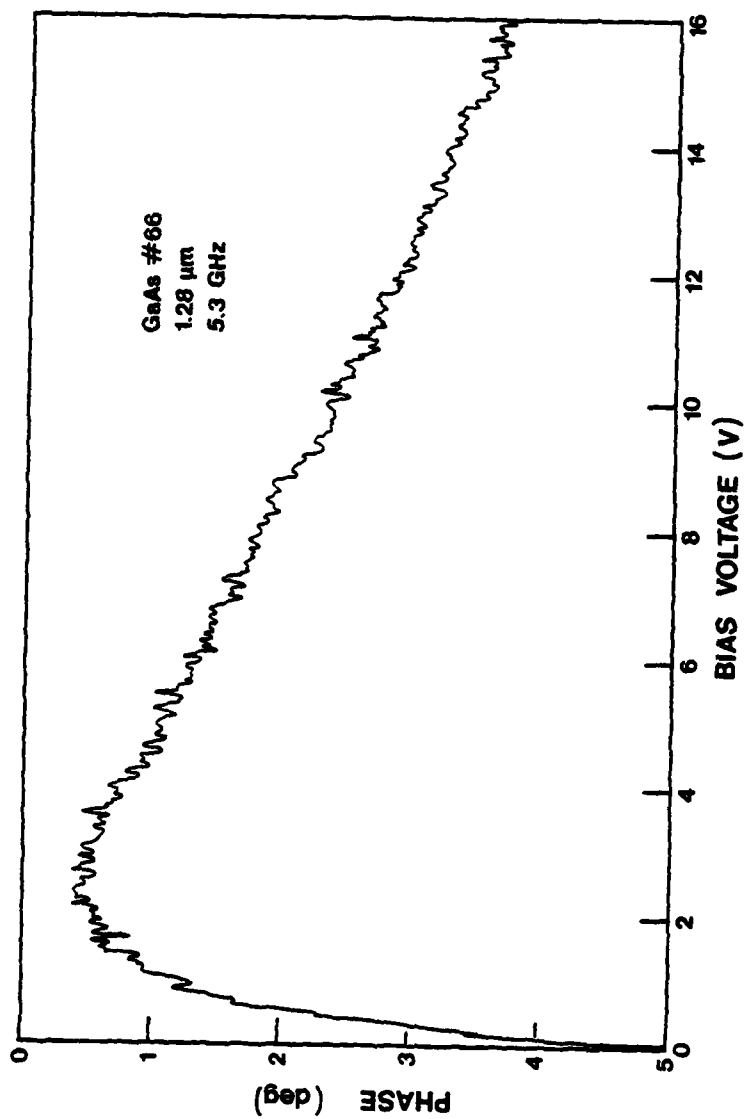
Figure 6.2. 5.3 GHz phase data for sample #66, indicating resolution of phase measurements.

for circuit effects would contain several terms of roughly equal uncertainty, the total error of a circuit effect correction could be quite large. Note that epitaxial layers with doping on the order of 10^{14} cm^{-3} would permit direct measurements to be made in the 10 to 25 kV/cm field range without appreciable circuit effects.

We have seen in Chapter 2 that diffusion can cause the measured apparent velocity to exceed the true value, and that this effect increases as sample length decreases. Diffusion and velocity overshoot therefore have the same qualitative effect on measured phase. Let us assume first that there are no transient effects, i.e. velocity overshoot does not occur. Equation (1.3) is then valid, and the effect of diffusion can be investigated.

The diffusivity is large, but not known with confidence in GaAs in the field range 10 to 25 kV/cm. Reported diffusivity[34,113] at 10 kV/cm ranges from 50 to 270 cm^2/sec. The results of [34] and [113], when extrapolated at a constant value to higher fields, yield a range of 20 to 150 cm^2/sec at 25 kV/cm. The effect of diffusion on measured phase was calculated with program "EXPT". As seen in Figure 6.3, the apparent velocity is greater than the steady-state value, and the uncertainty in diffusivity results in a wide range of possible measured apparent velocities. The most important conclusion to be drawn from this calculation is that even if overshoot is not present, diffusion can cause the
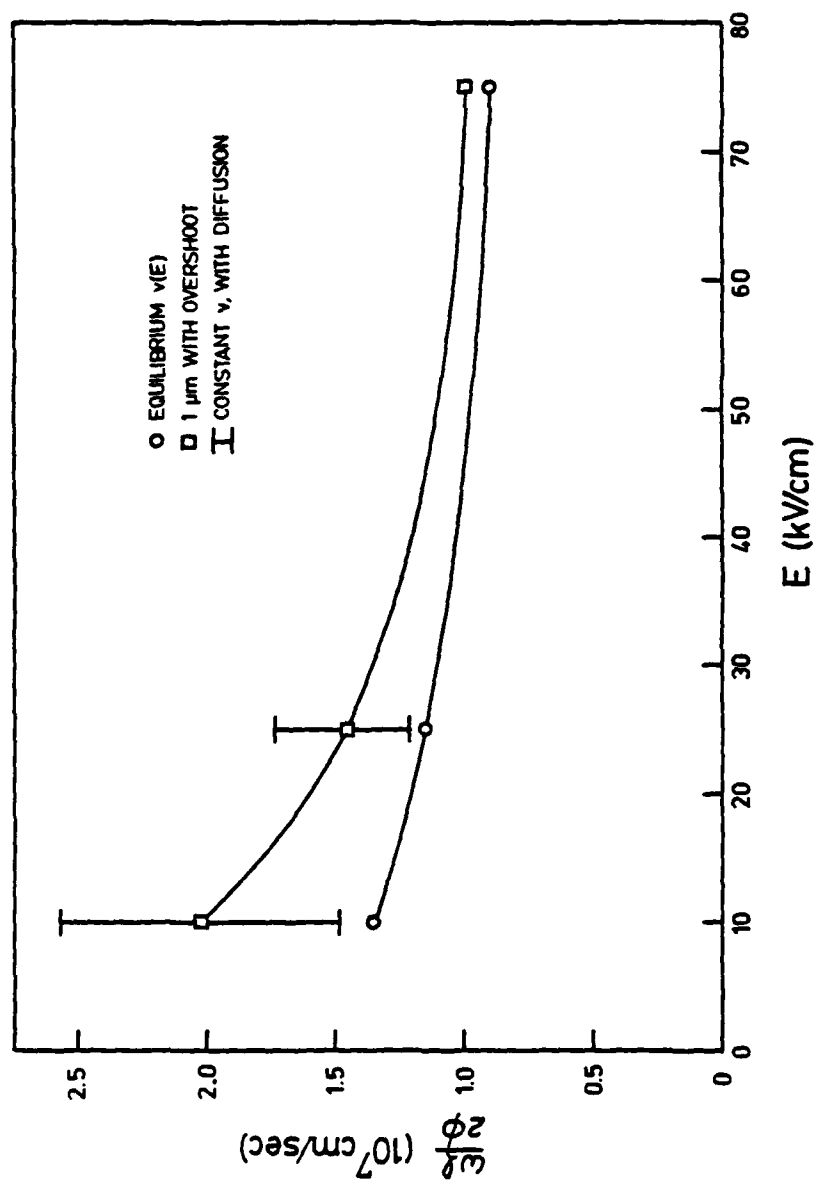
Figure 6.3. Effect of diffusion on measured apparent velocity for a 1 μm GaAs sample.

experimental results to exhibit the behavior associated with overshoot.

In reality, some transients will be present. We must therefore return to the general transport equations, which contain terms associated with velocity transients as well as terms involving diffusion (i.e. of the form ∇nkT). Thus diffusion will still occur in the presence of transient effects, although it would be difficult to decouple the two phenomena. Two suggestions are made:

1. Using the general transport equations, evaluate all terms and, if possible, decouple velocity transients from diffusion effects.

2. It may be possible to reduce diffusion effects to a negligible level by optimizing the electron beam modulation so as to reduce carrier gradients.

Some questions have been raised[114-117] about the correctness of comparing results of the microwave time-of-flight experiment with Monte Carlo calculations for overshoot. In particular, Monte Carlo calculations that have been performed start with electrons at thermal equilibrium, located in the central Γ valley, when the field is applied. However, an electron beam produces secondary carriers which are initially "hot" and cascade down the bandstructure to their equilibrium positions. As stated in Chapter 5, this process, which precludes the occurrence of velocity overshoot, is believed to

equilibrate more rapidly than overshoot. Cook has performed some calculations[116] based on a relaxation time model, which show that for electrons having initial energies greater than 0.6 eV (such as those created by an electron beam), velocity overshoot does not occur. Instead, calculated electron velocity increases monotonically to its steady-state value within a time much shorter than that required for the overshoot process. If diffusion and circuit effects can be properly removed, and transient effects are measurable, a measurement with the existing microwave time-of-flight experiment in conjunction with an appropriate Monte Carlo computation could, however, yield useful information on the energy spectrum associated with the generation of electron-hole pairs by particle irradiation.

Since carrier excitation by photons having energy slightly greater than the band gap would initially populate the central valley, the velocity overshoot phenomenon predicted by Monte Carlo calculations could occur with optically excited carriers. Constant et al.[117] have assembled a microwave time-of-flight experiment with optical excitation, but have encountered difficulties: First, optical modulation is currently limited to frequencies below about 2 GHz. At their operating frequency, 1 GHz, changes in phase (which is roughly proportional to frequency) can be difficult to resolve. Also, the optical absorption constant of

GaAs[118] for a photon energy equal to the band gap (1.44 eV) is about 6×10^{-3} cm^{-1}, indicating that penetration depth effects could be important. Finally, it is clear from our calculations that diffusion must be considered in the analysis of microwave time-of-flight data before valid conclusions can be drawn.

CHAPTER 7

CONCLUSIONS

7.1. <u>Summary and Conclusions</u>

A microwave time-of-flight experiment has been used
to study the high field transport properties of
semiconductors.

In Chapter 2 a general theory was presented from
which expressions were derived relating the carrier
velocity as a function of position to the amplitude and
phase of each Fourier component of the test device
terminal current. The assumptions and approximations
which were made to arrive at this result are justified
in Chapter 5, in some cases with experimental evidence.

In order to include diffusion, numerical simulation
of carrier motion through the test device, duplicating
experimental conditions, was necessary. The effects of
both electric field non-uniformity and diffusion on
terminal current were examined, and methods were
developed to allow the magnitude of such effects to be
evaluated in experimental samples.

Measurements were performed at 5.3 and 10.6 GHz for
a number of n-Si, p-Si and n-GaAs samples ranging in
thickness from 1 to 10 micrometers. Measured amplitude
extrema provided discrete, absolute values of velocity.
Since only relative phase can be measured in this
experiment, velocities obtained from phase data were

matched to an absolute reference point. When necessary, corrections were applied for the two most important secondary effects, field taper and diffusion. In general, the magnitude of both effects was found to decrease with increasing electric field, and was less than 5% for the results reported here.

The measured velocity-field curves are compiled in Figure 7.1. All three curves agree with other time-of-flight results[40,43,44] to within about 3% at low fields, and extend to considerably higher fields. In p-Si, for example, previous time-of-flight measurements were limited to fields below 50 kV/cm, but in this experiment the maximum field is 235 kV/cm. The velocity-field results can be summarized as follows:

1. Electron velocity in silicon has been measured for fields from 5 to 135 kV/cm. A saturated velocity of $1.10 \pm .08 \times 10^7$ cm/sec was reached at 115 kV/cm.

2. The measured electron velocity in GaAs is seen to decrease steadily with increasing electric field, from $0.86 \pm .04 \times 10^7$ cm/sec at 40 kV/cm to $0.60 \pm .03 \times 10^7$ cm/sec at 205 kV/cm.

3. The velocity-field characteristic for holes in silicon was measured for fields ranging from 9 to 235 kV/cm, and velocity saturation observed for the first time. The measured saturation velocity of $0.96 \pm .05 \times 10^7$ cm/sec is reached at 175 kV/cm.

The spreading diffusion of electrons in GaAs has
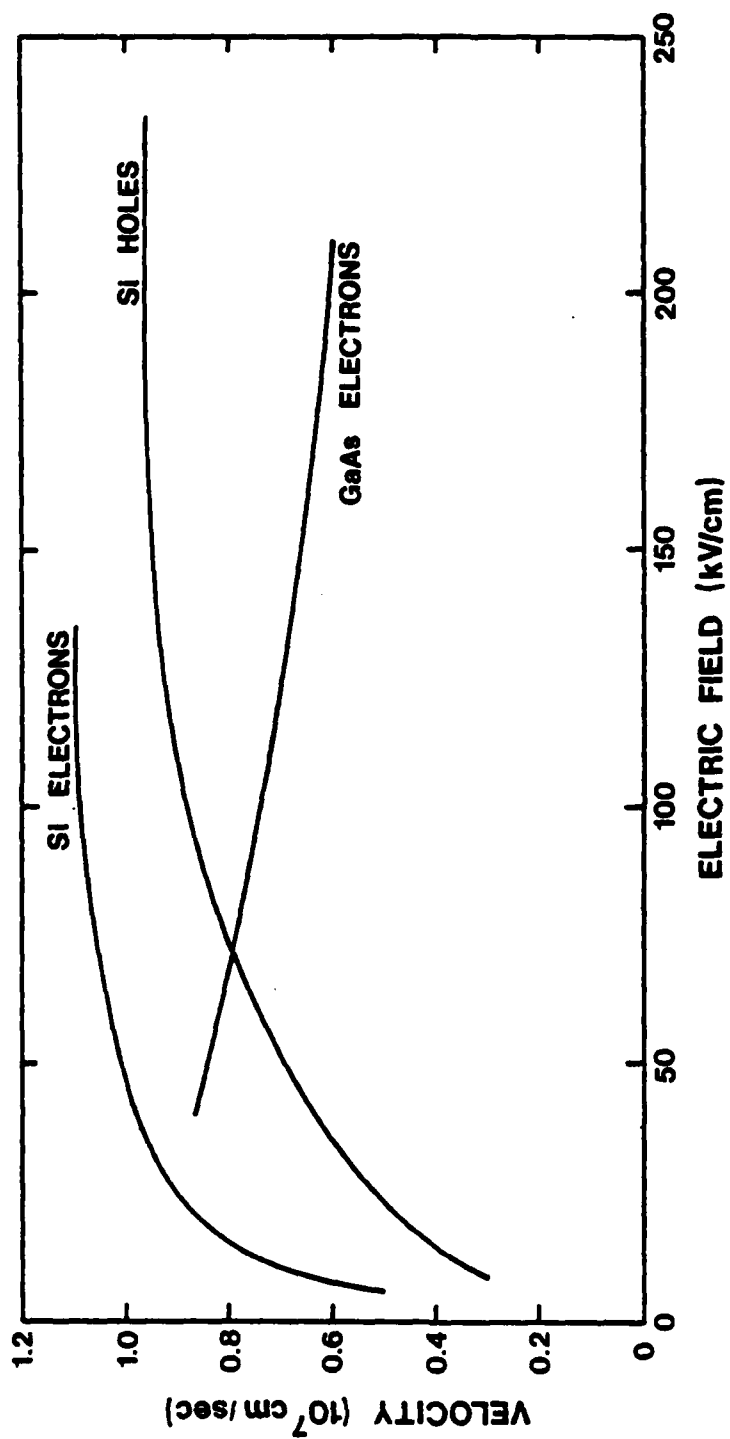
Figure 7.1. Velocity-field results obtained at 300 K for (111) Si and (100) GaAs.

been studied. Two techniques by which the microwave time-of-flight experiment can yield high field diffusivity have been presented. In one, the relative sharpness of an amplitude minimum is seen to be a function of diffusivity. The second technique utilizes the fact that the effect of diffusion on measured phase is more pronounced in thin samples than in thick ones, so that velocity-field curves derived from phase measurements vary with sample length. For GaAs, we have determined that electron diffusivities of 5 ± 5 cm^2/sec at 64 kV/cm, and 29 ± 8 cm^2/sec at 170 kV/cm are consistent with our experimental data.

Since the experiment is capable of resolving carrier transit times to within a fraction of a picosecond, it would seem well suited to the detection of transient effects. Although carriers produced by energetic particle irradiation (i.e. electron beams) probably do not experience the velocity overshoot phenomenon predicted by the usual type of Monte Carlo calculations, a microwave time-of-flight experiment in which carriers are excited by optical means would result in the occurrence, and possibly the detection, of velocity overshoot.

7.2. Suggestions For Future Work

If absolute rather than relative phase could be measured in this experiment, then velocity-field results

could be obtained for thin layers without the use of a reference point. Methods of calibrating the experimental system, thereby allowing absolute phase to be determined, are described in Appendix F.

Experiments should be performed at a variety of temperatures, although this would first require the construction of a more complicated sample holder. Temperature dependence of measured quantities would provide an extensive set of experimental data which Monte Carlo transport calculations would attempt to fit, in the process arriving at a set of physical material parameters, some of which are at present not well known. Temperature dependent measurements could be used in conjunction with device simulation work to more accurately predict the performance of devices which operate at various temperatures (i.e., IMPATT's or power FET's), or to determine the temperature required for optimum device operation.

The microwave time-of-flight experiment has provided a large amount of new velocity-field data for carriers in silicon and GaAs, the two semiconductors most widely studied in recent years. The high field transport properties of other materials such as Ge, InP, CdTe, and a host of ternary and quaternary compounds (as well as p-GaAs) are not well known, and could be measured with this experiment.

The experiment is especially well suited to the characterization of new materials because it is compatible with thin expitaxial layers, such as might be produced by molecular beam epitaxy (MBE) and doping levels as high as 10^{15} cm^{-3}. It should be noted that compensation, which might be necessary to reduce the net ionized impurity density to an acceptable level, is not expected to affect results obtained at very high fields.

Although only epitaxial layers on conducting substrates have been considered thus far, a test configuration which would permit the testing of layers formed on insulating substrates (i.e. silicon on sapphire, laser annealed polycrystalline silicon, etc.) is shown in Figure 7.2. Note that a high conductivity layer is still required to collect the carriers, and that this layer must be sufficiently thick to keep the associated series resistance relatively small.

The simplicity of this experiment makes it ideally suited to the examination of a number of physical processes which occur in samples at high fields. Carrier diffusivity has been measured in n-type GaAs. While drift velocity is not accurately known for many materials, high field diffusivity measurements are practically nonexistent, and should therefore be performed.

With appropriate models, other phenomena such as impact ionization and trapping could be studied with the
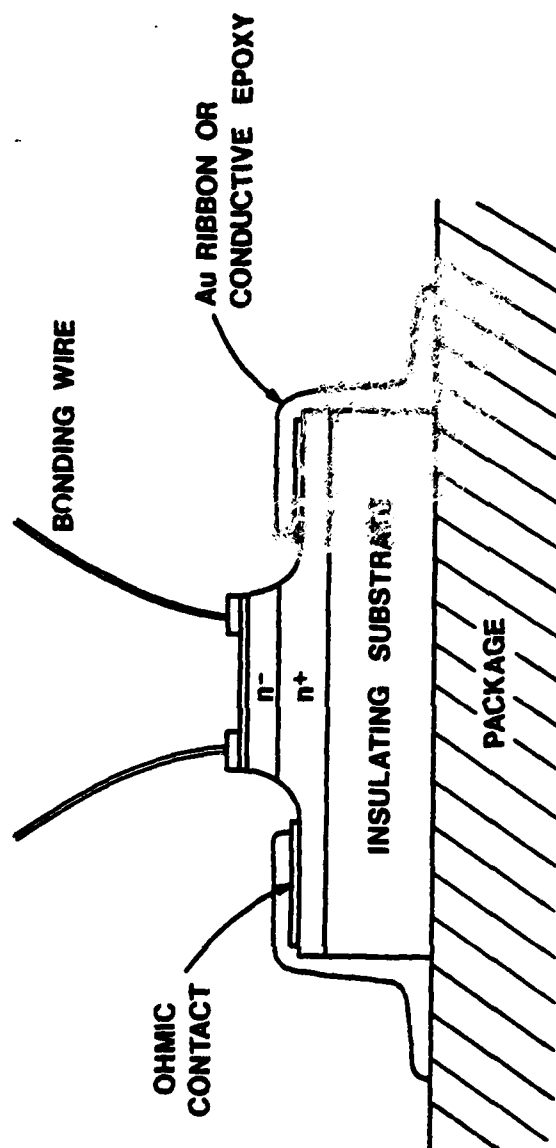
Figure 7.2. Proposed structure for testing n-type samples with insulating substrates.

microwave time-of-flight experiment. In particular, subpicosecond experimental resolution may permit time dependences of these and other effects to be determined.

A.1. Program "CALC"

This program computes amplitude and phase of one
frequency component of terminal current for a specified
$v(x)$ according to Equations (2.14) and (2.15), both of
which contain double integrals. If $v(x)$ is approximated
by a piecewise linear function, the inner integral can be
evaluated analytically as a sum of terms, each of which is
determined as follows:

$$v_i(x) = Ax + B \qquad (x_i < x < x_{i+1}) \qquad \text{(A.1.1)}$$

where

$$A = \frac{v_{i+1} - v_i}{x_{i+1} - x_i} \qquad \text{(A.1.2)}$$

$$B = \frac{v_i x_{i+1} - x_i v_{i+1}}{x_{i+1} - x_i} \qquad \text{(A.1.3)}$$

For a linear $v(x)$ we have

$$\int_{x_i}^{x_{i+1}} \frac{dx}{v_i(x)} = \frac{1}{A} \ln \left(\frac{B + A\, x_{i+1}}{B + A\, x_i}\right) \quad (v_{i+1} \neq v_i) \qquad \text{(A.1.4)}$$

$$= \frac{x_{i+1} - x_i}{v_i} \qquad (v_{i+1} = v_i)$$

Note that if either v_i or v_{i+1} is equal to zero, the

integral will not converge. However, convergence is excellent

if the velocity at a discontinuity of this type is taken

to be very small, typically two or three orders of magnitude

below average drift velocities. The second integration is

then performed numerically.

Frequency and Δx are requested by the program; $v(x)$ is

read from a data file. A listing of the program appears

on the next page.

```
C         ************************ PROGRAM CALC ************************
C
C         THIS PROGRAM CALCULATES AMPLITUDE AND PHASE OF ONE FREQUENCY
C         COMPONENT OF THE TERMINAL CURRENT FOR A SPECIFIED V(X).
C
          DIMENSION X(50),V(50),Y(1500),U(1500)
          REAL MAG
C
C         ENTER INPUT PARAMETERS
          WRITE(7,1)
1         FORMAT(' ENTER FREQUENCY (GHZ)')
          READ(5,*) FREQ
          WRITE(7,2)
2         FORMAT(' ENTER DX (UM)')
          READ(5,*) DX
C
C         READ V(X) FROM DATA FILE
          OPEN(UNIT=15,NAME='DX1:VX.DAT',TYPE='OLD')
          I=0
3         I=I+1
          READ(15,*) X(I),V(I)
          IF(X(I).EQ.0.0.AND.V(I).EQ.0.0) GO TO 4
          GO TO 3
4         JJ=I-1
C
C         ASSIGN VELOCITY TO EACH MESH POINT
          NDX=INT(X(JJ)/DX+.999)
          DO 7 J=1,NDX
          Y(J)=FLOAT(J-1)*DX
          DO 5 I=2,JJ
          IF(Y(J).LT.X(I)) GO TO 6
5         CONTINUE
6         U(J)=V(I-1)+(V(I)-V(I-1))*(Y(J)-X(I-1))/(X(I)-X(I-1))
7         CONTINUE
          U(NDX+1)=V(JJ)
          IF(U(NDX+1).EQ.0.0) U(NDX+1)=U(NDX)
          Y(NDX+1)=X(JJ)
C
C         INITIALIZE SUMS
          T=0.0
          CO=0.0
          SI=0.0
          W=6.283E9*FREQ
C
C         INTEGRATE OVER SAMPLE LENGTH
          DO 9 I=1,NDX
          IF(U(I+1).EQ.U(I)) D=W*DX/(U(I)*1.E11)
          IF(U(I+1).EQ.U(I)) GO TO 8
          A=(U(I+1)-U(I))/DX
          B=U(I)-A*Y(I)
          D=(W/(1.E11*A))*ALOG((A*Y(I+1)+B)/(A*Y(I)+B))
8         T=T+D
          CO=CO+(COS(T)+COS(T+D))*DX/(2.*X(JJ))
          SI=SI+(SIN(T)+SIN(T+D))*DX/(2.*X(JJ))
9         CONTINUE
C
          MAG=(CO*CO+SI*SI)**0.5
          PHASE=57.3*ATAN(SI/CO)
          IF(PHASE.LT.0.0) PHASE=PHASE+180.
          WRITE(7,10) FREQ,X(JJ)
10        FORMAT('0','FREQUENCY= ',F5.2,' GHZ',7X,'L=',F6.3,' UM')
          WRITE(7,11) MAG,PHASE
11        FORMAT(' AMP=',F6.3,7X,'PHASE=',F6.2,' DEGREES')
          STOP
          END
```

A.2   Program "E"

```
C       ************************ PROGRAM E ************************
C
C       THIS PROGRAM IS USED TO DETERMINE THE EFFECTS OF NON-UNIFORM
C       ELECTRIC FIELD ON SAMPLE TERMINAL CURRENT AMPLITUDE AND
C       PHASE.  FIRST, E(X) IS CALCULATED FROM POISSON'S EQUATION
C       FOR A SPECIFIED BIAS VOLTAGE GIVEN THE DOPING PROFILE N(X).
C       E(X) AND AN ASSUMED V(E) ARE THEN COMBINED INTO A V(X)
C       WHICH ALLOWS AMPLITUDE AND PHASE TO BE COMPUTED.
C
        DIMENSION DELE(50),X(50),E(50),S(50),F(50),V(50)
        DIMENSION Y(1500),U(1500)
        REAL N(50),NO,MAG
C
C       ENTER INPUT PARAMETERS
        WRITE(7,51)
51      FORMAT(' ENTER RELATIVE DIELECTRIC CONSTANT (SI=11.8, GAAS=13.1)')
        READ(5,*) EPS
        EP=EPS*8.85E-12
        WRITE(7,52)
52      FORMAT(' ENTER FREQUENCY (GHZ)')
        READ(5,*) FREQ
        WRITE(7,53)
53      FORMAT(' ENTER DX (UM)')
        READ(5,*) DX
        WRITE(7,54)
54      FORMAT(' ENTER BUILT-IN VOLTAGE (V)')
        READ(5,*) VBI
        WRITE(7,55)
55      FORMAT(' TYPE 1 TO PRINT E(X), 0 TO SKIP')
        READ(5,*) LP
C
        OPEN(UNIT=15,NAME='DX1:NX.DAT',TYPE='OLD')
        OPEN(UNIT=16,NAME='DX1:VE.DAT',TYPE='OLD')
C
C       READ N(X) FROM DATA FILE
        I=0
1       I=I+1
        READ(15,*) X(I),N(I)
        IF(N(I).EQ.0.) GO TO 2
        GO TO 1
2       J=I-2
C
C       READ V(E) FROM DATA FILE
        I=0
3       I=I+1
        READ(16,*) F(I),S(I)
        IF(F(I).EQ.-1.) GO TO 4
        GO TO 3
4       NN=I-2
C
C       CALCULATE ELECTRIC FIELD PROFILE
        DO 5 I=1,J
        DELE(I)=.801E-24*(N(I)+N(I+1))*(X(I+1)-X(I))/EP
5       CONTINUE
C
        JJ=0
6       WRITE(7,56)
56      FORMAT('0','ENTER VBIAS,X(UM),N(CM-3)')
        READ(5,*) VMEAS,XO,NO
        IF(XO.EQ.0.) GO TO 22
        IFLAG=1
        I=0
7       I=I+1
        IF(XO.GT.X(I)) GO TO 7
        J=I-1
        E(J)=.801E-24*(NO+N(J))*(XO-X(J))/EP
```

```
8          J=J-1
           IF(J.EQ.0) GO TO 9
           E(J)=E(J+1)+DELE(J)
           GO TO 8
C
9          K=I-2
           VOLT=E(K+1)*(X0-X(K+1))/20.
           DO 10 J=1,K
           VOLT=VOLT+(E(J)+E(J+1))*(X(J+1)-X(J))/20.
10         CONTINUE
C
           IF(LP.EQ.1) WRITE(7,57) VMEAS
57         FORMAT('0',8X,'BIAS VOLTAGE=',F6.2,' VOLTS')
           IF(LP.EQ.1) WRITE(7,58) VOLT
58         FORMAT(' ',8X,'INTEGRAL OF E(X)=',F6.2,' VOLTS')
           IF(LP.EQ.1) WRITE(7,59)
59         FORMAT(' ',8X,'X(UM)',4X,'E(KV/CM)')
C
           KK=I-1
           DO 11 J=1,KK
           IF(LP.EQ.1) WRITE(7,60) X(J),E(J)
60         FORMAT(7X,F6.3,4X,F7.3)
11         CONTINUE
           IF(LP.EQ.1) WRITE(7,61) X0
61         FORMAT(7X,F6.3,6X,'0.000')
           IF(IFLAG.EQ.0) GO TO 13
C
C          CORRECT E(X)
           JJ=1
           DE=10.*(VOLT-VMEAS-VBI)/X0
           DO 12 J=1,KK
           E(J)=E(J)-DE
           IF(E(J).LT.0.) E(J)=E(J-1)*(X0-X(J))/(X0-X(J-1))
12         CONTINUE
           IF(LP.EQ.1) WRITE(7,62)
62         FORMAT('0',8X,'CORRECTED E-FIELD PROFILE')
           IFLAG=0
           GO TO 9
C
C          ASSIGN V TO POINTS AT WHICH N(X) WAS GIVEN
13         DO 16 J=1,KK
           DO 14 I=2,NN
           IF(E(J).LT.F(I)) GO TO 15
14         CONTINUE
15         V(J)=S(I-1)+(S(I)-S(I-1))*(E(J)-F(I-1))/(F(I)-F(I-1))
16         CONTINUE
           V(KK+1)=.01*S(2)
C
C          ASSIGN V TO EACH MESH POINT
           NDX=INT(X0/DX+.999)
           DO 19 J=1,NDX
           Y(J)=FLOAT(J-1)*DX
           DO 17 I=2,KK
           IF(Y(J).LT.X(I)) GO TO 18
17         CONTINUE
18         U(J)=V(I-1)+(V(I)-V(I-1))*(Y(J)-X(I-1))/(X(I)-X(I-1))
19         CONTINUE
           U(NDX+1)=.01*S(2)
           Y(NDX+1)=X0
C
C          INITIALIZE VARIABLES
           T=0.0
           C0=0.0
           SI=0.0
           W=6.283E9*FREQ
```

```
C          PERFORM INTEGRATION
           DO 21 I=1,NDX
           IF(U(I+1).EQ.U(I)) D=W*(Y(I+1)-Y(I))/(U(I)*1.E11)
           IF(U(I+1).EQ.U(I)) GO TO 20
           A=(U(I+1)-U(I))/(Y(I+1)-Y(I))
           B=U(I)-A*Y(I)
           D=(W/(1.E11*A))*ALOG((A*Y(I+1)+B)/(A*Y(I)+B))
20         T=T+D
           CO=CO+(COS(T)+COS(T+D))*(Y(I+1)-Y(I))/(2.*XO)
           SI=SI+(SIN(T)+SIN(T+D))*(Y(I+1)-Y(I))/(2.*XO)
21         CONTINUE
C
C          COMPUTE AND PRINT AMPLITUDE AND PHASE
           MAG=(CO*CO+SI*SI)**0.5
           PHASE=57.3*ATAN(SI/CO)
           IF(PHASE.LT.O.) PHASE=PHASE+180.
           ADB=20.*ALOG10(MAG)+50.
           EAV=10.*(VMEAS+VBI)/XO
           WRITE(7,63)
63         FORMAT('0','VBIAS(V)  L(UM)   <E>(KV/CM)  MAG(LIN)  MAG(DB)',
     X     '  PHASE(DEG)')
           WRITE(7,64) VMEAS,XO,EAV,MAG,ADB,PHASE
64         FORMAT(' ',F6.2,F9.3,F10.2,F11.4,F9.2,F11.2)
           GO TO 6
C
22         CONTINUE
           STOP
           END
```

Sample Data

```
.RUN E
ENTER RELATIVE DIELECTRIC CONSTANT (SI=11.8, GAAS=13.1)
11.8
ENTER FREQUENCY (GHZ)
10.6
ENTER DX (UM)
.02
ENTER BUILT-IN VOLTAGE (V)
0.73
TYPE 1 TO PRINT E(X), O TO SKIP
1

ENTER VBIAS,X(UM),N(CM-3)
10.0,10.20,10.0E14
         BIAS VOLTAGE= 10.00 VOLTS
         INTEGRAL OF E(X)= 11.77 VOLTS
         X(UM)     E(KV/CM)
         0.000      19.510
         1.000      17.976
         2.000      16.442
         2.200      15.982
         2.600      14.969
         3.000      14.282
         3.500      13.641
         4.000      13.101
         4.500      12.564
         5.000      11.943
         5.500      11.195
```

```
6.000      10.343
6.500       9.434
7.000       8.606
7.500       7.977
8.000       7.448
8.500       6.857
9.000       6.075
9.200       5.653
9.400       5.116
9.600       4.433
9.800       3.482
10.000      2.148
10.100      1.266
10.200      0.000
```

CORRECTED E-FIELD PROFILE

```
BIAS VOLTAGE= 10.00 VOLTS
INTEGRAL OF E(X)= 10.74 VOLTS
X(UM)      E(KV/CM)
0.000      18.493
1.000      16.959
2.000      15.425
2.200      14.965
2.600      13.952
3.000      13.265
3.500      12.625
4.000      12.084
4.500      11.547
5.000      10.926
5.500      10.178
6.000       9.326
6.500       8.418
7.000       7.589
7.500       6.960
8.000       6.431
8.500       5.840
9.000       5.058
9.200       4.636
9.400       4.099
9.600       3.417
9.800       2.465
10.000      1.131
10.100      0.249
10.200      0.000
```

VBIAS(V)	L(UM)	<E>(KV/CM)	MAG(LIN)	MAG(DB)	PHASE(DEG)
10.00	10.200	10.52	0.0694	26.83	91.83

A.3 Program "BEAM"

```
C       ****************** PROGRAM BEAM ********************
C
C       THIS PROGRAM COMPUTES THE INCIDENT BEAM CURRENT AS A
C       FUNCTION OF TIME WHEN A GAUSSIAN ELECTRON BEAM IS SWEPT
C       OVER A CIRCULAR SAMPLE.  THE BEAM CENTER IS GIVEN BY
C       Y=0, Z=-ACOS(WT).
C
        REAL IY,IZ,IO
C
C       ENTER INPUT PARAMETERS
        WRITE(7,10)
10      FORMAT(' ENTER TIME STEP (PSEC)')
        READ(5,*) DELT
        WRITE(7,11)
11      FORMAT(' ENTER INCREMENT IN Y AND Z (.001 INCH)')
        READ(5,*) DEL
        WRITE(7,12)
12      FORMAT(' ENTER SIGMA OF BEAM (.001 INCH)')
        READ(5,*) SIGMA
        WRITE(7,13)
13      FORMAT(' ENTER SAMPLE RADIUS (.001 INCH)')
        READ(5,*) R
        WRITE(7,14)
14      FORMAT(' ENTER AMPLITUDE OF BEAM MODULATION (.001 INCH)')
        READ(5,*) A
        WRITE(7,15)
15      FORMAT(' ENTER Z-COORDINATE OF SAMPLE CENTER (.001 INCH)')
        READ(5,*) H
        WRITE(7,16)
16      FORMAT(' ENTER FREQUENCY (HZ)')
        READ(5,*) FREQ
        WRITE(7,17)
17      FORMAT(' ENTER TOTAL BEAM CURRENT (UA)')
        READ(5,*) IO
C
        W=FREQ*6.2832E-12
        C=-1./(2.*SIGMA*SIGMA)
        R2=R*R
        T=0.0
        WRITE(7,18)
18      FORMAT('0',2X,'TIME(PSEC)    CURRENT(UA)')
C
C       EVALUATE INTEGRAL
1       SUM=0.0
        Y=0.0
        U=-A*COS(W*T)
C
2       IY=EXP(Y*Y*C)
        D=SQRT(R2-Y*Y)
        Z=H-D
C
3       IZ=EXP(ABS(Z-U)**2.*C)
        SUM=SUM+IY*IZ
        Z=Z+DEL
        IF(Z.LT.H+D) GO TO 3
C
        Y=Y+DEL
        IF(Y.LT.R) GO TO 2
C
        SUM=IO*SUM*DEL*DEL*(-C)/3.14159
        WRITE(7,19) T,SUM
19      FORMAT(' ',F9.2,E16.4)
        IF(T.EQ.0.0) STORE=SUM
        T=T+DELT
        IF((W*T).LT.6.2832) GO TO 1
C
        PER=1.E12/FREQ
        WRITE(7,19) PER,STORE
        STOP
        END
```

Sample Data

```
.RUN BEAM
ENTER TIME STEP (PSEC)
5.0
ENTER INCREMENT IN Y AND Z (.001 INCH)
.05
ENTER SIGMA OF BEAM (.001 INCH)
13.86
ENTER SAMPLE RADIUS (.001 INCH)
5.0
ENTER AMPLITUDE OF BEAM MODULATION (.001 INCH)
35.0
ENTER Z-COORDINATE OF SAMPLE CENTER (.001 INCH)
35.0
ENTER FREQUENCY (HZ)
5.3E9
ENTER TOTAL BEAM CURRENT (UA)
10.0

   TIME(PSEC)    CURRENT(UA)
      0.00       0.1362E-05
      5.00       0.1615E-05
     10.00       0.2664E-05
     15.00       0.5903E-05
     20.00       0.1666E-04
     25.00       0.5601E-04
     30.00       0.2078E-03
     35.00       0.7877E-03
     40.00       0.2840E-02
     45.00       0.9164E-02
     50.00       0.2530E-01
     55.00       0.5818E-01
     60.00       0.1105E+00
     65.00       0.1749E+00
     70.00       0.2361E+00
     75.00       0.2810E+00
     80.00       0.3059E+00
     85.00       0.3157E+00
     90.00       0.3178E+00
     95.00       0.3179E+00
    100.00       0.3176E+00
    105.00       0.3142E+00
    110.00       0.3011E+00
    115.00       0.2711E+00
    120.00       0.2211E+00
    125.00       0.1575E+00
    130.00       0.9498E-01
    135.00       0.4756E-01
    140.00       0.1968E-01
    145.00       0.6816E-02
    150.00       0.2041E-02
    155.00       0.5550E-03
    160.00       0.1462E-03
    165.00       0.4014E-04
    170.00       0.1242E-04
    175.00       0.4661E-05
    180.00       0.2264E-05
    185.00       0.1494E-05
    188.68       0.1362E-05
STOP --
```

A.4. Program "EXPT"

In this section we describe the computer program used to simulate carrier motion across a sample due to the mechanisms of drift and diffusion for constant drift velocity v and diffusivity D. An explicit scheme is employed, wherein Equation (2.43) becomes

$$n_j^{t+\Delta t} = n_j^t - \frac{\Delta t}{2\Delta x} v(n_{j+1}^t - n_{j-1}^t)$$

$$+ \frac{\Delta t}{(\Delta x)^2} D(n_{j+1}^t + n_{j+1}^t + n_{j-1}^t - 2n_j^t). \tag{A.4.1}$$

The simulation will be unstable if a carrier is allowed to travel a distance greater than one mesh spacing Δx in a single time increment Δt. This is stated mathematically as

$$v + D \max \left(\frac{1}{n(x)} \frac{dn(x)}{dx}\right) \geq \frac{\Delta x}{\Delta t}. \tag{A.4.2}$$

For the typical values $\Delta x = 0.02$ μm and $\Delta t = 0.02$ psec, the simulation will be stable for the carrier spatial distributions of this experiment for diffusivity $D \leq 50$ cm^2/sec, provided the drift velocity is at least 0.2×10^7 cm/sec.

"Pseudodiffusion" is a numerically induced packet spreading which originates due to the truncation errors introduced by (A.4.1)[119]. It has no physical basis. When dn/dx is evaluated using a backward-difference

method, the pseudodiffusion coefficient D_p is given by

$$D_p = \frac{1}{2} (v\Delta x - v^2 \Delta t). \qquad (A.4.3)$$

This artificial spreading can be minimized by the choice of small values of Δx and Δt, but this conflicts with stability requirements, which dictate large Δx and small Δt. Boris et al.[120,121] have successfully removed this effect by applying an antidiffusion flux.

For center-difference evaluation of dn/dx, as is our case, the pseudodiffusion coefficient can be shown to be

$$D_p = -\frac{1}{2} v^2 \Delta t. \qquad (A.4.4)$$

For example, if $\Delta t = 0.05$ psec and $v = 1.0 \times 10^7$ cm/sec, D_p is equal to -5 cm^2/sec, comparable in magnitude to real semiconductor diffusivities. In this case, pseudodiffusion is minimized either by taking Δt small or adding $-D_p$ to the diffusivity D in Equation (A.3.1). The present simulation employs the latter method, although in practice small Δt is necessary to improve stability.

The incident electron current at time t_o must be chosen to satisfy

$$\frac{dF(t)}{dt}\bigg|_{t_o} = 0 \qquad\qquad\qquad (A.4.5)$$

and the initial carrier concentration is thus

$$n(x,t_o) = \frac{F(t_o)}{qv} \quad . \qquad\qquad\qquad (A.4.6)$$

These conditions must be satisfied for the simulation to "start up" properly. Also, calculations should progress until the terminal current becomes periodic, i.e. $K(t + T) = K(t)$, typically one or two cycles longer than the expected carrier transit time.

A program listing and sample output follow:

```
C        ******************** PROGRAM EXPT ********************
C
         REAL N(501),NN(501),K(50),NO,L,MULT
         DIMENSION F(50),T(50),T4(50)
         DIMENSION VV(20)
         DOUBLE PRECISION T1,T2,DT
C
C        ENTER INPUT PARAMETERS
         WRITE(7,30)
30       FORMAT(' ENTER DX (UM)')
         READ(5,*) DX
         WRITE(7,31)
31       FORMAT(' ENTER SAMPLE LENGTH L (UM)')
         READ(5,*) L
         WRITE(7,32)
32       FORMAT(' ENTER DT (PSEC)')
         READ(5,*) DT
         WRITE(7,33)
33       FORMAT(' TYPE 1 IF FREQUENCY= 5.3 GHZ'//' ',5X,
      X  '2 IF FREQUENCY=10.6 GHZ')
         READ(5,*) IFREQ
         WRITE(7,34)
34       FORMAT(' ENTER NUMBER OF CYCLES')
         READ(5,*) NC
         WRITE(7,35)
35       FORMAT(' ENTER DESIRED # OF HARMONICS (10 MAX)')
         READ(5,*) NH
         WRITE(7,36)
36       FORMAT(' ENTER MULTIPLICATION')
         READ(5,*) MULT
         WRITE(7,37)
37       FORMAT(' ENTER # OF VELOCITIES')
         READ(5,*) NVEL
         WRITE(7,50)
50       FORMAT(' ENTER VELOCITY IN CM/SEC (1 PER LINE)')
         DO 60 I=1,NVEL
         READ(5,*) VV(I)
60       CONTINUE
         WRITE(7,38)
38       FORMAT(' ENTER DIFFUSION CONSTANT D (CM**2/SEC)')
         READ(5,*) DD
C
C        READ NDATA FROM APPROPRIATE FILE
         OPEN(UNIT=15,NAME='DX1:DATA1.DAT',TYPE='OLD')
         OPEN(UNIT=16,NAME='DX1:DATA2.DAT',TYPE='OLD')
         IF(IFREQ.EQ.1) READ(15,*) NDATA
         IF(IFREQ.EQ.2) READ(16,*) NDATA
C
C        READ INCIDENT BEAM CURRENT FROM APPROPRIATE FILE
         DO 1 I=1,NDATA
         IF(IFREQ.EQ.1) READ(15,*) T(I),F(I)
         IF(IFREQ.EQ.2) READ(16,*) T(I),F(I)
1        CONTINUE
C
C        FOURIER ANALYZE INCIDENT BEAM CURRENT
         WRITE(7,39)
39       FORMAT('0','FOURIER ANALYSIS OF INCIDENT BEAM CURRENT')
         CALL FA(NDATA,T,F,NH)
C
         WRITE(7,40)
40       FORMAT('0'//'0','TERMINAL CURRENT K')
         M=INT(L/DX+.5)+1
         NP=INT(5./(FLOAT(IFREQ)*DT)+.5)
         MM=M-1
         PER=188.68/FLOAT(IFREQ)
C
         DO 61 II=1,NVEL
         V=VV(II)
         D=DD+.5E-12*DT*V*V
         A=1.0E-8*V*DT/(2.*DX)
         B=1.0E-4*D*DT/(DX*DX)
         T1=0.0
         T2=0.0
         N3=-1
```

```
          J=1
          JJ=1
          T4(1)=0.0
          K(1)=MULT*F(1)
          NO=K(1)/V
          NCC=1
C
C         INITIALIZE N(I)
          DO 2 I=1,M
          N(I)=NO
2         CONTINUE
C
3         WRITE(7,41) NCC
41        FORMAT('0','CYCLE #',I1)
          WRITE(7,42)
42        FORMAT('0',2X,'TIME(PSEC)',6X,'K(UA)')
          WRITE(7,43) T4(1),K(1)
43        FORMAT(' ',F9.2,E15.4)
C
C         SEARCH FOR INCIDENT BEAM CURRENT AT TIME T2
4         CONTINUE
          IF(T2.LT.PER) GO TO 5
          T2=T2-PER
          J=1
5         IF(T2.GT.T(J+1)) J=J+1
          NN(1)=MULT*(F(J)+(T2-T(J))*(F(J+1)-F(J))/(T(J+1)-T(J)))/V
C
C         COMPUTE N(T+DT)
          DO 6 I=2,MM
          NN(I)=N(I)-A*(N(I+1)-N(I-1))+B*(N(I+1)+N(I-1)-2.*N(I))
          IF(NN(I).LT.0.0) NN(I)=0.0
6         CONTINUE
C
          NN(M)=N(M)-2.*A*(N(M)-N(M-1))
          IF(NN(M).LT.0.0) NN(M)=0.0
C
C         STORE NN
          DO 7 I=1,M
          N(I)=NN(I)
7         CONTINUE
C
C         INCREMENT TIME
          T1=T1+DT
          IF(T1-DT.GT.PER) GO TO 8
          T2=T2+DT
          N3=N3+1
          IF(N3.LT.NP) GO TO 4
C
C         INTEGRATE CURRENT J OVER SAMPLE LENGTH
8         JJ=JJ+1
          SUM=.5*V*N(1)
          DO 9 I=2,MM
          SUM=SUM+N(I)*V-1.0E4*D*(N(I)-N(I-1))/DX
9         CONTINUE
C
          SUM=SUM+.5*(N(M)*V-1.0E4*D*(N(M)-N(MM))/DX)
          K(JJ)=SUM*DX/L
          T4(JJ)=T1-DT
          WRITE(7,43) T4(JJ),K(JJ)
          N3=0
          IF(PER.GT.T1) GO TO 4
C
C         FOURIER ANALYZE TERMINAL CURRENT
          WRITE(7,44) NCC
44        FORMAT('0','FOURIER ANALYSIS OF CYCLE #',I1)
          CALL FA(JJ,T4,K,NH)
          NCC=NCC+1
          IF(NCC.GT.NC) GO TO 10
          K(1)=K(JJ)
          JJ=1
          N3=-1
          T1=0.0
          GO TO 3
C
10        CONTINUE
61        CONTINUE
          STOP
          END
```

```fortran
        SUBROUTINE FA(N,TT,F,NH)
C
C       THIS SUBROUTINE FOURIER ANALYZES A WAVEFORM WHERE
C               N = # OF DATA POINTS
C               TT = VECTOR OF TIMES (PSEC)
C               F = VECTOR OF FUNCTION VALUES
C               NH = # OF HARMONICS
C
        REAL NWT1,NWT2
        DIMENSION TT(100),T(100),F(100),AA(10),BB(10)
C
        DO 1 I=1,N
        T(I)=TT(I)*1.0E-12
1       CONTINUE
C
        FREQ=1.0/T(N)
        W=6.2832*FREQ
        A0=0.0
C
        DO 2 I=1,NH
        AA(I)=0.0
        BB(I)=0.0
2       CONTINUE
C
        DO 4 J=2,N
        A0=A0+.5*(F(J-1)+F(J))*(T(J)-T(J-1))
        B=(F(J)-F(J-1))/(T(J)-T(J-1))
        A=F(J-1)-B*T(J-1)
C
        DO 3 K=1,NH
        HN=FLOAT(K)
        E=1./(HN*W)
        NWT1=HN*W*T(J-1)
        NWT2=HN*W*T(J)
        D1=E*(A+B*T(J))*SIN(NWT2)
        D2=E*E*B*COS(NWT2)
        D3=E*(A+B*T(J-1))*SIN(NWT1)
        D4=E*E*B*COS(NWT1)
        E1=-E*(A+B*T(J))*COS(NWT2)
        E2=E*E*B*SIN(NWT2)
        E3=-E*(A+B*T(J-1))*COS(NWT1)
        E4=E*E*B*SIN(NWT1)
        AA(K)=AA(K)+D1+D2-D3-D4
        BB(K)=BB(K)+E1+E2-E3-E4
3       CONTINUE
4       CONTINUE
C
        CO=A0/T(N)
        WRITE(7,10)
10      FORMAT('0',2X,'FREQ(GHZ)',4X,'MAG(UA)',4X,'PHASE(DEG)')
        WRITE(7,11) CO
11      FORMAT(' ',5X,'DC',E16.4)
C
        DO 5 I=1,NH
        AA(I)=(2./T(N))*AA(I)
        BB(I)=(2./T(N))*BB(I)
        C=(AA(I)*AA(I)+BB(I)*BB(I))**0.5
        PH=57.296*ATAN(BB(I)/AA(I))
        IF(AA(I).LT.0.0.AND.BB(I).GT.0.0) PH=PH+180.0
        IF(AA(I).LT.0.0.AND.BB(I).LT.0.0) PH=PH-180.0
        FN=1.0E-9*FLOAT(I)*FREQ
        WRITE(7,12) FN,C,PH
12      FORMAT(' ',F8.1,E15.4,F11.3)
5       CONTINUE
C
        RETURN
        END
```

Sample Data

```
.RUN EXPT
ENTER DX (UM)
.02
ENTER SAMPLE LENGTH L (UM)
1.00
ENTER DT (PSEC)
.02
TYPE 1 IF FREQUENCY= 5.3 GHZ
     2 IF FREQUENCY=10.6 GHZ
2
ENTER NUMBER OF CYCLES
2
ENTER DESIRED # OF HARMONICS (10 MAX)
5
ENTER MULTIPLICATION
100
ENTER # OF VELOCITIES
1
ENTER VELOCITY IN CM/SEC (1 PER LINE)
1.0E7
ENTER DIFFUSION CONSTANT D (CM**2/SEC)
20.0
```

FOURIER ANALYSIS OF INCIDENT BEAM CURRENT

FREQ(GHZ)	MAG(UA)	PHASE(DEG)
DC	0.1148E+00	
10.6	0.1390E+00	179.942
21.2	0.4863E-01	-0.070
31.8	0.1179E-01	179.883
42.4	0.2172E-02	0.140
53.0	0.3190E-03	179.363

TERMINAL CURRENT K

CYCLE #1

TIME(PSEC)	K(UA)
0.00	0.1454E+01
2.50	0.1459E+01
5.00	0.1483E+01
7.50	0.1544E+01
10.00	0.1662E+01
12.50	0.1859E+01
15.00	0.2158E+01
17.50	0.2590E+01
20.00	0.3193E+01
22.50	0.4019E+01
25.00	0.5128E+01
27.50	0.6588E+01
30.00	0.8458E+01
32.50	0.1078E+02
35.00	0.1355E+02
37.50	0.1670E+02
40.00	0.2007E+02
42.50	0.2343E+02
45.00	0.2647E+02
47.50	0.2885E+02
50.00	0.3029E+02
52.50	0.3059E+02
55.00	0.2973E+02
57.50	0.2782E+02
60.00	0.2510E+02
62.50	0.2189E+02
65.00	0.1850E+02

```
67.50        0.1523E+02
70.00        0.1225E+02
72.50        0.9696E+01
75.00        0.7587E+01
77.50        0.5909E+01
80.00        0.4613E+01
82.50        0.3635E+01
85.00        0.2911E+01
87.50        0.2386E+01
90.00        0.2014E+01
92.50        0.1761E+01
94.34        0.1636E+01
```

FOURIER ANALYSIS OF CYCLE #1

FREQ(GHZ)	MAG(UA)	PHASE(DEG)
DC	0.1147E+02	
10.6	0.1356E+02	-161.815
21.2	0.4387E+01	36.251
31.8	0.9465E+00	-126.581
42.4	0.1363E+00	73.218
53.0	0.2345E-01	-110.305

CYCLE #2

TIME(PSEC)	K(UA)
0.00	0.1636E+01
2.50	0.1536E+01
5.00	0.1509E+01
7.50	0.1550E+01
10.00	0.1663E+01
12.50	0.1859E+01
15.00	0.2158E+01
17.50	0.2590E+01
20.00	0.3193E+01
22.50	0.4019E+01
25.00	0.5128E+01
27.50	0.6588E+01
30.00	0.8458E+01
32.50	0.1078E+02
35.00	0.1355E+02
37.50	0.1670E+02
40.00	0.2007E+02
42.50	0.2343E+02
45.00	0.2647E+02
47.50	0.2885E+02
50.00	0.3029E+02
52.50	0.3059E+02
55.00	0.2973E+02
57.50	0.2782E+02
60.00	0.2510E+02
62.50	0.2189E+02
65.00	0.1850E+02
67.50	0.1523E+02
70.00	0.1225E+02
72.50	0.9696E+01
75.00	0.7587E+01
77.50	0.5909E+01
80.00	0.4613E+01
82.50	0.3635E+01
85.00	0.2911E+01
87.50	0.2386E+01
90.00	0.2014E+01
92.50	0.1761E+01
94.34	0.1636E+01

FOURIER ANALYSIS OF CYCLE #2

FREQ(GHZ)	MAG(UA)	PHASE(DEG)
DC	0.1148E+02	
10.6	0.1355E+02	-161.808
21.2	0.4397E+01	36.207
31.8	0.9378E+00	-126.295
42.4	0.1435E+00	70.795
53.0	0.1645E-01	-94.941

STOP --

APPENDIX B

SAMPLE PROCESSING

B.1. <u>n-type GaAs Samples</u>

1. Clean wafer with FL-70 soap and soft bristle brush in ultrasonic.

2. Standard clean wafer (acetone, methanol, DI water).

3. Evaporate 2000 $\overset{o}{A}$ AuGe on backside.

4. Alloy ohmic contact 2 minutes at 400°C.

5. If epilayer is not to be thinned, go to step 13.

6. Brush Shipley AZ-1350B photoresist on backside.

7. Bake 110°C for 40 minutes.

8. Etch in 5:1:1 $H_2SO_4:H_2O_2(30\%):H_2O$ (etch rate is $\approx$ 1.3 $\mu m/min.$)

9. Quench in 5:2 $H_2SO_4:H_2O$.

10. Rinse in DI.

11. Standard clean.

12. Bake 15 minutes at 150°C.

13. Spin on AZ-1350J photoresist 15 seconds at 2500 rpm.

14. Prebake 20 minutes at 80°C.

15. Expose through mask #1 for 15 seconds in Optometric contact mask aligner.

16. Develop 1 minute in 1:10 solution AZ-606 developer:DI water.

17. Rinse in DI water, blow dry.

AFTER STEP
#16

20

21

27

29

30
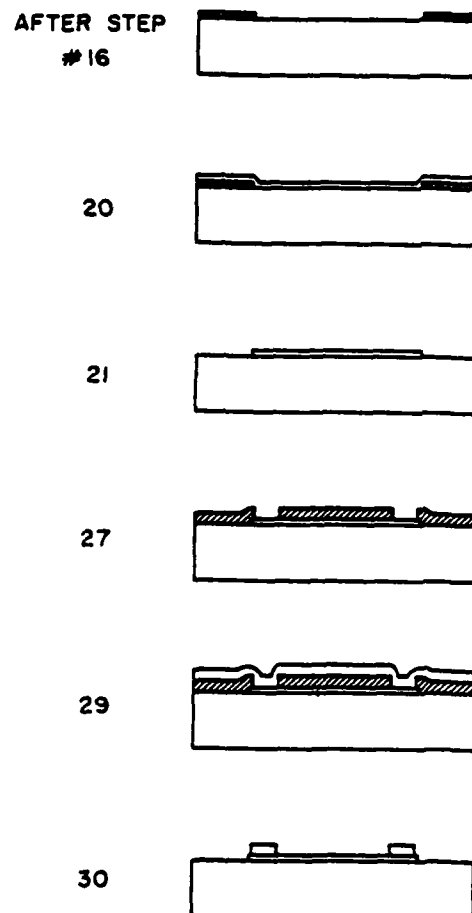
Figure B.1. Cross-sectional view of n-GaAs sample after
various steps of the fabrication process.

18. Etch 30 seconds in 400:8:3 $H_2O:NH_4OH(58\%):H_2O_2(30\%)$ (etch rate is 2000 Å/min).

19. Rinse in DI water, blow dry.

20. Immediately evaporate 200 Å Cr.

21. Liftoff in acetone.

22. Standard clean.

23. Bake 15 minutes at 150°C.

24. Spin on AZ 1350J photoresist 10 seconds at 1500 rpm.

25. Prebake 20 minutes at 80°C.

26. Expose through mask #2 for 30 seconds.

27. Develop 1 minute in 1:10 AZ-606 developer:DI water.

28. Rinse in DI water, blow dry.

29. Evaporate 100 Å Cr, 2500 Å Au.

30. Liftoff in acetone with ultrasonic.

31. Standard clean, blow dry.

B.2. <u>Si Samples (Both n- and p-Type)</u>

1. Standard clean wafer.

2. Evaporate 2000 Å AuSb (n-Si), 2000 Å aluminum (p-Si) on backside.

3. Alloy ohmic contact: 500°C for 5 minutes (n-Si), 450°C for 10 minutes (p-Si).

4. Evaporate 100 ÅCr, 2000 Å Au on back side.

5. If epilayer is not to be thinned, go to step 9.

6. Etch in 50:1 $HNO_3:HF$ (etch rate $\approx$ 1.8 μm/min).

7. Rinse in DI, blow dry.
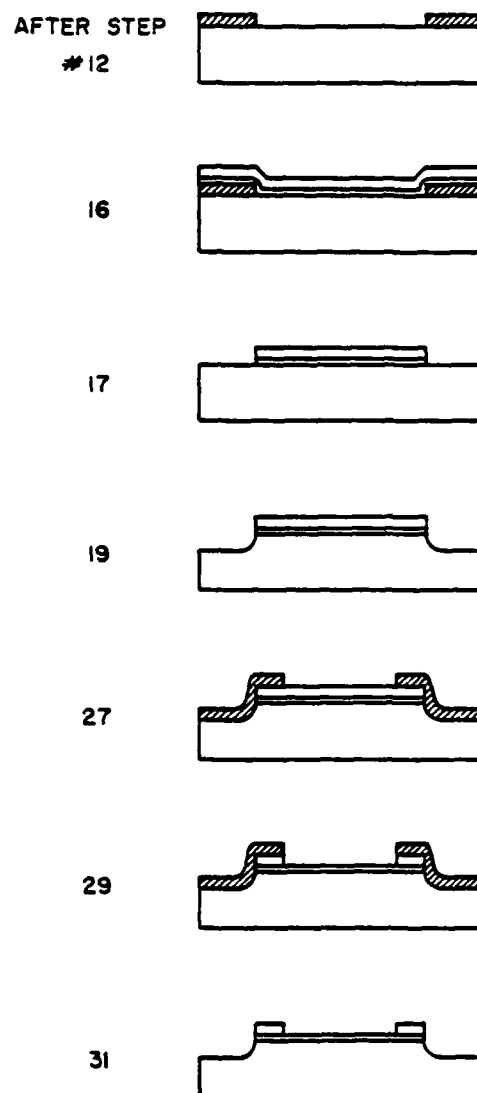
Figure B.2. Cross-sectional view of Si sample after various steps of the fabrication process.

8. Bake 15 minutes at 150°C.

9. Spin on AZ 1350J photoresist 15 seconds at 2500 rpm.

10. Prebake 20 minutes at 80°C.

11. Expose through mask #1 for 15 seconds.

12. Develop 1 minute in 1:10 AZ-606 developer: DI water.

13. Rinse in DI water, blow dry.

14. Dip into buffered HF.

15. Rinse in DI water, blow dry.

16. Immediately evaporate 200 $\overset{o}{A}$ Cr (n-Si), 100 $\overset{o}{A}$ Cr (p-Si), 2500 $\overset{o}{A}$ Au.

17. Liftoff in acetone with ultrasonic.

18. Standard clean.

19. Etch mesa of desired height in 30:1 HNO_3:HF (etch rate $\simeq$ 3 μm/min). Mesa height should be greater than epi-layer thickness.

20. Rinse in DI water, blow dry.

21. Remove overhanging metallization with 30 seconds ultrasonic in acetone.

22. Standard clean, blow dry.

23. Bake 15 minutes at 150°C.

24. Spin on AZ-1350J photoresist 10 seconds at 1500 rpm.

25. Prebake 20 minutes at 80°C.

26. Expose through mask #2 for 30 seconds.

27. Develop 1 minute in 1:10 AZ-606 developer:DI

water.

28. Rinse in DI water, blow dry.

29. Etch 90 seconds in Transene type TFA gold etchant (etch rate $\cong$ 1700 $\overset{o}{A}$/min).

30. Rinse in DI water, blow dry.

31. Standard clean, blow dry.

APPENDIX C

MICROWAVE C-V TECHNIQUE

Due to their low capacitances, microwave time-of-flight samples are profiled using a high frequency C-V technique[122] in which sample capacitance is derived from measurements of the diode reflection coefficient at 100 MHz.

Since sample capacitances can be as low as 1 pF, the maximum capacitive reactance at 100 MHz is 160 Ω, substantially smaller than the shunt resistance which is typically in the 10^6 to 10^7 Ω range. The magnitude of the reflection coefficient is therefore taken to be unity and the reflection coefficient phase is related to the capacitive reactance. The diode is located at the end of the center conductor of a coaxial transmission line, as shown in Figure C.1a. The equivalent circuit of this configuration appears in Figure C.1b.

It can be shown that the total capacitance

$$C_{total} \ (pF) \ = \ \frac{10^4}{\pi \ f \ (MHz)} \ \frac{sin|\theta|}{1+cos|\theta|} \tag{C.1}$$

where

$$C_{total} = C_{fringe} + C_{package} + substrate + C_{chip} \tag{C.2}$$
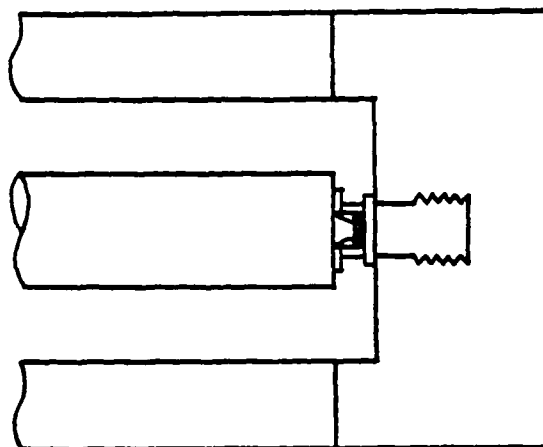
a) Experimental configuration
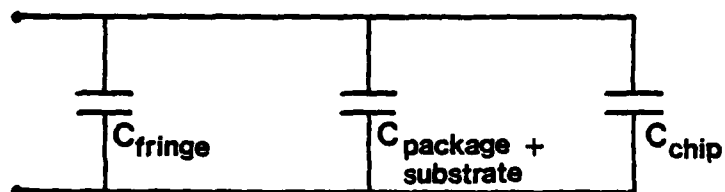
b) Equivalent circuit

Figure C.1. Microwave C-V technique. a) Experimental
configuration. b) Equivalent circuit for (a).

and θ is the phase of the reflection coefficient. In this work the phase was measured with an HP network analyzer system which consists of an 8410A network analyzer mainframe, 8413A phase-gain indicator, 8411A harmonic frequency converter, and 8745 low frequency S-parameter test set. A GR 1215-B oscillator provides the 100 MHz signal, its frequency being monitored with an HP 5381A frequency counter.

The system is first calibrated with an open circuit whose fringing capacitance is calculated to be 0.08 pF[123] (corresponding to $\theta = 0.29°$). The parasitic capacitance $(C_{fringe} + C_{package+substrate})$ is then determined from a measurement of θ for a package containing a diode without wires attached. The effect of the conducting substrate must be considered since it effectively raises the electrical height of the package pedestal with respect to the package lip. A typical measured value of parasitic capacitance, 0.41 pF, leads to a package plus substrate capacitance of 0.33 pF, slightly higher than the accepted value of capacitance for an empty package, 0.31 pF.[123]

Total capacitance as a function of sample bias is then derived from measurements of the reflection coefficient phase. The parasitic capacitance is subsequently subtracted from the total capacitance, leaving the chip capacitance. The depletion width as a function of bias voltage is given by

$$x(v) = \frac{\varepsilon a}{C_{chip}(V)} \tag{C.3}$$

where ε is the dielectric permittivity and a is the diode area. Carrier concentration is calculated according to[124]

$$n, p(V) = \frac{C(V)^3}{q\varepsilon a^2 \left|\frac{dC(V)}{dV}\right|} \tag{C.4}$$

Equation (C.4), which is based upon the depletion approximation, has been shown[125,126] to provide a reasonably accurate description of the majority carrier concentration, not the impurity profile. However, this data is subsequently used to compute electric field profiles via Poisson's equation, and it is in fact the majority carrier concentration which must be known.

The computer program which evaluates Equations (C.1)-(C.4) is listed below, along with a sample output. In order to estimate the accuracy of capacitance values obtained with the high-frequency C-V technique, thin samples having capacitances on the order of 10 pF were tested using both the 100 MHz and the conventional 1 MHz methods and results compared: measured capacitances were found to differ by less than 1%.

```
C         ********** PROGRAM MCV (MICROWAVE C-V) **********
C
          DIMENSION VOLTS(50),THETA(50),CCHIP(50),X(50)
C
C         ENTER EXPERIMENTAL PARAMETERS
          WRITE(7,10)
10        FORMAT(' ENTER RELATIVE DIELECTRIC CONSTANT (SI=11.8,GAAS=13.1)')
          READ(5,*) EPS
          WRITE(7,11)
11        FORMAT(' ENTER SAMPLE DIAMETER (UM)')
          READ(5,*) D
          WRITE(7,12)
12        FORMAT(' ENTER FREQUENCY (MHZ)')
          READ(5,*) F
          WRITE(7,13)
13        FORMAT(' ENTER PHASE OF EMPTY PACKAGE (DEGREES)')
          READ(5,*) PAR
C
          E=EPS*8.85E-12
          P=ABS(PAR)*2.*3.14159/360.
          CPAR=(1.0E4/(3.14159*F))*SIN(P)/(1.+COS(P))
          A=3.14159*1.0E-12*D*D/4.0
C
C         READ MEASURED DATA FROM FILE
          OPEN(UNIT=15,NAME='DX1:CV.DAT',TYPE='OLD')
          I=0
1         I=I+1
          READ(15,*) VOLTS(I),THETA(I)
          IF(THETA(I).EQ.0.0) GO TO 2
          GO TO 1
C
2         WRITE(7,14)
14        FORMAT('0',8X,'VOLT',3X,'THETA',5X,'C(PF)',4X,'1/C2(10**22)',
     X    3X,'X(UM)')
C
C         CALCULATE CHIP CAPACITANCE, DEPLETION WIDTH
          N=I-1
          DO 3 J=1,N
          RAD=ABS(THETA(J))*2.*3.14159/360.
          CTOTL=(1.0E4/(3.14159*F))*SIN(RAD)/(1.+COS(RAD))
          CCHIP(J)=CTOTL-CPAR
          C2=100./(CCHIP(J)*CCHIP(J))
          X(J)=E*A*1.0E18/CCHIP(J)
          WRITE(7,15) VOLTS(J),THETA(J),CCHIP(J),C2,X(J)
15        FORMAT(' ',F12.3,F7.1,F10.3,F12.3,F12.3)
3         CONTINUE
C
          WRITE(7,16)
16        FORMAT('0',8X,'X(UM)',5X,'N(CM-3)')
C
C         CALCULATE DOPING
          N=I-2
          DO 4 J=1,N
          DELV=VOLTS(J)-VOLTS(J+1)
          DELC=CCHIP(J+1)-CCHIP(J)
          C=(CCHIP(J)+CCHIP(J+1))/2.
          DOPE=ABS(C**3*DELV*.625E-11/(A*A*E*DELC))
          X1=(X(J)+X(J+1))/2.
          WRITE(7,17) X1,DOPE
17        FORMAT(' ',7X,F6.3,E13.4)
4         CONTINUE
C
          WRITE(7,18) CPAR
18        FORMAT('0',8X,'PARASITIC CAPACITANCE=',F6.3,' PF')
          STOP
          END
```

```
RUN MCV
ENTER RELATIVE DIELECTRIC CONSTANT (SI=11.8,GAAS=13.1)
11.8
ENTER SAMPLE DIAMETER (UM)
367.0
ENTER FREQUENCY (MHZ)
98.6
ENTER PHASE OF EMPTY PACKAGE (DEGREES)
1.45
```

VOLT	THETA	C(PF)	1/C2(10**22)	X(UM)
16.600	5.8	1.241	64.933	8.902
7.490	6.0	1.283	60.716	8.608
4.100	7.0	1.566	40.778	7.054
2.960	8.0	1.849	29.252	5.975
2.120	9.0	2.132	21.996	5.181
1.610	10.0	2.416	17.134	4.573
1.305	11.0	2.700	13.718	4.092
1.070	12.0	2.985	11.226	3.701
0.912	13.0	3.270	9.354	3.379
0.792	14.0	3.555	7.911	3.107
0.614	16.0	4.129	5.867	2.676
0.485	18.0	4.705	4.518	2.348
0.385	20.0	5.284	3.582	2.091
0.299	22.0	5.867	2.905	1.883
0.225	24.0	6.453	2.401	1.712
0.158	26.0	7.045	2.015	1.568
0.100	28.0	7.641	1.713	1.446
0.045	30.0	8.242	1.472	1.340
0.000	31.9	8.818	1.286	1.253
-0.053	34.0	9.461	1.117	1.168
-0.099	36.0	10.081	0.984	1.096
-0.141	38.0	10.707	0.872	1.032
-0.181	40.0	11.342	0.777	0.974
-0.219	42.0	11.984	0.696	0.922
-0.270	45.0	12.964	0.595	0.852
-0.315	48.0	13.965	0.513	0.791
-0.351	51.0	14.990	0.445	0.737
-0.379	54.0	16.040	0.389	0.689
-0.400	57.0	17.120	0.341	0.645
-0.414	60.0	18.230	0.301	0.606
-0.424	63.0	19.374	0.266	0.570
-0.432	66.0	20.556	0.237	0.537

X(UM)	N(CM-3)
8.755	0.2312E+16
7.831	0.1855E+15
6.515	0.1073E+15
5.578	0.1251E+15
4.877	0.1131E+15
4.332	0.9609E+14
3.896	0.1014E+15
3.540	0.9063E+14
3.243	0.8928E+14
2.891	0.9418E+14
2.512	0.1032E+15
2.219	0.1150E+15
1.987	0.1368E+15
1.797	0.1577E+15
1.640	0.1863E+15
1.507	0.2061E+15
1.393	0.2450E+15
1.297	0.2592E+15
1.210	0.3364E+15
1.132	0.3705E+15
1.064	0.4026E+15
1.003	0.4520E+15
0.948	0.5020E+15
0.887	0.5403E+15
0.822	0.5867E+15
0.764	0.5700E+15
0.713	0.5322E+15
0.667	0.4743E+15
0.626	0.3723E+15
0.588	0.3106E+15
0.554	0.2881E+15

```
          PARASITIC CAPACITANCE= 0.409 PF
STOP --
```

APPENDIX D

MEASUREMENT OF BEAM PROPERTIES

Beam properties, such as spot size and deflection sensitivity, are determined from simple experiments in which either x or y deflection is used to move the beam over a partially blocking structure (i.e. step or slit) while the beam current, collected with a Faraday cup, is monitored.

One such method is illustrated in Figure D.1a. In this case, only beam current falling within the half plane defined by $x > 0$ is collected. The collected current is measured as the x-coordinate of the beam center, a, is varied by changing voltages applied to the x-deflection plates. Clearly, when $a = 0$ exactly one half of a symmetric beam will be collected. Furthermore, the rate at which the collected current rises as a increases will vary with beams of different size.

If a Gaussian beam is assumed, its density can be written as

$$\rho(x,y) = \frac{I_o}{2\pi\sigma^2} e^{-(x^2+y^2)/2\sigma^2} \qquad (D.1)$$

where I_o is the total beam current and σ is defined as the square root of the variance, and is also known as the half-width. When a Gaussian beam is swept across a

228
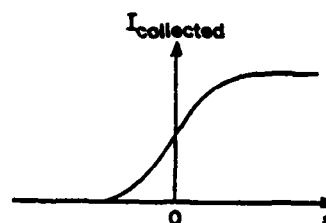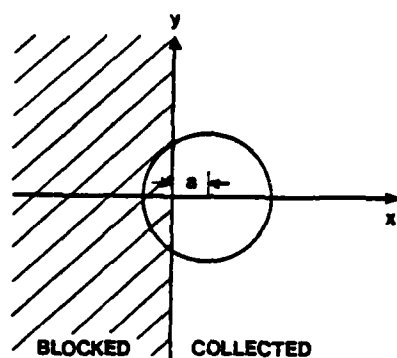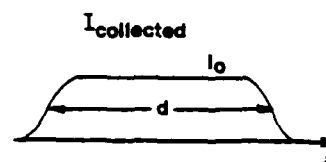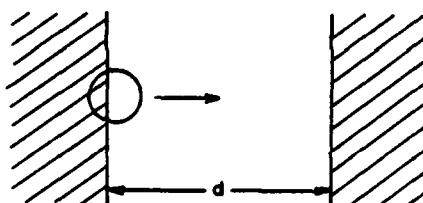
a) Step

b) Slit

Figure D.1. Test configurations for beam profiling and
X-Y deflection system calibration. a) Step used to
profile beam. b) Slit used to calibrate X-Y deflection.

step as in Figure D.1a, collected current is given by

$$I_{coll} = I_0 \left(\frac{1}{2} + \int_0^a \int_{-\infty}^{\infty} \rho (x,y) dy dx\right) \tag{D.2}$$

Integrating over y and performing a change of variables, we obtain

$$I_{coll} = I_0 \left(\frac{1}{2} + \frac{1}{2} \int_0^{\frac{a}{\sqrt{2}\sigma}} e^{-t^2} dt\right). \tag{D.3}$$

Values for the integral in Equation (D.3) have been tabulated,[127] allowing evaluation of collected beam current as a function of beam position a. The resulting curve is plotted in Figure D.2. For a half-width σ of 0.011 inches, the theoretical curve fits the experimental one over the entire experimental range, indicating that our assumption of a Gaussian beam is correct. It should be pointed out that the calculated curve of Figure D.2 is unique, i.e. no other radially symmetric beam intensity distribution will have the same collected current versus beam position characteristic.

Since the beam has been shown to be Gaussian, σ is simply equal to the value of a at which

$$\frac{I_{coll}}{I_0} = \frac{1}{2} + \frac{1}{2} \int_0^{\frac{1}{\sqrt{2}}} e^{-t^2} dt = 0.731 \tag{D.4}$$

Both x and y deflection settings must be calibrated
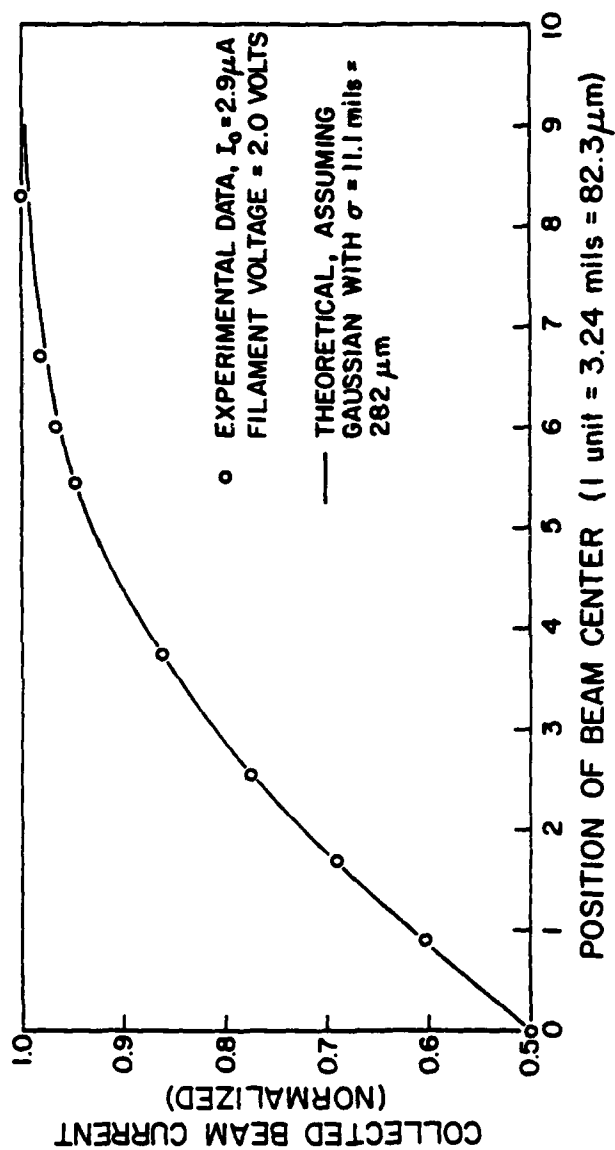
Figure D.2. Comparison of measured and calculated collected beam current as a function of beam position.

to allow determination of actual physical lengths in the sample plane. This is accomplished with a slit of known width considerably larger than the beam size. As shown in Figure D.1b, the slit is aligned perpendicular to the axis under calibration. The setting of the potentiometer controlling the deflection must be changed by a certain number of divisions to move the beam across the slit. Since the collected current is equal to half of the total current when the beam center coincides with either side of the slit, and the distance between these half current points is known, the physical distance corresponding to a single division can be found. The following results were obtained:

x   1.62 mils/division

y   1.91 mils/division

It is important to note that these calibrations are necessary for the beam half-width to be determined, and they allow the beam axis and sample center to be offset by a known distance, as is the case when the experiment is performed at 5.3 GHz.

APPENDIX E

MEASUREMENT SEQUENCE

Preparations: (These steps performed before <u>any</u> measurement)

1. Warm up the following equipment for the specified time:

    Network analyzer (2 hours)

    5.3 GHz oscillator (2 hours)

    X-Y recorder (1 hour)

    e-gun high voltage supply (1/2 hour)

    e-gun x-y supply (1/2 hour)

    GaAs FET amplifier (1/2 hour)

2. Connect phosphor screen to system, following "sample change procedure" of Section 3.7.

3. Turn on e-gun cooling fan. Turn on e-gun filament and gradually increase filament voltage to 2.0 to 2.5 volts. Beam is now on.

4. Center beam visually with x-y positioning.

5. Adjust frequency of 5.3 GHz oscillator to give maximum amplitude of microwave modulation visible on phosphor screen. This will occur precisely at the cavity resonant frequency.

6. Gradually decrease filament voltage to zero and turn off. Beam is now off.

7. Install sample holder with sample into system, again following sample change procedure.

5.3 GHz Measurement

8. Connect bias tee, amplifier and harmonic frequency converter.

9. Adjust variable attenuator in reference line to give reference channel level in middle of "operate" range.

10. Apply small reverse bias to sample (typically 10% of breakdown voltage).

11. With beam off, turn microwave input to cavity on. 5.3 GHz test channel amplitude is monitored by phase-gain indicator on gain, 30 dB scale, and should be equal to system noise level when beam is off. If there is some 5.3 GHz signal, it is due to some of the power from the reference channel coupling into the input side of the amplifier, and can be eliminated by readjusting or tightening the connections. Isolation can also be improved by wrapping metal tape around these connections.

12. Turn off cavity input power, turn on beam (see step 3).

13. Center beam on sample by adjusting x and y positioning until DC sample current is maximized.

14. Turn on cavity input power.

15. Adjust x deflection for maximum amplitude of test signal as indicated by phase-gain

indicator. Note that there are two beam positions at which a maximum is obtained, given by $x = \pm$ h, and the phase of these two signals differs by exactly 180 degrees, as one would expect.

16. Vary bias smoothly from 0 volts to reverse breakdown (as evidenced by large dc current), recording 5.3 GHz phase or amplitude with x-y recorder.

10.6 GHz Measurements

17. Connect 10.6 GHz transmission cavity, frequency doubler diode and X-band slide screw tuner at appropriate locations.

18. Adjust variable attenuator and slide screw tuner to give acceptable reference channel power level.

19. Apply small reverse bias to sample.

20. Turn on beam (step 3) and center on sample by adjusting x and y positioning until dc sample current is maximized.

21. Turn on cavity input power, mechanically tune 10.6 GHz cavity for maximum transmission, i.e. maximum signal amplitude indicated by phase-gain indicator.

22. Adjust x and y deflection to maximize signal level. Note: since beam has already been centered, only slight adjustment will be

necessary here.

23. Vary bias smoothly from 0 volts to reverse
     breakdown, recording 10.6 GHz phase or
     amplitude.

APPENDIX F

ABSOLUTE MEASUREMENTS

Throughout Chapter 4 absolute values of velocity were determined from amplitude extrema according to

$$\frac{\omega \ell}{2v} = n\pi \qquad\qquad (4.14)$$

Only discrete points can be obtained in this manner with the present experiment. In order to obtain a number of absolute points evenly distributed over the field range through which a velocity-field curve can be reliably drawn, one must either vary the frequency or make measurements on many samples of different lengths.

In this experiment a narrow bandwidth cavity produced electron beam modulation at 5.3 GHz. A number of fixed frequency cavities could be used, but this would be impractical since each would in turn have to be inserted into the vacuum system and properly aligned. Alternatively, a meander line deflection structure[128] would allow the frequency to be tuned over a broad bandwidth, although the low Q of such a structure would necessitate large input power.

In our experiment thinner samples (i.e. less than 5 μm) had no observable amplitude extrema at 5.3 or 10.6 GHz since the first amplitude minimum was never reached, i.e.,

$$0 < \frac{\omega \ell}{2v} < \pi \quad . \tag{4.15}$$

In such cases measurements of higher harmonic components of the terminal current might provide absolute points, although in practice this may be difficult due to the low detected signal levels which at high frequencies will be diminished ever further by circuit effects, as discussed in Chapter 5.

In cases where no reference point can be found, an alternative method of arriving at absolute results is required. We present here both an analytical and an experimental technique which would allow absolute determination of velocity in the absence of amplitude extrema.

If velocity is taken to be constant with position and diffusion neglected, then the measured phase and amplitude at two different bias voltage (i.e. carrier velocities) are given by:

$$\phi_{m1} = \frac{\omega \ell}{2v_1} + \phi_o \tag{4.16}$$

$$\phi_{m2} = \frac{\omega \ell}{2v_2} + \phi_o \tag{4.17}$$

$$A_1 = A_o \frac{\sin \left(\frac{\omega \ell}{2v_1} \right)}{\frac{\omega \ell}{2v_1}} \tag{4.18}$$

$$A_2 = \frac{A_0 \sin\left(\frac{\omega \ell}{2v_2}\right)}{\frac{\omega \ell}{2v_2}} \qquad (4.19)$$

where ϕ_0 is a constant phase shift attributed to the experimental configuration and A_0 is another unknown constant. Equations (4.16)-(4.19) represent four nonlinear equations in four unknowns (v_1, v_2, ϕ_0 and A_0), for which a solution for v_2 is given by the transcendental equation

$$\sin(C_1)\cot\left(\frac{\omega \ell}{2v_2}\right) + \cos(C_1) - C_2 - \frac{2C_1 C_2 v_2}{\omega \ell} = 0 \qquad (4.20)$$

in which

$$C_1 = \phi_{m1} - \phi_{m2} \qquad (4.21)$$

$$C_2 = \frac{A_1}{A_2} \qquad (4.22)$$

For the solution to be well-conditioned, the phase difference C_1 must be appreciable and the ratio of amplitudes, C_2, must not be too close to unity. Also, this technique requires that the constant velocity assumption is valid and that the assumed amplitude dependence is not altered by phenomena such as noise.

Alternatively, the constant phase ϕ_0 inherent in the system may be determined experimentally. One can "calibrate" the system by first measuring the phase of the

signal detected when an empty package replaces the test diode in the sample holder. Since in this case there is no current multiplication, the signal is expected to be extremely small. Measurements verify this, yet the amplitude is still more than 14 dB above system noise.

The success of this technique hinges upon the requirement that experimental conditions be identical during measurements of both the empty package and the test sample. Due to the delay caused by changing samples, the two measurements must be made at least 20 minutes apart in the present experiment. Slight changes in various parameters such as electron gun accelerating potential and deflection oscillator frequency can produce significant phase shifts, as discussed in Chapter 5. Attempts were made to stabilize all important quantities, yet measured drift was still found to be unacceptably large.

It is believed that a modification of this technique in which both the sample and reference are fabricated on the same chip, and hence mounted in a single package, can produce meaningful results. The obvious advantage of the proposed method is that no sample changes are necessary, and the time between measurements is minimal.

A cross-sectional view of the proposed sample is given in Figure E.1a. A double aperture is aligned above the chip. A distance of 0.035" between centers of the reference and the test sample was found to provide adequate isolation, given the measured size of the

SUBSTRATE

REFERENCE   TEST DIODE
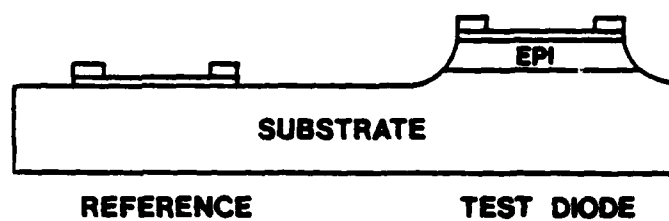
a)
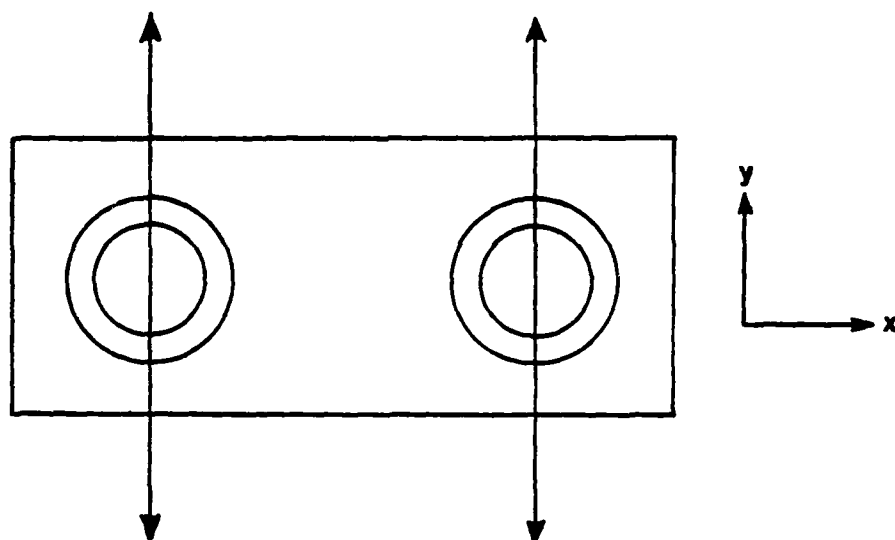
b)

Figure F.1.   Proposed sample for absolute phase measure-
ments.   a) Cross-section of test structure.   b) Top
view, indicating position of electron beam for 10.6
GHz measurements.

electron beam.

The direction of beam sweep is shown in Figure E.1b. The modulated beam is first positioned over the reference, and the corresponding phase measured. Next, electrostatic deflection is used to shift the beam in the x-direction until it is centered on the test diode, and the phase measured as a function of bias voltage.

Preliminary measurements performed with this technique using n-Si samples yielded inconclusive results. Correct interpretation of the experimental data requires a more complete understanding of the circuit interaction arising from placing both the reference and test sample in the same package.

References

1. E.J. Ryder and W. Shockley, "Mobilities of Electrons in High Electric Fields," Phys. Rev. 81, 139 (1951).

2. C.A. Lee, et al., "The Read Diode - An Avalanching, Transit-time, Negative Resistance Oscillator," Appl. Phys. Lett. 6, 89 (1965).

3. K. Blotekjaer, "Transport Equations for Electrons in Two-valley Semiconductors," IEEE Trans. Elec. Devices ED-17, 38 (1970).

4. Robert Cook, Ph.D. Thesis, Cornell University (1981).

5. M. Asche and O.G. Sarbei, "Electrical Conductivity of Hot Carriers in Si and Ge," Phys. Stat. Sol. 33, 9 (1969).

6. T. Kurosawa, J. Phys. Soc. Japan Suppl. 21, 424 (1966).

7. H. Budd, J. Phys. Soc. Japan Suppl. 21, 420 (1966).

8. W. Fawcett, D.A. Boardman, and S. Swain, "Monte Carlo Determination of Electron Transport Properties in Gallium Arsenide," J. Phys. Chem. Solids 31, 1963 (1970).

9. S.G. Kratzer and J. Frey, "Transient Velocity Characteristics of Electrons in GaAs with Γ-L-X Conduction Band Ordering," J. Appl. Phys. 49, 4064 (1978).

10. C. Jacoboni and L. Reggiani, "Bulk Hot-Electron Properties of Cubic Semiconductors," Advances in Physics 28, 493 (1979).

11. E.J. Ryder, "Mobility of Holes and Electrons in High Electric Fields," Phys. Rev. 90, 766 (1953).

12. T.E. Seidel and D.L. Scharfetter, "Dependence of Hole Velocity Upon Electric Field and Hole Density for p-type Silicon," J. Phys. Chem. Solids 28, 2563 (1967).

13. A.C. Prior, "The Field-Dependence of Carrier Mobility in Silicon and Germanium," J. Phys. Chem. Solids 12, 175 (1959).

14. M. Asche, J. Von Borzeskowski, and O.G. Sarbei, "Conductivity of Hot Holes in Silicon at 77°K," Phys. Stat. Sol. 38, 357 (1970).

15. J.W. Holm-Kennedy and K.S. Champlin, "Warm-Carrier dc Transport in n-Si," J. Appl. Phys. 43, 1878 (1972).

16. V.L. Dalal, A.B. Dreeben, and A. Triano, "Temperature Dependence of Hole Velocity in p-GaAs," J. Appl. Phys. 42, 2864 (1971).

17. J.G. Nash and J.W. Holm-Kennedy, "Effect of Electron-Electron Scattering on Hot-Electron Repopulation in n-Si at 77K," Phys. Rev. B 16, 2834 (1977).

18. J. Von Borzeskowski and J. Scholz, "On the Electric Field Dependence of the Conductivity of Holes in Si at Low Temperatures," Phys. Stat. Sol. B 79, 525 (1977).

19. R.K. Cook and J. Frey, "High-Field Electron Transport in Silicon-on-Sapphire Layers," J. Appl. Phys. 51, 2656 (1980).

20. E.M. Bastida, et al., "Indirect Electron Drift Velocity versus Electric Field Measurement in GaAs," Appl. Phys. Letters 18, 28 (1971).

21. K. Seeger, "Microwave Field Dependence of Drift Mobility in Germanium," Phys. Rev. 114, 476 (1959).

22. A.F. Gibson, J.W. Granville, and E.G.S. Paige, "A Study of Energy-loss Processes in Germanium at High Electric Fields Using Microwave Techniques," J. Phys. Chem. Solids 19, 198 (1961).

23. M.A.C.S. Brown, "Deviations from Ohm's Law in Germanium and Silicon," J. Phys. Chem. Solids 19, 218 (1961).

24. J. Zucker, V.J. Fowler, and E.M. Conwell, "High-Field Conductivity in Germanium and Silicon at Microwave Frequencies," J. Appl. Phys. 32, 2606 (1961).

25. C. Hamaguchi and Y. Inuishi, "Conductivity Anisotropy of Hot Electrons in n-type Silicon Heated by Microwave Fields," J. Phys. Chem. Solids 27, 1511 (1966).

26. G.H. Glover, "Study of Electron Energy Relaxation Times in GaAs and InP," _J. Appl. Phys._ <u>44</u>, 1295 (1973).

27. V. Rodriguez, H. Ruegg, and M-A. Nicolet, "Measurement of the Drift Velocity of Holes in Silicon at High-Field Strengths," _IEEE Trans. Elec. Devices_ <u>ED-14</u>, 44 (1967).

28. C.Y. Duh and J.L. Moll, "Electron Drift Velocity in Avalanching Silicon Diodes," _IEEE Trans. Elec. Devices_ <u>ED-14</u>, 46 (1967).

29. V. Rodriguez and M-A. Nicolet, "Drift Velocity of Electrons in Silicon at High Electric Fields From 4.2° to 300°K," _J. Appl. Phys._ <u>40</u>, 496 (1969).

30. H. Okamoto and M. Ikeda, "Measurement of the Electron Drift Velocity in Avalanching GaAs Diodes," _IEEE Trans. Elec. Devices_ <u>ED-23</u>, 372 (1976).

31. B. Kramer and A. Mircea, "Determination of Saturated Electron Velocity in GaAs," _Appl. Phys. Letters_ <u>26</u>, 623 (1975).

32. W.E. Spear, "The Hole Mobility in Selenium," _Proc. Phys. Soc._ <u>78</u>, 826 (1960).

33. P.A. Tove, et al., "Measurement of Drift Velocity of Electrons in Silicon by Exciting a Diode Structure with Short Superradiant Laser Pulses," _IEEE Trans. Elec. Devices_ <u>ED-17</u>, 407 (1970).

34. J.G. Ruch and G.S. Kino, "Transport Properties of GaAs," _Phys. Rev._ <u>174</u>, 921 (1968).

35. T.H. Glisson, et al., "Circuit Effects in Time-of-Flight Diffusivity Measurements," _Solid-State Electronics_ <u>23</u>, 627 (1980).

36. T.W. Sigmon and J.F. Gibbons, "Diffusivity of Electrons and Holes in Silicon," _Appl. Phys. Letters_ <u>15</u>, 320 (1969).

37. C.B. Norris and J.F. Gibbons, Measurement of High-Field Carrier Drift Velocities in Silicon by a Time-of-Flight Technique," _IEEE Trans. Elec. Devices_ <u>ED-14</u>, 38 (1967).

38. R. Cecchi, et al., "Electrons and Holes Drift Velocity in Silicon at Very Low Temperature," _Solid State Comms._ <u>6</u>, 727 (1968).

39. H.R. Zulliger, et al., "Electric Field Profile and Electron Drift Velocities in Lithium Drifted Silicon," Nucl. Instr. Methods 70, 125 (1969).

40. C. Canali, G. Ottaviani, and A. Alberigi-Quaranta, "Drift Velocity of Electrons and Holes and Associated Anisotropic Effects in Silicon," J. Phys. Chem. Solids 32, 1707 (1971).

41. G.A. Haas, T. Pankey Jr., and F.H. Harris, "Temperature Dependence of Electron Drift Velocity in Silicon," J. Appl. Phys. 44 2433 (1973).

42. C. Canali, et al., "Electron Drift Velocity in Silicon," Phys. Rev. B 12, 2265 (1975).

43. F. Nava, et al, "On the Diffusivity of Holes in Silicon," J. Appl. Phys. 50, 922 (1979).

44. P.A. Houston and A.G.R. Evans, "Electron Drift Velocity in n-GaAs at High Electric Fields," Solid-State Electronics 20, 197 (1977).

45. D.M. Chang and J.G. Ruch, "Measurement of the Velocity Field Characteristic of Electrons in Germanium," Appl. Phys. Letters 12, 111 (1968).

46. G. Ottaviani, et al., "Hole Drift Velocity in High-Purity Ge Between 8 and 220°K," J. Appl. Phys. 44, 2917 (1973).

47. C. Canali, et al., "Hole Drift Velocity in Semi-insulating CdTe," Appl. Phys. Letters 19, 51 (1971).

48. A Neukermans and G.S. Kino, "Measurement of Velocity-Field Characteristics of Electrons in InSb at High Fields," Appl. Phys. Letters 17, 102 (1970).

49. C. Canali, et al., "Hole and Electron Drift Velocity in CdSe at Room Temperature," Solid State Comms. 11, 105 (1972).

50. G.W. Bradberry and W.E. Spear, "Electron Mobility and Edge Emission in CdS Crystals," Brit. J. Appl. Phys. 15, 1127 (1964).

51. A.G.R. Evans, P.N. Robson, and M.G. Stubbs, "New Time-of-Flight Technique for Measuring Drift Velocity in Semiconductors," Electronics Letts. 8, 195 (1972).

52. A.G.R. Evans and P.N. Robson,"Drift Mobility Measurements in Thin Epitaxial Semiconductor Layers using Time-of-Flight Techniques," Solid-State Electronics 17, 805 (1974).

53. D.P. Kennedy, P.C. Murley and W. Kleinfelder, "On the Measurement of Impurity Atom Distributions in Silicon by the Differential Capacitance Technique," IBM J. Res. Develop., 399 (1968).

54. R.B. Shirts and R.G. Gordon, "Improved Approximate Analytic Charge Distributions for Abrupt p-n Junctions," J. Appl. Phys. 50, 2840 (1979).

55. See, for example, R.S. Muller and T.I. Kamins, Device Electronics for Integrated Circuits (Wiley, New York, 1977), p. 88.

56. W. Schottky, Z. Phys. 113, 367 (1939); 117, 574 (1941).

57. W. Shockley, "The Theory of p-n Junctions in Semiconductors and p-n Junction Transistors," Bell Syst. Tech. Journal 28, 435 (1949).

58. S. Kratzer, "Computer Simulations of Electron Transport in GaAs," M.S. Thesis, cornell University, 1978.

59. J.P. Nougier, "Noise and Diffusion of Hot Carriers," in Physics of Nonlinear Transport in Semiconductors (Plenum Press, New York, 1980).

60. H. Kanter, "Electron Scattering by Thin Foils for Energies Below 10 keV," Phys. Rev 121, 461 (1961).

61. T.E. Everhart and P.H. Hoff, "Determination of Kilovolt Electron Energy Dissipation vs. Penetration Distance in Solid Materials," J. Appl. Phys. 42, 5837 (1971).

62. W.W. Siekanowicz, et al., "Current-Gain Characteristics of Schottky Barrier and p-n Junction Electron Beam Semiconductor Didoes," IEEE Trans. Elec. Devices ED-21, 691 (1974).

63. C.R. Crowell and S.M. Sze, "Quantum Mechanical Reflection at Metal-Semiconductor Barriers," J. Appl. Phys. 37, 2683 (1966).

64. E. Wasserstrom and J. McKenna, "The Potential Due to a Charged Metallic Strip on a Semiconductor Surface," Bell Syst. Tech. Jour. 49, 853 (1970).

65. J.A. Lewis and E. Wasserstrom, "The Field
     Singularity at the Edge of an Electrode on a
     Semiconductor Surface," Bell Syst. Tech. Jour. 49,
     1183 (1970).

66. M.P. Lepselter and S.M. Sze, "Silicon Schottky
     Barrier Diode with Near-Ideal I-V Characteristics,"
     Bell Syst. Tech. Jour. 47, 195 (1968).

67. V.S. Formenko, Handbook of Thermionic Properties,
     edited by G.V. Samsonov, (Plenum Press Data
     Division, New York, 1966).

68. C.A. Mead, "Metal-Semiconductor Surface Barriers,"
     Solid State Electronics 9, 1023 (1966).

69. Hewlett Packard, Microwave Network Analyzer
     Applications AN 117-1, (1970).

70. Glenn Thoren, Private Communication.

71. R.F. Harrington, Time-Harmonic Electromagnetic
     Fields (McGraw-Hill, New York, 1961), p. 214.

72. S. Ramo, J.R. Whinnery, and T. VanDuzer, Fields and
     Waves in Communication Electronics, (Wiley, New
     York, 1965), p. 551.

73. Cliftronics, Inc., 515 Broad Street, Clifton, New
     Jersey, 07013.

74. Instruction Manual GEK-9738, General Electric Co.

75. C.A. Lee, Private Communication.

76. S.M. Sze, Physics of Semiconductor Devices (Wiley,
     New York, 1969), p. 130.

77. C. Canali, et.al. "High Field Diffusion of
     Electrons in Silicon," Appl. Phys. Lett. 27, 278
     (1975).

78. J.B. Bott and C. Hilsum, "An Analytic Approach to
     the LSA Mode," IEEE Trans. on Electron Devices ED-
     14, 492 (1967).

79. C. Jacoboni, et al., "A Review of Some Charge
     Transport Properties of Silicon," Solid State
     Electronics 20, 77 (1977).

80. M.G. Stubbs, "Hot Electron Mobility Measurements by
     a Microwave Time-of-Flight Technique," Ph.D.
     Thesis, Sheffield University, 1975.

81. P.M. Smith, M. Inoue and J. Frey, "Electron
     Velocity in Si and GaAs at Very High Electric
     Fields," Appl. Phys. Lett. 37, 797 (1980).

82. N. Braslau and P.S. Hauge, "Microwave Measurement
     of the Velocity-Field Characteristic of GaAs," IEEE
     Trans. Elec. Devices ED-17, 616 (1970).

83. W. Fawcett and H.D. Rees, "Calculation of the Hot
     Electron Diffusion Rate for GaAs," Phys. Lett. A
     29, 578 (1969).

84. M.A. Littlejohn, J.R. Hauser and T.H. Glisson,
     "Velocity-Field Characteristics of GaAs with Γ-L-X
     Conduction Band Ordering," J. Appl. Phys. 48, 4587
     (1977).

85. J. Pozela and A. Reklaitis, "Electron Transport
     Properties in GaAs at High Electric Fields," Solid
     State Electronics 23, 927 (1980).

86. M. Abe, et al., "Monte-Carlo Calculations of
     Diffusion Coefficient of Hot Electrons in n-type
     GaAs," Appl. Phys. Lett. 25, 675 (1974).

87. Andre Castelain, et al., "Value of Electron
     Diffusion Constant in GaAs for High Electric
     Field," Appl. Phys. Lett. 25, 721 (1974).

88. V.E. Riginos, "Nonsaturating Velocity-Field
     Characteristic of Gallium Arsenide Experimentally
     Determined From Domain Measurements," J. Appl.
     Phys. 45, 2919 (1974).

89. J. P. Pokorny and F. Jelinek, "Experimental
     Nonsaturating Velocity-Field Characteristic of
     GaAs," Proc. IEEE 60, 457 (1972).

90. T.W. Sigmon and J.F. Gibbons, "Measurement of High-
     Field Carrier Drift Velocities in Silicon by a
     Time-of-Flight Technique," IEEE Trans. Elec.
     Devices ED-14, 38 (1967).

91. Phillip M. Smith, Jeffrey Frey and P. Chatterjee,
     "High-Field Transport of Holes in Silicon," Appl.
     Phys. Lett. 39, 332 (1981).

92. W.J. Getsinger, "The Packaged and Mounted Diode as
     a Microwave Circuit," IEEE Trans. MTT MTT-14, 58
     (1962).

93. A. Alberigi Quaranta, M. Martini, and G. Ottaviani, "The Pulse Shape and the Timing Problem in Solid State Detectors - A Review Paper," IEEE Trans. Nucl. Sci. NS-16, 35 (1969).

94. "S-Parameter Design," Hewlett-Packard Application Note 154, 1 (1972).

95. C.A. Lee, et al., "Ionization Rates of Holes and Electrons in Silicon," Phys. Rev. 134, A761 (1964).

96. H.D. Law and C.A. Lee, "Interband Scattering Effects on Secondary Ionization Coefficients in GaAs," Solid-State Electronics 21, 331 (1978).

97. S.M. Sze, Physics of Semiconductor Devices, (Wiley, New York, 1969), p. 113.

98. H.R. Zulliger, "Hole-Electron Production in Semiconductors," J. Appl. Phys. 42, 5570 (1971).

99. R.U. Martinelli and C.C. kWang, "Electron-Beam Penetration in GaAs," J. Appl. Phys. 44, 3350 (1973).

100. A Taroni and G. Zanarini, "Plasma Effects and Charge Collection Time in Solid State Detectors," Nucl. Instr. Meth. 67, 277 (1969).

101. P.A. Tove and W. Seibt, "Plasma Effects in Semiconductor Detectors," Nucl. Instr. Meth. 51, 261 (1967).

102. R. Cook, Private Communication.

103. H.J. Leamy, L.C. Keamerling, and S.D. Ferris, "Electron Beam Induced Current," in Scanning Electron Microscopy Vol.I, SEM, Inc.

104. C.H. Lee, A. Antonetti and G. Mourou, "Measurements of the Photoconductive Lifetime of Carriers in GaAs by Optoelectronic Gating Techniques," Opt. Commun. 21, 158 (1977).

105. H. Kroemer, "Negative Conductance in Semiconductors," IEEE Spectrum 5, 47 (1968).

106. J.G. Ruch, "Electron Dynamics in Short Channel Field-Effect Transistors," IEEE Trans. Elec. Dev. ED-19, 652 (1972).

107. H.D. Rees, "Calculation of the Distribution Functions by Exploiting the Stability of the Steady State," J. Phys. Chem. Solids 30, 643 (1969).

108. T.J. Maloney and J. Frey, "Transient and Steady-State Electron Transport Properties of GaAs and InP," J. Appl. Phys. 48 781 (1977).

109. T. Wada and J. Frey, "Physical Basis of Short-Channel MESFET Operation," IEEE Trans. Elec. Dev. ED-26, 476 (1979).

110. T.J. Maloney and J. Frey, "Frequency Limits of GaAs and InP Field-Effect Transistors at 300K and 77K with Typical Active Layer Doping," IEEE Trans. Elec. Dev. ED-23, 519 (1976).

111. C.V. Shank, et al., "Picosecond Nonequilibrium Carrier Transport in GaAs," Appl. Phys. Lett. 38, 104 (1981).

112. S. Laval, et al., "Velocity Overshoot Investigations in Submicron GaAs Devices by Photoconductior Experiments," IEDM (1980).

113. W. Fawcett and H.D. Rees, "Calculation of the Hot Electron Diffusion Rate for GaAs," Phys. Lett.A 29, 578 (1969).

114. T.J. Maloney, Private Communicaiton.

115. S.G. Kratzer, Private Communication.

116. R. Cook, Private Communication.

117. E. Constant, Private Communication.

118. C.H. Lee, P.S. Mak, and A.P. DeF0nzo, "Optical Control of Millimeter-Wave Propagation in Dielectric Waveguides," IEEE Jour. Quant. Elec. QE-16, 277 (1980).

119. See, for example, P.A. Blakey, R.A. Giblin, and A.J. Seeds, "Large-Signal Time-Domain Modeling of Avalanche Diodes," IEEE Trans. Electron devices ED-26, 1718 (1979).

120. J.P. Boris and D.L. Book, "Flux-Corrected Transport. I. Shasta, A Fluid Transport Algorithm that Works," J. Comput. Phys. 11,38,(1973).

121. D.L. Book, J.P.Boris, and K. Hain, "Flux-Corrected Transport. II. Generalizations of the Method, J. Comput. Phys. 18, 248 (1975).

122. J. McClymonds, "Linear, High Power IMPATT Amplifiers Using Constant Voltage Bias," Ph.D. Thesis, Cornell University, 1980.

123. J.W. McClymonds, Private Communication.

124. J. Hilibrand and R.D. Gold, <u>RCA Review</u> <u>21</u>, 245 (1960).

125. D.P. Kennedy, P.C. Murley and W. Kleinfelder, "On the Measurement of Impurity Atom Distributions in Silicon by the Differential Capacitance Technique," <u>IBM J. Res. Develop</u>., 399 (1968).

126. G. Baccarani, et al., "Interpretation of C-V Measurements for Determining the Doping Profile in semiconductors," <u>Solid State Electronics</u> <u>23</u>, 65 (1980).

127. <u>CRC Standard Mathematical Tables</u> (CRC Press, Palm Beach, Florida, 1978), p. 524.

128. G. Hill, Ph.D. Thesis, Sheffield University, 1979.